Ambient Noise Tomography for Wavespeed and Anisotropy in the Crust of Southwestern China

by

Hui Huang

M.S. Geophysics, Peking University, Beijing, China, 2007
B.S. Geophysics, Peking University, Beijing, China, 2004

Submitted to the Department of Earth, Atmospheric, and Planetary Sciences
in partial fulfillment of the requirements for the degree of

Doctor of Philosophy

at the

MASSACHUSETTS INSTITUTE OF TECHNOLOGY

February 2014

Author:.....
Department of Earth, Atmospheric, and Planetary Sciences
October 11, 2013

Certified by:.....
Robert D. van der Hilst
Schlumberger Professor of Earth Sciences
Head, Department of Earth, Atmospheric and Planetary Sciences
Thesis Supervisor

Accepted by:.....
Robert D. van der Hilst
Schlumberger Professor of Earth Sciences
Head, Department of Earth, Atmospheric and Planetary Sciences

Ambient Noise Tomography for Wavespeed and Anisotropy in the Crust of Southwestern China

by

Hui Huang

Submitted to the Department of Earth, Atmospheric, and Planetary Sciences
on October 11, 2013 in partial fulfillment of the requirements for the Degree of
Doctor of Philosophy in Geophysics

Abstract

The primary objective of this thesis is to improve our understanding of the crustal structure and deformation in the southeastern Tibetan Plateau and adjacent regions using surface wave tomography. Green's functions for Rayleigh and Love waves are extracted from ambient noise interferometry. Using the Green's functions, we first conduct traditional traveltime tomography for the two shear wavespeeds V_{SV} and V_{SH}. Their differences are measured as radial anisotropy. We then conduct Eikonal tomography to study azimuthal anisotropy in the crust. Our tomography results are well consistent with geology in the study region. In the Sichuan Basin, low wavespeed and positive radial anisotropy ($V_{SH}>V_{SV}$) in the upper crust reflect thick sedimentary layers at surface; high wavespeed and small radial anisotropy in the middle and lower crust reflect a cold and rigid basin root. Little azimuthal anisotropy is observed in the Basin, indicating small internal deformation. In the Tibetan Plateau, we observe widespread low wavespeed zones with positive anisotropy in the middle and lower crust, which may reflect combined effects of weakened rock mechanism and horizontal flow in the deep crust of southeastern Tibet. The northern part of the Central Yunnan block, which geographically coincides with the inner zone of the Emeishan flood basalt, reveals relatively higher wavespeeds than the surrounding regions and little radial anisotropy throughout the entire crust. We speculate that the high wavespeeds and small radial anisotropy are due to combined effects of the remnants of intruded material from mantle with sub-vertical structures and channel flow with sub-horizontal structures. In general, the azimuthal anisotropy in our study region is consistent with a clockwise rotation around the Eastern Himalayan Syntaxis. Careful examination reveals large angular differences between the azimuthal anisotropy in the upper and lower crust, suggesting different deformation patterns at the surface and in depth. Therefore, our tomography results support models with ductile flow in the deep crust of the southeastern Tibetan Plateau; however, the large lateral variation of both wavespeeds and anisotropy indicates that the flow also varies greatly in intensity and pattern in different geological units.

Thesis supervisor: Robert D. van der Hilst
Title: Schlumberger Professor of Earth Sciences
Head, Department of Earth, Atmospheric and Planetary Sciences

Acknowledgments

First of all, I would like to express my heartfelt gratitude to my advisor Professor Robert D. van der Hilst for his invaluable advice and guidance. He showed unlimited patience in our discussion. This work could not have been done without his interests and encouragement. He always unselfishly contributed his creative ideas, which constantly helped me out of troubles and pushed me towards brighter directions in the research. His enthusiasm about Earth sciences had great influence in my MIT life. Through him, I understood what it means to be a geophysicist. It was my greatest fortune and pleasure to work with him.

I owe much gratitude to Professor Brad Hager, who was the advisor for my second project in general exam. He always made time to answer my questions and offer useful insights. I also owe much to Professor Maarten de Hoop at Purdue University. His broad knowledge in geophysics and mathematics was particularly helpful for my research. I would also like to thank other thesis committee members Professor Leigh Royden, Professor Alison Malcolm, and general exam committee member Professor Nafi Toksöz. Conversations with them were very useful for my research.

My appreciation also goes to Professor Huajian Yao from University of Science and Technology of China, Professor Qiyuan Liu and Dr. Yu Li from the China Earthquake Administration. The precious collaboration with them was invaluable to the project.

My work was also benefited by intuitive discussion with Research Scientists, Postdocs, and graduate students at EAPS, Ping Wang, Min Chen, Xuefeng Shang, Tianrun Chen, Zhenya Zhu, Chang Li, Haijiang Zhang, Yingcai Zheng, Rizheng He, Junlun Li, Xinding Fang, Di Yang, Chen Gu, Chunquan Yu, Jing Liu, Haoyue Wang, and Zhulin Yu.

I would also like to thank Sue Turbak, Vicki McKenna, Carol Sprague, and Jacqueline Taylor for their constant help during my six years at MIT.

I am deepest grateful to my husband Jian Yang, my mother Gaoxiu Jia and my sister Shengnan Huang for their greatest support, encouragement and love.

Table of Contents

List of Figures

Chapter 1

Introduction

1.1 Structure and deformation in the lithosphere of the southeastern Tibetan Plateau

The Tibetan plateau, as the consequence of the collision between the Indian and Eurasian plates, has elevated more than 5km since about 50 Ma (Molnar and Tapponnier, 1975). As the Indian plate moves northward, materials are extruded from the central collision zone to the margins of the Plateau, causing rapid surface uplift of southeastern Tibet at approximately 8 Ma (Royden et al., 2008). Due to the obstacle of the rigid lithosphere of the Sichuan Basin, this material transport bifurcates at the eastern margin of the Plateau. The southern branch changes its direction about 90° around the Eastern Himalayan Syntaxis: from nearly eastward to nearly southward (Wang, 1998; Wang and Burchfiel, 2000; Shen et al., 2005). The active material transport and lateral variation in strength of the crust cause a lot of earthquakes in the southeastern Tibetan Plateau and Central Yunnan block, including the 2008 Wenchuan earthquake (M = 8.0) on the Longmenshan fault. Therefore, the region between the Eastern Himalayan Syntaxis and the Sichuan Basin is of particular importance to understand the uplift history and relevant dynamic processes of the whole Plateau,

and our study of the crustal structure may also help understand the mechanism of the local seismicity.

The southeastern Tibetan Plateau has a complicated tectonic history (Royden et al., 2008). Even after decades of research there is still controversy and debate about the mechanism of deformation. A lot of modeling works have been conducted to account for the topography variation, surface velocity field from GPS observations, stress field derived from earthquake focal mechanism, and other measurements. In general, there are three schools of modeling which propose distinct lithospheric settings and thus have different implications for the deformation mechanism.

The first school considers the lithosphere of Tibet as a rigid plate, and one representative example is the rigid block extrusion model (Molnar and Tapponnier, 1975; Pelzer and Tapponnier, 1988). This model proposes that the crust of Tibet is composed of several rigid sub-blocks which have little interior deformation. Large deformation only occurs on narrow zones between these sub-blocks, which can penetrate through the entire lithosphere, to compensate the material extrusion due to the India-Eurasia collision. Since this rigid block model suggests mechanically strong and coupled lithosphere, the variation of the deformation is small in the depth direction.

The second school considers the lithosphere as a thin viscous sheet with continuous deformation in response to the India-Eurasian collision and gravity force, obeying a Newtonian or a power law rheology (England and McKenzie, 1982; England and Houseman, 1986; Flesch et al., 2001). Since, in this school, it is assumed

that the vertical gradients of the horizontal velocity are negligible, both the rheology and modeled deformation are the averages in depth direction.

The third school proposes to explain the topography with either sharp or smooth gradient near the margins of the Tibetan Plateau (Royden et al., 1997; Clark and Royden, 2000). Channel flow with constant material transportation and deformation mainly occurs in a week zone in the deep crust and form distinct topography gradients due to the rheology contrasts between the Plateau and its surrounding regions. Since the most straightforward way to reduce viscosity is the increased temperature, we would expect, for instance, higher heat flow, lower seismic wavespeed, and higher Poisson's ratio.

Besides the above three schools with simple concepts, more complicated numerical modeling has been conducted recently (Copley and McKenzie, 2007; Copley, 2008). Since the rheology is poorly constrained, even if the deformation at the surface is well modeled its patterns in deep lithosphere can differ greatly with different settings of rheology. Therefore, the coupling of the lithosphere may not be determined from surface observations alone.

Previous studies reveal complicated variations of the material properties in the lithosphere of the southeastern Tibetan Plateau, corresponding to the complicated tectonic history of this region. These results have been used to support one of the models mentioned above. At surface, GPS observations reveal several sub-blocks separated by faults on which the major deformation occurs (Shen et al., 2005). At depth, although a weak middle and lower crust is suggested by recent discoveries of

low wavespeed zones (Yao et al., 2008, Zhang et al., 2012), high Poisson's ratio (Hu et al., 2005; Xu et al., 2007), high heat flow (Hu et al., 2000), and low electrical resistivity (Bai et al., 2010), all these properties reveal great spatial variation, both horizontally and vertically. Hence, the deformation in the deep crust, for example flow as suggested in the channel flow model (Royden et al., 1997), if it occurs at all, is also expected to vary greatly in pattern. Furthermore, based on the comparison between GPS observations and shear wave splitting, Sol et al. (2007) suggest a strong lower crust and hence couple lithosphere around the Eastern Himalayan Syntaxis but possible weak lower crust and decoupled lithosphere in southeastern Plateau.

1.2 Thesis objectives

In view of the above background, the objective of this thesis is to obtain detailed models of seismic wavespeed and anisotropy, both radial and azimuthal, to understand the deformation in the crust of the southeastern Tibetan Plateau and its surrounding regions. Firstly, we construct 3-D models for the two shear wavespeeds V_{SV} and V_{SH} with vertical and horizontal polarizations, respectively, and their difference are measured as the radial anisotropy. Secondly, we investigate the relationship between the two wavespeeds and radial anisotropy. We compare the distribution of the low wavespeed and positive radial anisotropy. Thirdly, we construct a 3-D model for the azimuthal anisotropy. Finally, we discuss the implications of our understanding of the deformation patterns in the lithosphere of the southeastern Tibet.

1.3 Traditional and Eikonal tomography

To meet the objectives above, we conduct both traditional and Eikonal tomography on surface wave signals extracted from ambient noise interferometry (Yao et al., 2006). The Green's functions for both Rayleigh and Love waves are calculated from cross-correlation functions of the seismic noise records. We use data from three temporary arrays in the southeastern marginal region of the Tibetan Plateau and the Sichuan Basin (Figure 1-1). Two relatively sparse arrays were deployed by Lehigh University and Massachusetts Institute of Technology (MIT) from Oct 2003 to Sep 2004, with an average inter-station distance of approximately 50-100 km. A much denser array was conducted by China Earthquake Administration (CEA) from Jan 2007 to Dec 2009, with an average inter-station distance of approximately 20-30 km. In this study we only use seismic records of the year 2007 from the CEA array, because one year data is sufficient to extract clear signals of Green's functions (Bensen et al., 2007). Since Green's functions are extracted for each station-pair, we obtain very dense raypath coverage and thus tomography results with sufficient details for the study region.

The fundament of traveltime tomography is the (non-linear) relation between the traveltime of a certain wave and local wavespeed. Basically, there are two types of equations connecting them, based on which different tomography schemes are developed (Table 1). The first type of equation has an integral form: the total traveltime is the integration or summation the local wave slowness along the raypath. A kernel can be introduced into the integration to account for effects such as finite

frequency (Dahlen et al., 2000). Most of the tomography studies are based on this integration relation. A "de-integration" operation, matrix inversion in this study, can be implemented to calculate the local wavespeed. Since all the raypaths are used simultaneously in the matrix inversion, the traditional tomography has good resolution. Therefore, in this thesis, we use it to study the isotropic wavespeeds, i.e. V_{SV} and V_{SH}. Radial anisotropy is also studied because it is calculated from the two isotropic wavespeeds.

The second type of equation, i.e. the Eikonal equation, has a differential form: the local wave slowness and propagation direction are directly obtained from the gradient of the traveltime (Shearer, 1999). Eikonal tomography is more efficient in computation because it avoids the time-consuming calculation of matrix inversion in traditional tomography, especially when there are a large number of raypaths. To accurately estimate the traveltime and its gradient from a specific source for the entire study region, an interpolation operator is applied. In the interpolation, only traveltime data for the specific source are used, this procedure is fast because less data (than the whole data set) are involved. Furthermore, since no assumption is made for the raypath, the wave propagation direction is more accurate than that in the traditional tomography (great circle in this thesis). Therefore, we mainly apply the Eikonal tomography to calculate azimuthal anisotropy.

1.4 Thesis structure

This thesis contains five chapters. In Chapter 1 (this chapter), we introduce the

background geological settings for the southeastern Tibetan Plateau. We also present the motivations and objectives of this thesis work.

In Chapter 2, published as Huang et al. (2010), we conduct surface wave tomography using seismic noise records from MIT and Lehigh arrays. Green's functions for both Rayleigh and Love waves are calculated from the cross-correlation functions of the vertical and transverse components, respectively. Average phase velocities or dispersion curves along the raypaths are then measured using a phase image analysis technique (Yao et al., 2006). These dispersion curves are used to invert for 3-D models for the two shear wavespeed V_{SV} and V_{SH}, respectively. The difference between the two wavespeeds are examined both in view of non-uniqueness of tomographic solutions and radial anisotropy. We also analyze the correlation between the wavespeeds and radial anisotropy.

In Chapter 3, which is in preparation for publication, we conduct surface wave tomography using seismic noise records from CEA array. This is an extension work of Chapter 2 but with much denser data and a more sophisticated inversion scheme. The densely deployed array enhances the resolution with more details for the study region. To constrain the wavespeeds and radial anisotropy better, we develop a new scheme to invert jointly for the two wave speeds (V_{SH} and V_{SV}), thus the radial anisotropy is explicitly included in the inversion.

In Chapter 4, which is also in preparation for publication, we conduct Eikonal tomography (Shearer, 1999) using seismic records from CEA array as in Chapter 3. We develop an improved interpolation scheme to accurately estimate the traveltime

for Rayleigh waves, the gradient of which reflects the local wave slowness and propagation direction. Assuming a HTI medium (horizontal transverse isotropic), we obtain the angular variation of the wavespeed (or slowness) in the horizontal plane, i.e. the azimuthal anisotropy. Then the variations of azimuthal anisotropy at different depths are carefully examined and compared with surface strain-rate and SKS splitting to build up comprehensive perspectives about the crustal deformation for the southeastern Tibetan Plateau.

Chapter 5 is the summary and conclusion chapter. We summarize our understanding of the structure and deformation mechanism in the lithosphere of the southeastern Tibetan Plateau. Possible directions of future research are also discussed.

References

Bai, D., M. J. Unsworth, M. A. Meju, X. Ma, J. Teng, X. Kong, Y. Sun, J. Sun, L. Wang, C. Jiang, C. Zhao, P. Xiao, and M. Liu, (2010), Crustal deformation of the eastern Tibetan plateau revealed by magnetotelluric imaging, Nature Geosci., 3, 358-362, doi:10.1038/ngeo830.

Bensen, G.D., M.H. Ritzwoller, M.P. Barmin, A.L. Levshin, F. Lin, M.P. Moschetti, N.M. Shapiro, and Y. Yang, (2007), Processing seismic ambient noise data to obtain reliable broad-band surface wave dispersion measurements, Geophys. J. Int., 169, 1239-1260.

Clark, M., and L. Royden, (2000), Topographic ooze: Building the eastern margin of Tibet by lower crustal flow, Geology, 28, 703-706.

Copley, A., D. McKenzie, (2006), Models of crustal flow in the India-Asia collision zone, Geophys. J. Int., 169, 683-698.

Copley, A., (2008), Kinematics and dynamics of the southeastern margin of the Tibetan Plateau, Geophys. J. Int., 174, 1081-1100.

Dahlen, F., S. Huang, and G. Nolet, (2000), Frechet kernels for finite-frequency traveltimes – I. Theory, Geophys. J. Int., 141(1), 157-174.

England, P., and D. McKenzie, (1982), A thin viscous sheet model for continental deformation, Geophys. J. R. Astr. Soc., 70, 295-321.

England, P., and G. Houseman, (1986), Finite strain calculations of continental deformation, 2, Comparison with the India-Asia collision zone, J. Geophys. Res., 91, 3664-3676.

Flesch, L., J. Haines, W. Holt, (2001), Dynamics of the India-Eurasia collision zone, J. Geophys. Res., 106(B8), 16435-16460.

Hu, S., L. He, and J. Wang, (2000), Heat flow in the continental area of China: a new data set, Earth planet. Sci. Lett., 179, 407–419.

Hu, J.F., Y.J. Su, X. Zhu, Y. Chen, (2005), S-wave velocity and Poisson's ratio structure of crust in Yunnan and its implication, Science in China Ser. D Earth Sciences, 48(2), 210-218.

Huang, H., H. Yao, and R.D. van der Hilst (2010), Radial anisotropy in the crust of SE Tibet and SW China from ambient noise interferometry, Geophysical Research Letters, 37(21), DOI: 10.1029/2010GL044981.

Molnar P., and P. Tapponnier, (1975), Cenozoic tectonics of Asia: Effects of a continental collision: Features of recent continental tectonics in Asia can be interpreted as results of the India-Eurasia collision, Science, 189, 419-426.

Peltzer, G., and P. Tapponnier, (1988), Formation and evolution of strike-slip faults, rifts, and basins during the India-Asia collision: An experimental approach, Journal of Geophysical research, 93, 15085-15117.

Shearer P., (1999), Introduction to seismology, Cambridge University Press, ISBN 0-521-66023-8 (hbk.).-ISBN 0-521-66953-7 (pbk), 237-240.

Royden, L.H., B.C. Burchfiel, R.W. King, E. Wang, Z. Chen, F. Shen, and Y. Liu, (1997), Surface deformation and lower crustal flow in eastern Tibet, Science, 276, 788-790.

Royden, L.H., B.C. Burchfiel, R.D. van der Hilst, (2008), The geological evolution of the Tibetan plateau, Science, 321, 1054-1058.

Shen, Z., J. Lv, M. Wang, R. Burgmann, (2005), Contemporary crustal deformation around the southeast borderland of the Tibetan Plateau, Journal of Geophysical research, 110, B11409.

Sol, S., A. Meltzer, R. Burgmann, R.D. van der Hilst, R. King, Z. Chen, P.O. Koons, E. Lev, Y.P. Liu, P.K. Zeitler, X. Zhang, J. Zhang and B. Zurek, (2007), Geodynamics of the southeastern Tibetan Plateau from seismic anisotropy and geodesy, Geology, 35, 563-566.

Wang, E., (1998), Late Cenozoic Xianshuihe-Xiaojian, Red River and Dali fault systems of southwestern Sichuan and central Yunnan, China, Spec. Pap, Geol. Soc, Am., 327.

Wang, E., B.C. Burchfiel, (2000), Late Cenozoic to Holocene deformation in southwestern Sichuan and adjacent Yunnan, China, and its role in formation of the southeastern part of the Tibetan Plateau, Geol. Soc. Am. Bull., 112, 413-423.

Xu, L., S. Rondenay, and R. D. van der Hilst, (2007), Structure of the crust beneath the southeastern Tibetan Plateau from teleseismic receiver functions, *Phys. Earth Planet. Int.*, 165, 176-193, doi: 10.1016/j.pepi.2007.09.002.

Yao, H., R. D. van der Hilst, and M. V. De Hoop, (2006), Surface-wave array tomography in SE Tibet from ambient seismic noise and two-station analysis – I. Phase velocity maps, *Geophys. J. Int.*, 166, 732-744, doi: 10.1111/j.1365-246X.2006.03028.x.

Yao, H., C. Beghein, and R.D. Van der Hilst, (2008), Surface wave array tomography in SE Tibet from ambient seismic noise and two-station analysis – II. Crustal- and upper-mantle structure, Geoohys. J. Int., 173, 205-219.

Zhang, H., S. Roecker, C.H. Thurber, and W. Wang (2012), Seismic Imaging of Microblocks and Weak Zones in the Crust Beneath the Southeastern Margin of the Tibetan Plateau, Earth Sciences, Dr. Imran Ahmad Dar (Ed.), ISBN: 978-953-307-861-8, 159-202.

Table 1-1: Comparison of traditional and Eikonal tomography

	Traditional tomography	Eikonal tomography
Equation	$t(\mathbf{r}, \mathbf{r}_s) = \int \frac{1}{c(\mathbf{r})} dr$	$\nabla t(\mathbf{r}, \mathbf{r}_s) = \frac{1}{c(\mathbf{r})} \hat{\mathbf{k}}$
Wavespeed calculation	Matrix inversion	Interpolation and derivation
Advantage	Good resolution; Well-developed	Fast; Accurate direction
Application in this thesis	Isotropic V_{SV} and V_{SH}; Radial anisotropy	Azimuthal anisotropy

Here $t(\mathbf{r}, \mathbf{r}_s)$ is the traveltime from source $\mathbf{r}_s$ to location $\mathbf{r}$, $c(\mathbf{r})$ is the local wavespeed, and $\hat{\mathbf{k}}$ is the unit vector along wave propagation direction.

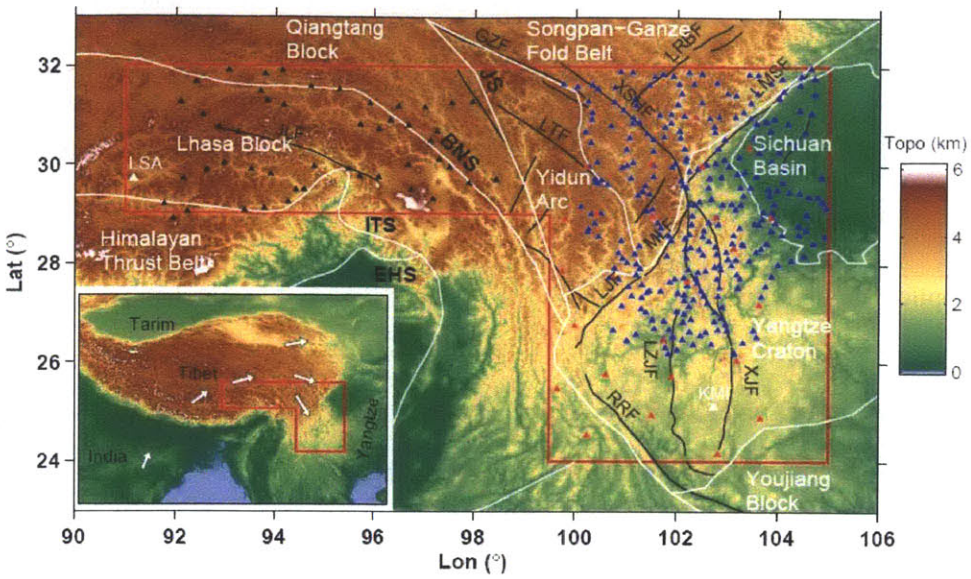

Figure 1-1. Topography, geological units and seismic stations used in this thesis. The topography is represented by the background color. The locations of seismic stations are depicted as black, red, and blue triangles for Lehigh, MIT, and CEA arrays, respectively. The two permanent stations KMI and LSA are depicted as white triangles. The white curves depict the boundaries of the geological units: Lhasa block, Qiangtang block, Yidun Arc, Songpan-Ganze fold belt and Yangtze Craton including the Sichuan Basin. Major faults are depicted as thin black lines and the abbreviations are: Ganze fault (GZF), Longriba fault (LRBF), Xianshuihe fault (XSHF), Longmenshan fault (LMSF), Longquan fault (LQF), Litang fault (LTF), Chenzhi fault (CZF), Lijian fault (LJF), Muli fault (MLF), Anninghe fault (ANHF), Zemuhe fault (ZMHF), Xiaojiang fault (XJF), Shimian fault (SMF), and Luzhijiang fault (LZJF) (after Wang et al., 1998; Wang and Burchfiel, 2000; Shen et al., 2005). Other abbreviations are: Eastern Himalayan Syntaxis (EHS), Jingsha Suture (JS), Bangong-Nujiang Suture (BNS), and Indus-Tsangpo Suture (ITS). The inset shows the location of our study region in the background of the whole Tibetan Plateau and its surrounding areas. The white arrows show the approximate surface motion relative to the Yangtze Craton from GPS observations (Shen et al., 2005).

Chapter 2

Radial anisotropy in the crust of SE Tibet and SW China from ambient noise interferometry[1]

Abstract

We use Rayleigh and Love wave Green's functions estimated from ambient seismic noise to study crustal structure and radial anisotropy in the tectonically complex and seismically active region west of the Sichuan Basin and around the Eastern Himalaya Syntaxis. In agreement with previous studies, low velocity zones are ubiquitous in the mid-lower crust, with substantial variations both laterally and vertically. Discrepancies between 3-D shear velocity from either Rayleigh (V_{SV}) or Love (V_{SH}) waves are examined both in view of non-uniqueness of tomographic solutions and radial anisotropy. Low shear wave speed and radial anisotropy with $V_{SH} > V_{SV}$ are most prominent in mid-lower crust in area northwest to the Lijiang-Muli fault and around the Red River and Xiaojiang faults. This anisotropy could be caused by sub-horizontal mica fabric and its association with low velocity zones suggests mica alignment due to flow in deep crustal zones of relatively low mechanical strength.

[1] Published as (except Appendix 2B): Huang, H., H. Yao, and R. D. van der Hilst, (2010), Radial anisotropy in the crust of SE Tibet and SW China from ambient noise interferometry, *Geophys. Res. Lett.*, 37, L21310, doi: 10.1029/2010GL044981.

2.1 Introduction

Despite decades of research, the mechanism of crustal deformation and eastward expansion of the Tibetan Plateau are still under debate. As the conjunction between the Tibetan Plateau and the Yangtze Indo-China blocks and the southern end of the trans-China seismicity belt, SE Tibet is of particular interest. GPS data (Zhang et al., 2004; Shen et al., 2005) and geological studies (Wang, 1998; Wang and Burchfiel, 2000) show that in this region the upper crust rotates clockwise around the Eastern Himalayan Syntaxis. But how this surface motion is related to deformation at larger depth is not yet known.

Along with geological data, including constraints on shortening and uplift history, the topography of this region – in particular, the gentle slope from ~5 km on the Plateau to less than 1 km in the southeast and the steep margin west of the Sichuan Basin – was used by Royden et al. (1997) to argue for flow in the deep crust. The area is intersected, however, by major fault systems, such as the Red River, Lijiang-Muli, Xianshuihe-Xiaojiang, and Longmenshan faults (Figure 2-1), which seismicity and GPS measurements (Shen et al., 2005) indicate are active block boundaries. These observations mostly pertain to the (near) surface, and more direct information about the deeper crust is needed to understand the large scale deformation this region.

On the one hand, recent discoveries of low velocity zones (LVZs) in middle and lower crust (Xu et al., 2007; Yao et al., 2008, 2010; Li et al., 2009), high Poisson's ratio (Hu et al., 2005; Xu et al., 2007), high heat flow (Hu et al., 2000), and low electrical resistivity (Bai et al., 2010) suggest that at least locally the deep crust is

mechanically weak. Furthermore, the change in pattern of azimuth anisotropy from upper crust to upper mantle (Yao et al., 2010) suggests that the crust and mantle deform differently. These inferences are qualitatively consistent with ductile flow in the deep crust (Royden et al., 1997, 2008). On the other hand, the edges of some LVZs seem to coincide with faults (Yao et al., 2008, 2010) where GPS data reveal large slip rates (Shen et al., 2005). Combined, these observations suggest that the tectonic evolution and deformation of SE Tibet is influenced by the juxtaposition of crustal blocks with or without weak zones, separated by major faults (Yao et al., 2010).

Radial anisotropy, that is, the difference in propagation speed of horizontally and vertically polarized waves – inferred, respectively, from Love and Rayleigh wave data – has been used to diagnose specific styles of crustal deformation (Shapiro et al., 2004; Moschetti et al., 2010). For example, crustal flow can produce a horizontal mica fabric, which, in turn, can produce significant radial anisotropy (e.g., Weiss et al., 1999; Shapiro et al., 2004). Following our work on crustal heterogeneity and azimuthal anisotropy in the southeastern margin of Tibet (Yao et al., 2008, 2010), we determine radial anisotropy from ambient noise tomography (e.g., Shapiro et al., 2005; Yao et al., 2006) with empirical Green's functions (EGFs) for short- and intermediate period Rayleigh and Love wave propagation. A major objective of this study is to establish spatial correlations between LVZs and the type and strength of radial anisotropy.

2.2 Data and method

It is now well established that cross correlation of ambient noise recorded at two seismic stations can be used to measure the Green's function, hereinafter referred to as the empirical Green's function (EGF), of wave propagation between these stations (see auxiliary material, Section 1) (Lobkis and Weaver, 2001; Weaver and Lobkis, 2004; Roux et al., 2005). For our study in SE Tibet we estimate Rayleigh wave EGFs from vertical component and Love wave EGFs (Figure 2A-1a,b) from transverse component data recorded in 2003 and 2004 at a temporary array of 25 stations in SE Tibet and at KMI (Kunming, Yunnan), a permanent station of the global seismograph network (Figure 2-1).

Following Yao et al. (2006, 2008) we use a 3-step procedure to invert for 3-D shear wave velocity variations. In the first step, we measure phase velocity dispersion curves for appropriate station pairs (Figure 2A-1c,d). In the second step, we use these dispersion curves to construct phase velocity maps at different periods (7-40s); for each point on a 0.5°-by-0.5° grid, phase velocities are then calculated for a range of frequencies. As an example, dispersion curves of Rayleigh and Love waves at grid point (26°N, 102°E) are presented in Figure 2-2a. Finally, we use the neighborhood algorithm (NA) (Sambridge, 1999a, 1999b) to invert (for each grid-point) the dispersion data for variations of V_{SV} and V_{SH} with depth (Figure 2-2b); these 1-D profiles are combined into 3-D V_{SV} and V_{SH} models (Figure 2A-2).

The starting model for the 1-D inversion, after Yao et al. (2008), has an upper, middle, and lower crust, and the Moho depth is constrained by receiver function

analysis (Hu et al., 2005; Xu et al., 2007). To reduce the number of free parameters, V_P is scaled to V_{SV} using receiver function results (Hu et al., 2005; Xu et al., 2007), and ρ is related to V_P using empirical relations by Brocher (2005).

2.3 Shear wave velocity structure and radial anisotropy

The V_{SV} model obtained here from ambient noise interferometry agrees with the results that Yao et al. (2008) obtained from a combination of ambient noise interferometry and two-station analysis. In particular, LVZs are prominent in the middle and lower crust and some are bounded by faults, such as the Xianshuihe and Lijiang-Muli faults (Figure 2A-2 of the auxiliary material).

V_{SV} and V_{SH} are generally similar in the upper crust and upper mantle, but large differences occur in the middle and lower crust. A comparison of Love wave dispersion calculated from V_{SV} profiles (obtained from vertical component data) with the observed dispersion shows that these differences (and, hence, the implied radial anisotropy) are required by our data. For example, Figure 2-2a shows that for (25°N, 102°E) Love wave dispersion calculated from V_{SV} (cyan dashed line) is inconsistent with the observations (top red line with 1σ error bars), which are explained well by the V_{SH} model (black line).

We quantify radial anisotropy, ψ, as $2(V_{SH}-V_{SV})/(V_{SH}+V_{SV})*100\%$. In the upper crust ψ is less than 2% (Figure 2-3a), which we consider insignificant. In the middle and lower crust V_{SH} is generally larger than V_{SV} (Figures 2-3b,c and 2-4), but strong anisotropy ($\psi > 5\%$) is detected in Songpan-Ganze block and in the southern part of

our study region, between the Red River and the Xiaojiang fault. In the center of the study area a zone of relatively high V_{SV} ($\psi < 0$) is present in the middle and lower crust (Figures 2-3b,c and 2-4). We note that uncertainty in the Moho depth only has a small effect on the estimate of radial anisotropy discussed here (see auxiliary material, Section 3).

2.4 Discussion and conclusions

GPS data (Shen et al., 2005) suggest different surface velocities in areas bounded by the Xianshuihe-Xiaojiang, Litang, Lijiang-Muli, and Red River faults. Our current and previous studies reveal substantial crustal heterogeneity, and the tomographically observed contrasts across the Litang, Red River, and Xiaojiang faults at shallow depth (Figure 2A-2a,d) and the Lijiang-Muli and Xianshuihe-Xiaojiang faults in the middle crust (Figure 2A-2b,e) suggest that these faults are indeed major tectonic boundaries. Combined with other geophysical observables (e.g., heat flow, resistivity, Poisson's ratio) the anomalously low shear velocities indicate low (mechanical) rigidity (Yao et al., 2008, 2010). The ubiquitous LVZs may thus represent loci of ductile deformation in the deep crust. By themselves, however, they do not provide unequivocal evidence for horizontal flow.

Our analysis of short-to-intermediate period horizontal and vertical component data suggests that, in general, radial anisotropy is weak at shallow depth but strong in the deep crust (with V_{SH} significantly larger than V_{SV}, that is, $\psi > 0$) (Figures 2-3 and 2-4). Interestingly, strong radial anisotropy occurs near the LVZs (that is, low V_{SV})

that were detected by Yao et al. (2008) and which are confirmed here. Indeed, in the middle crust of the Songpan-Ganze block and the part of the Yangtze craton between the Red River and Xiaojiang faults, V_{SV} is low and ψ is large ($V_{SH} > V_{SV}$). This is not always the case, however. Near the north end of the Luzhijiang fault, for instance, V_{SV} is relatively high and larger than V_{SH} ($\psi < 0$). We note that radial anisotropy here may not be significant since Love wave dispersion is, within error, consistent with the V_{SV} model (Figure 2-2c-d). The contrast with surrounding areas suggests that the small region confined by the Xianshuihe and Muli fault is relatively stable sub-block in the westernmost part of the Yangtze craton.

For a more quantitative analysis of the relationship between wavespeed and radial anisotropy we plot radial anisotropy (ψ) versus shear velocity ($d\ln V_{SV}$) for different tectonic regions and crust layers. In the upper crust (Figure 2-5a) radial anisotropy is small (less than 2%) and there is no correlation between V_{SV} and ψ. However, in the middle and lower crust, Figure 2-5b,c reveal a strong (negative) correlation between wavespeed and radial anisotropy in the lower crust beneath the western part of the study area (the Songpan-Ganze block, the westernmost part of the Yangtze craton and the Lhasa block) with LVZs (that is, $d\ln V_{SV} < 0$) coinciding with areas where $V_{SH} > V_{SV}$ (that is, $\psi > 0$). We also note that the LVZs themselves cannot simply be explained by radial anisotropy (see auxiliary material, Section 4, Figure 2A-6).

Radial anisotropy in the deep crust (with $V_{SH} > 0$) can be produced by a preferred orientation of mica crystals (Weiss et al., 1999; Nishizawa and Yoshitno, 2001). Shapiro et al. (2004) invoked a sub-horizontal mica fabric to explain radial anisotropy

inferred from Love and Rayleigh wave propagation and to argue for thinning and lateral (channel) flow in the deep crust of Central Tibet. The strong radial anisotropy in and near LVZs inferred here may thus suggest (flow-induced) sub-horizontal alignment of mica in the mechanically weak zones of the deep crust beneath SE Tibet and SW China. This is consistent with deep crustal channel flow (e.g., Royden et al., 1997), but lateral heterogeneity and the major faults in the region likely play an important role in controlling the pattern of such flow.

Appendix 2A

2A-1: Construction of Empirical Green's Functions (EGFs):

For diffuse fields the time derivative of cross-correlation function of seismic noise records at two stations is equal to the Green's function between these two positions except for an amplitude factor (Lobkis and Weaver, 2001; Weaver and Lobkis, 2004; Roux et al., 2005):

$$\frac{dC_{AB}(t)}{dt} = -G_{AB}(t) + G_{BA}(-t) \qquad (2A.1)$$

where $C_{AB}(t)$ and $G_{AB}(t)$ are, respectively, the cross-correlation function and the empirical Green's function (EGF) between two locations A and B. Using a time window of one year, we estimate Rayleigh wave EGFs from vertical component and Love wave EGFs (Figure 2A-1a,b) from transverse component data. Uneven distribution of noise sources can produce asymmetry of G_{AB} and G_{BA} (Sabra et al., 2005; Yao et al., 2006) and for our analysis we stack the two parts. Examples of EGFs

for both Rayleigh and Love wave, which are the data used in our study, are shown in Figure 2A-1.

2A-2: Crustal Heterogeneity

In Figure 2A-2 we present for three depths in the crust the lateral variation in wavespeed as inferred from Rayleigh wave EGFs (that is, V_{SV}) and Love waves (that is, V_{SH}), as well as the average wavespeed $(V_{SV} + V_{SH})/2$.

2A-3: Trade-off between the Moho Depth and Estimates of Radial Anisotropy in the Crust

A classical problem in crustal imaging is the trade-off between volumetric wavespeed variations and the depth to contrasts in elasticity. In our study, we constrain the depth to the crust-mantle interface, also referred to as the Moho, using results from receiver function analysis (Hu et al., 2005; Xu et al., 2007). But these constraints have uncertainties, and we have to investigate the effect of incorrect Moho depth on the tomographically inferred wavespeed variations. For this reason we investigate the effect if Moho is 5 km deeper than inferred from receiver functions (Figure 2A-3). The changes of radial anisotropy due to this effect are of the order of 1-2% (Figure 2A-3b), which is much smaller than the absolute value of anisotropy (Figure 2A-3a). Actual uncertainty in the Moho depth for receiver function analysis is probably less than 5 km, and this test confirms that the effect of the Moho depth error do not invalidate any of the main conclusions on radial anisotropy.

2A-4: Radial Anisotropy and Shear Velocity

To understand the geological meaning of our results better, we investigate the relationship of radial anisotropy and shear velocity anomaly. For this purpose we subdivide the study area into 6 sub-regions according to major faults and block boundaries: the Songpan-Ganze block, the Lhasa block, the Sichuan Basin, the western and eastern part of the Yangtze craton bordered by the Xianshuihe-Xiaojiang fault system, and the Youjiang block (Figure 2A-4).

As shown in Figure 2-5, a clear correlation between V_{SV} anomaly ($\mathrm{dln}V_{SV}$) and radial anisotropy (ψ) is observed in middle and lower crust. However, the relationship between $\mathrm{dln}V_{SH}$ and ψ is not that direct. Both shear wavespeeds (V_{SV} and V_{SH}) would decrease in areas where temperature is relatively high, but only V_{SH} increase due to the sub-horizontal alignment of mica fabric. In our study area both may occur, which makes the relationship between V_{SH} and ψ less clear than that of V_{SV} and ψ (Figure 2A-5).

We need to consider the possibility that the low V_{SV} zone is only caused by the radial anisotropy. If that were the case, however, we would observe a negative correlation between V_{SV} and V_{SH}. The fact that we see the opposite (Figure 2A-6) demonstrates that the occurrence of the LVZ cannot be explained by radial anisotropy and must thus have a different origin (such as high temperature). In the upper crust, the models center at the origin point, which means in average there is no significant radial anisotropy and shear wave speed anomaly. But in the middle and lower crust, the distribution of our models move to the bottom left, which indicates on average our

shear wave speed model is lower than the reference and V_{SV} is smaller than V_{SH}.

Appendix 2B

The methodology in the main text can be applied to a larger region using seismic noise records from two temporary arrays: the array deployed by MIT (as in the main text) and an array by Lehigh University (Figure 2B-1). We use seismic records between November 2003 and August 2004. Green's functions for Rayleigh and Love waves are extracted from the cross-correlations of the noise records of vertical and transverse components, respectively. Phase velocities (or dispersion curves) for both Rayleigh and Love waves are measured from the Green's functions. Then shear wavespeeds are inverted from the measured dispersion curves.

The obtained shear wavespeed V_{SV} and radial anisotropy are shown in Figures 2B-2 to 2B-5. In the eastern part of the study region, which is covered by the MIT array, both the wavespeed and radial anisotropy reveal similar patterns as those inverted from MIT array data only. The most dominant feature is the widespread low wavespeed zones with positive radial anisotropy in the middle and lower crust. In the western part of the study region, which is covered by the Lehigh array, we also observe ubiquitous low wavespeed anomalies and positive radial anisotropy in the middle and lower crust. A negative correlation between V_{SV} and radial anisotropy is observed in the middle and lower crust for the entire study region (Figure 2B-6).

Acknowledgments

We thank two anonymous reviewers for their constructive comments, which helped us improve the manuscript. We also thank the Editor Michael Wysession for his assistance. This work was supported by NSF grant EAR-0910618.

References

Bai, D., M. J. Unsworth, M. A. Meju, X. Ma, J. Teng, X. Kong, Y. Sun, J. Sun, L. Wang, C. Jiang, C. Zhao, P. Xiao, and M. Liu, (2010), Crustal deformation of the eastern Tibetan plateau revealed by magnetotelluric imaging, *Nature Geosci.*, 3, 358-362, doi:10.1038/ngeo830.

Brocher, T. M., (2005), Empirical relations between elastic wavespeeds and density in the Earth's crust, *Bull. Seism. Soc. Am.*, 95(6), 2081-2092, doi: 10.1785/0120050077.

Hu, J., Y. Su, X. Zhu, and Y. Chen, (2005), S-wave velocity and Poisson's ratio structure of crust in Yunnan and its implication (in Chinese), *Sci. China Ser. D*, 48(2), 210-218.

Hu, S., L. He, and J. Wang, (2000), Heat flow in the continental area of China: a new data set, *Earth planet. Sci. Lett.*, 179(2), 407-419, doi:10.1016/S0012-821X(00)00126-6.

Li, H., W. Su, C. Wang, and Z. Huang, (2009), Ambient noise Rayleigh wave tomography in western Sichuan and eastern Tibet, *Earth planet. Sci. Lett.*, 282, 201-211, doi:10.1016/j.epsl.2009.03.021.

Lobkis, O. I., and R. L. Weaver, (2001), On the emergence of the Green's function in the correlations of a diffuse field, *J. Acoust. Soc. Am.*, 110(6), 3011-3017.

Moschetti, M. P., M. H. Ritzwoller, F. C. Lin, and Y. Yang, (2010), Seismic evidence for widespread crustal deformation caused by extension in the western USA, *Nature*, 464, 885-889, doi:10.1038/nature08951.

Nishizawa, O., and T. Yoshitno, (2001), Seismic velocity anisotropy in mica-rich rocks: an inclusion model, *Geophys. J. Int.*, 145, 19-32, doi: 10.1111/j.1365-246X.2001.00331.x.

Roux, R., K. G. Sabra, W. A. Kuperman, and A. Roux, (2005), Ambient noise cross correlation in free space: Theoretical approach, *J. Acoust. Soc. Am.*, 117(1), 79-84.

Royden, L. H., B. C. Burchfiel, R. W. King, E. Wang, Z. Chen, F. Shen, and Y. Liu, (1997), Surface deformation and lower crustal flow in eastern Tibet, *Science*, 276, 788-790, doi: 10.1126/science.276.5313.788.

Royden, L. H., B. C. Burchfiel, and R. D. van der Hilst, (2008), The geological evolution of the Tibetan plateau, *Science*, 321, 1054-1058, doi: 10.1126/science.1155371.

Sabra, K. G., P. Gerstoft, P. Roux, W. A. Kuperman, and M.C. Fehler, (2005), Extracting time-domain Green's function estimates from ambient seismic noise, *Geophys. Res. Lett.*, 32, L03310, doi:10.1029/2004GL021862.

Sambridge M., (1999a), Geophysical inversion with a neighborhood algorithm –I. Searching a parameter space, *Geophys. J. Int.*, 138(2), 479-494, doi: 10.1046/j.1365-246X.1999.00876.x.

Sambridge M., (1999b). Geophysical inversion with a neighborhood algorithm –II. Appraising the ensemble, *Geophys. J. Int.*, 138(3), 727-746, doi: 10.1046/j.1365-246x.1999.00900.x.

Shapiro, N. M., M. H. Ritzwoller, P. Molnar, and V. Levin, (2004), Thinning and flow of Tibetan crust constrained by seismic anisotropy, *Science*, 305, 233-236, doi: 10.1126/science.1098276.

Shapiro, N. M., M. Campillo, L. Stehly, and M. H. Ritzwoller, (2005), High-resolution surface-wave tomography from ambient seismic noise, *Science*, 307, 1615-1618, doi: 10.1126/science.1108339.

Shen, Z., J. Lv, M. Wang, and R. Burgmann, (2005), Contemporary crustal deformation around the southeast borderland of the Tibetan Plateau, *J. Geophys. Res.*, 110, B11409, doi:10.1029/2004JB003421.

Wang, E., (1998), Late Cenozoic Xianshuihe-Xiaojian, Red River and Dali fault systems of southwestern Sichuan and central Yunnan, *China, Spec. Pap, Geol. Soc, Am.*, 327.

Wang, E., and B. C. Burchfiel, (2000), Late Cenozoic to Holocene deformation in southwestern Sichuan and adjacent Yunnan, China, and its role in formation of the southeastern part of the Tibetan Plateau, *Geol. Soc. Am. Bull.*, 112, 413-423, doi: 10.1130/0016-7606(2000)112<413:LCTHDI>2.0.CO;2.

Weaver, R., and O. I. Lobkis, (2004), Diffuse fields in open systems and the emergence of the Green's function (L), *J. Acoust. Soc. Am.*, 116(5), 2731-2734.

Weiss, T., S. Siegesmund, W. Rabbel, T. Bohlen, and M.Pohl, (1999), Seismic Velocities and Anisotropy of the Lower Continental Crust: A Review, *Pure Appl. Geophys.*, 156, 97-122, doi: 10.1007/s000240050291.

Xu, L., S. Rondenay, and R. D. van der Hilst, (2007), Structure of the crust beneath the southeastern Tibetan Plateau from teleseismic receiver functions, *Phys. Earth Planet. Int.*, 165, 176-193, doi: 10.1016/j.pepi.2007.09.002.

Yao, H., R. D. Van der Hilst, and M. V. De Hoop, (2006), Surface-wave array tomography in SE Tibet from ambient seismic noise and two-station analysis – I. Phase velocity maps, *Geophys. J. Int.*, 166, 732-744, doi: 10.1111/j.1365-246X.2006.03028.x.

Yao, H., C. Beghein, and R. D. Van der Hilst, (2008), Surface wave array tomography in SE Tibet from ambient seismic noise and two-station analysis – II. Crustal- and upper-mantle structure, *Geoohys. J. Int.*, 173, 205-219, doi: 10.1111/j.1365-246X.2007.03696.x.

Yao, H., R. D. Van der Hilst, and J. P. Montagner, (2010), Heterogeneity and anisotropy of the lithosphere of SE Tibet from ambient noise and surface wave array tomography, J. Geophys. Res., doi:10.1029/2009JB007142, in press.

Zhang P., Z. Shen, and M. Wang, et al. (2004), Continuous deformation of the Tibetan Plateau from global positioning system data, *Geology*, 32(9), 809-812, doi: 10.1130/G20554.1.

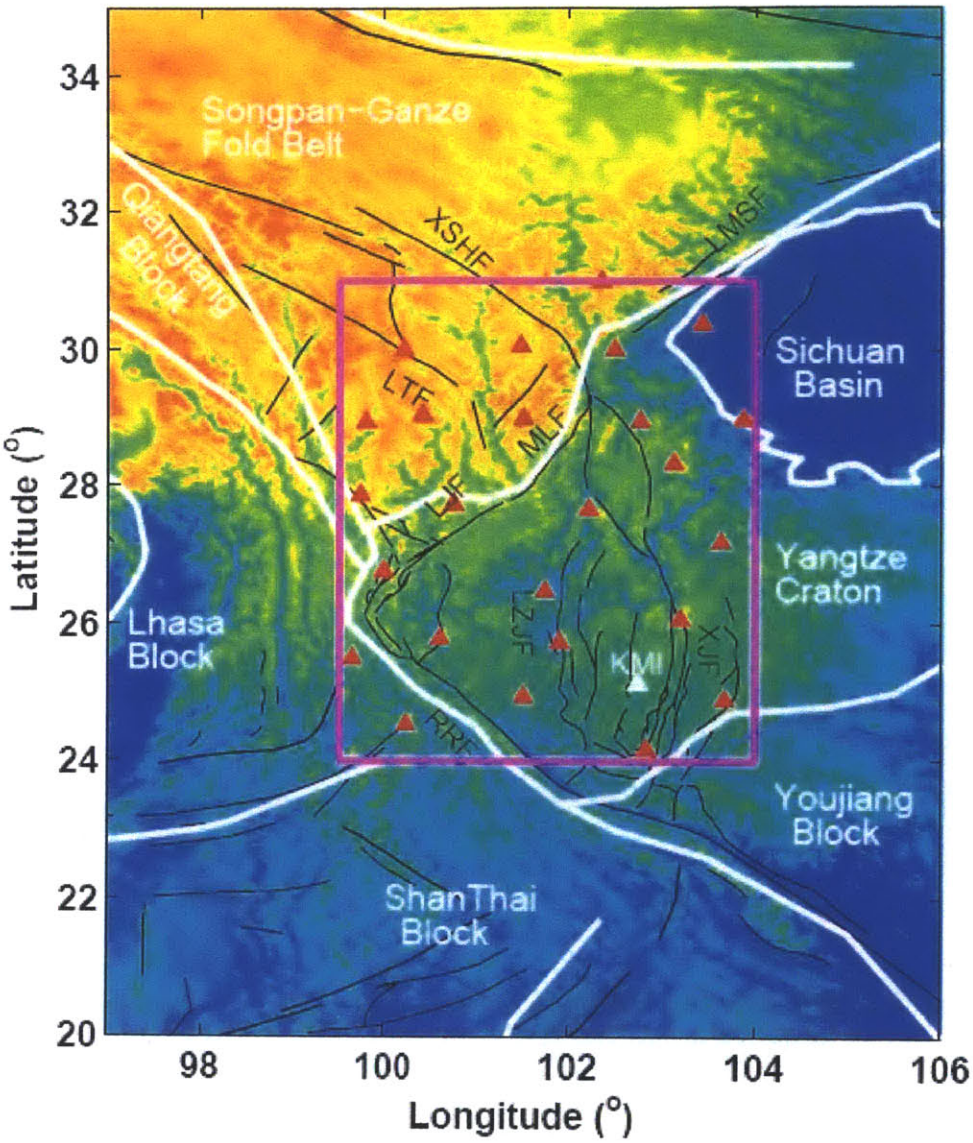

Figure 2-1. Location of the temporary broad-band array in Sichuan and Yunnan provinces of SW China (red triangles) and a permanent station KMI (white triangle) in Kunming, Yunnan. Black lines depict major faults (after Wang et al., 1998; Wang and Burchfiel, 2000; Shen et al., 2005) and white lines delineate tectonic boundaries. Magenta box shows the area of our study. Abbreviations: XSHF, Xianshuihe fault; LMSF, Longmenshan fault; LTF, Litang fault; LJF, Lijiang fault; MLF, Muli fault; LZJF, Luzhijiang fault; XJF, Xiaojiang fault; RRF, Red River fault.

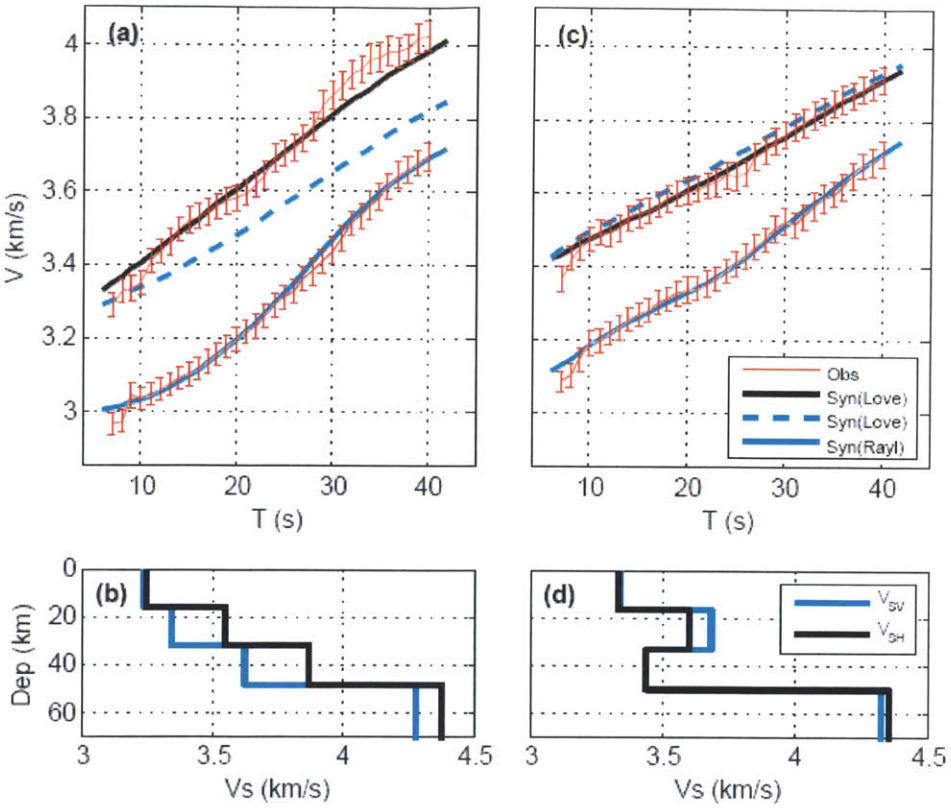

Figure 2-2. Rayleigh and Love phase velocity dispersion curves and shear wave speed models by the NA inversion at (25oN, 102oE) (a, b) and (27.5oN, 102oE) (c, d). (a) and (c): the red lines (with 1σ error bars) are observed phase velocity dispersion curves for Love (top) and Rayleigh (bottom) wave, respectively. The standard error σ is estimated from the seasonal variations of EGF (Yao et al., 2006). The black lines are the Love wave dispersion curves calculated from the VSH model in (b) and (d), and the solid cyan lines are the calculated Rayleigh wave dispersion curve from the VSV model in (b) and (d). The dashed cyan lines are the Love wave dispersion curve calculated from the VSV model. (b) and (d): VSH (black) and VSV (cyan) models obtained in NA inversion from the dispersion data shown in (a) and (c).

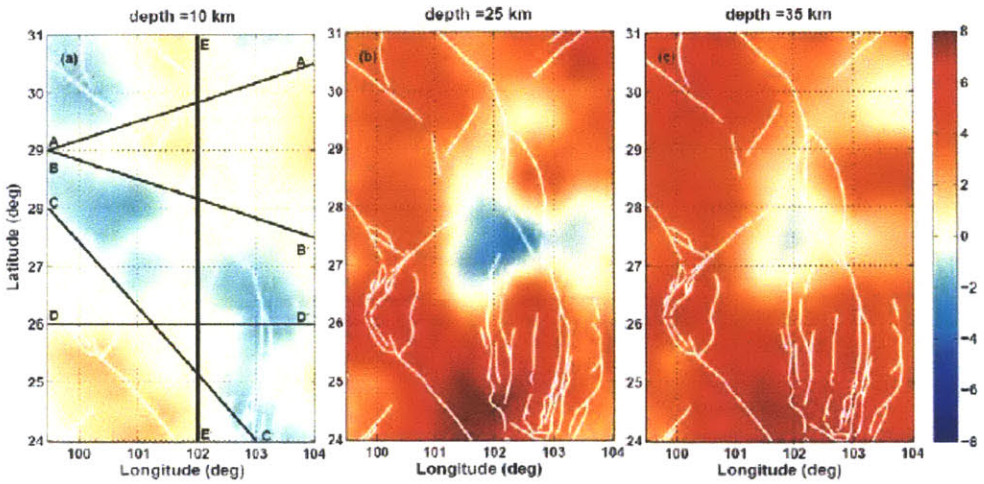

Figure 2-3. Radial anisotropy (ψ) defined as $2(V_{SH}-V_{SV})/(V_{SH}+V_{SV})*100$ (%), at (a) 10 km, (b) 25 km and (c) 35 km depth. Red depicts $V_{SH} > V_{SV}$ ($\psi > 0$); blue indicates $V_{SH} < V_{SV}$ ($\psi < 0$). White lines depict the major faults in our study area, and in (a) the thin black lines with letters at each end indicate the location of vertical profiles in Figure 2-4.

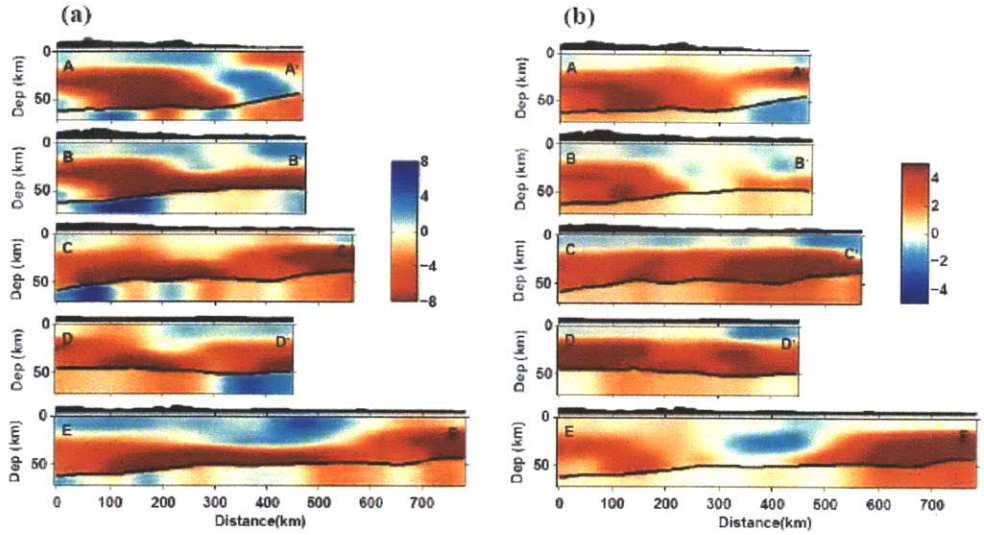

Figure 2-4. (a) The perturbation of shear wave velocity structure $d\ln V_{SV}$ (%), with red (blue) depicting slow (fast) shear wave propagation. Topography is shown above each profile. The black thick lines in each profile (around 50 km) depict the Moho discontinuity. The reference V_{SV} model in the curst is a 3 layered model with 3.3, 3.6, and 3.8 km/s in upper, middle and lower crust, which are inferred from the global Crust 2.0 model (http://mahi.ucsd.edu/Gabi/rem.html) by averaging Vs separately of the upper, middle, and lower crust for all locations with crustal thickness larger than 40 km. The reference V_{SV} in the upper mantle is the average of the whole study area. (b) Radial anisotropy, defined as $2(V_{SH}-V_{SV})/(V_{SH}+V_{SV})*100$ (%). Red represents $V_{SH} > V_{SV}$; and blue represents $V_{SH} < V_{SV}$.

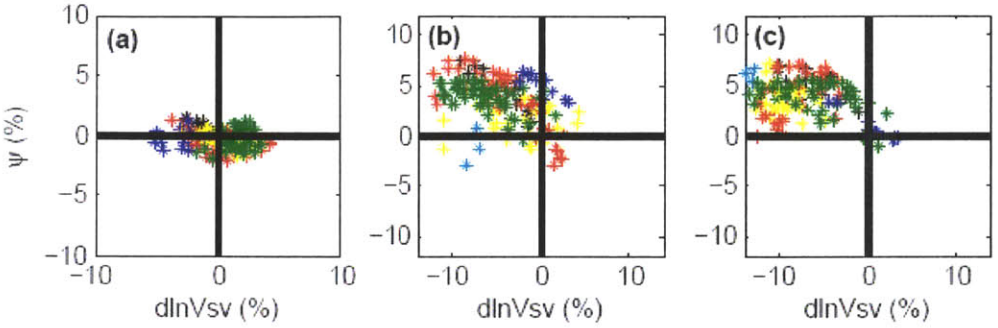

Figure 2-5. Relationship between relative V_{SV} anomalies (dlnV_{SV}) and radial anisotropy (ψ) for (a) upper crust, (b) middle crust, and (c) lower crust. Each symbol represents a grid point on map. Colors represent different tectonic regions (as defined in Figure 2A-4): the Songpan-Ganze block (green), the Lhasa block (black), the Sichuan Basin (blue), the part of the Yangtze craton west of the Xianshuihe-Xiaojiang fault system (red), the part of the Yangtze block east of the Xianshuihe-Xiaojiang fault system (yellow), and the Youjiang block (cyan).

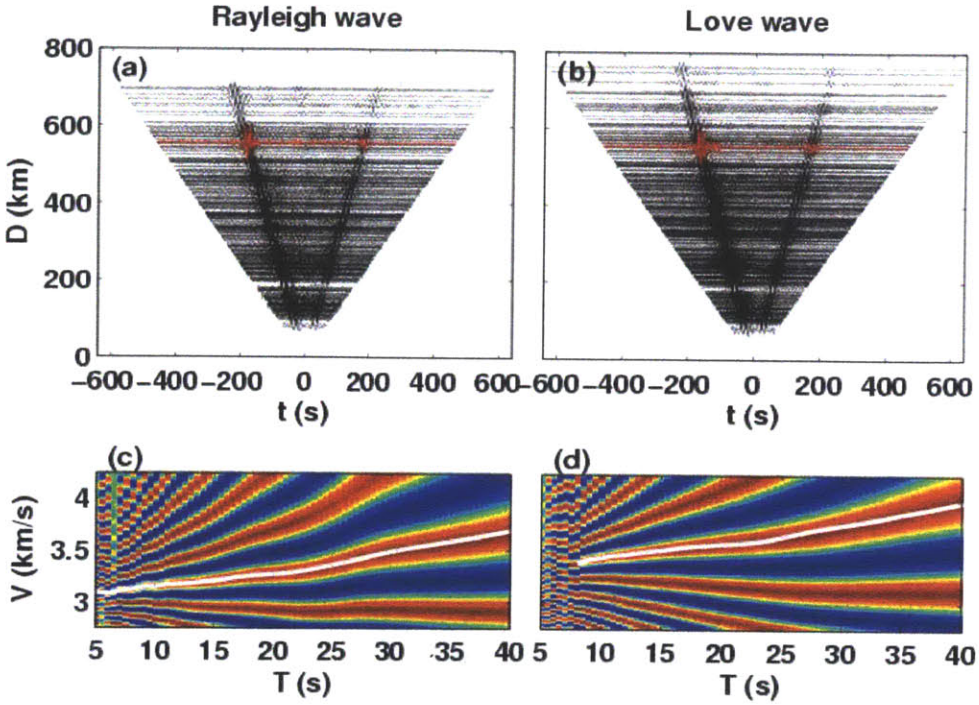

Figure 2A-1. (a)-(b) Band-pass filtered (8-40s) EGFs for Rayleigh and Love waves, respectively. The red curves (multiplied by a factor of 5) are the EGFs used in (c)-(d) to extract phase velocity dispersion curves by an image transformation technique (Yao et al., 2005). (c)-(d) Phase velocity dispersion measurements from the EGFs for Rayleigh and Love wave, respectively. The white lines depict the extracted dispersion curves.

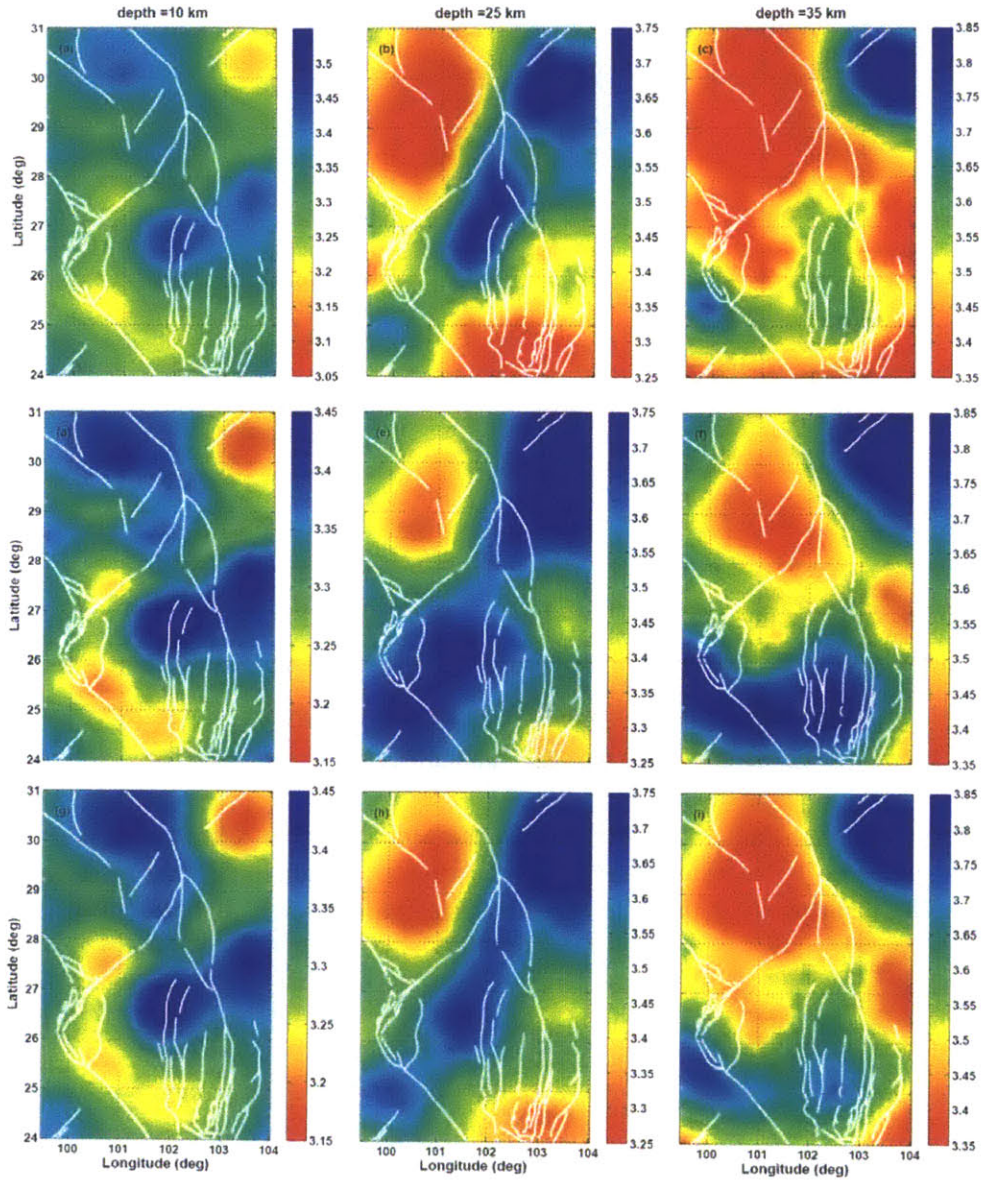

Figure 2A-2. Absolute wave speed (km/s) for Vsv (a)-(c), Vsh (d)-(f), and their average (g)-(i) at at 10 km, 25 km, and 35 km depth.

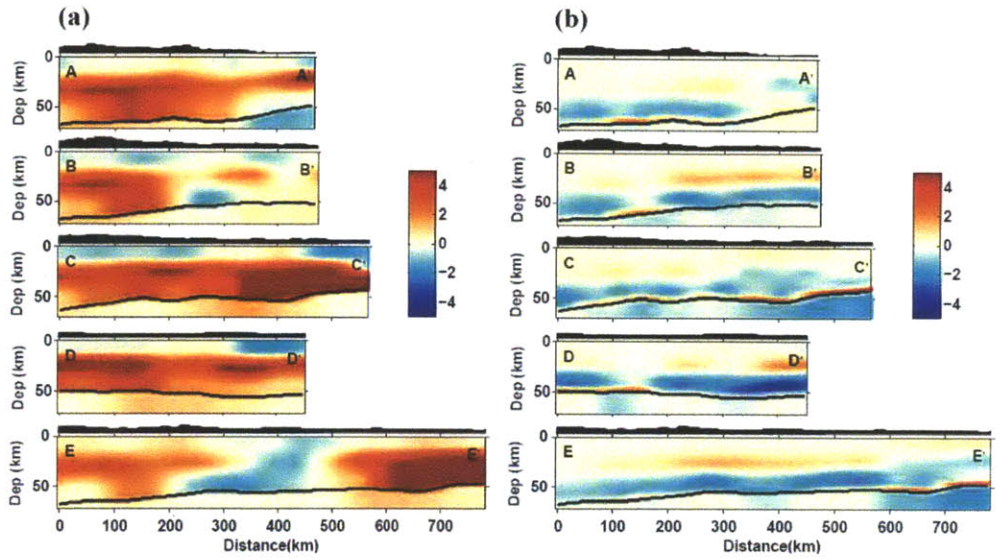

Figure 2A-3. (a) Radial anisotropy when the Moho depth is 5 km larger than that from the receiver function analysis; (b) the change of radial anisotropy due to the Moho depth change (e.g. the difference between Figure 2A-3a and Figure 2A-4b).

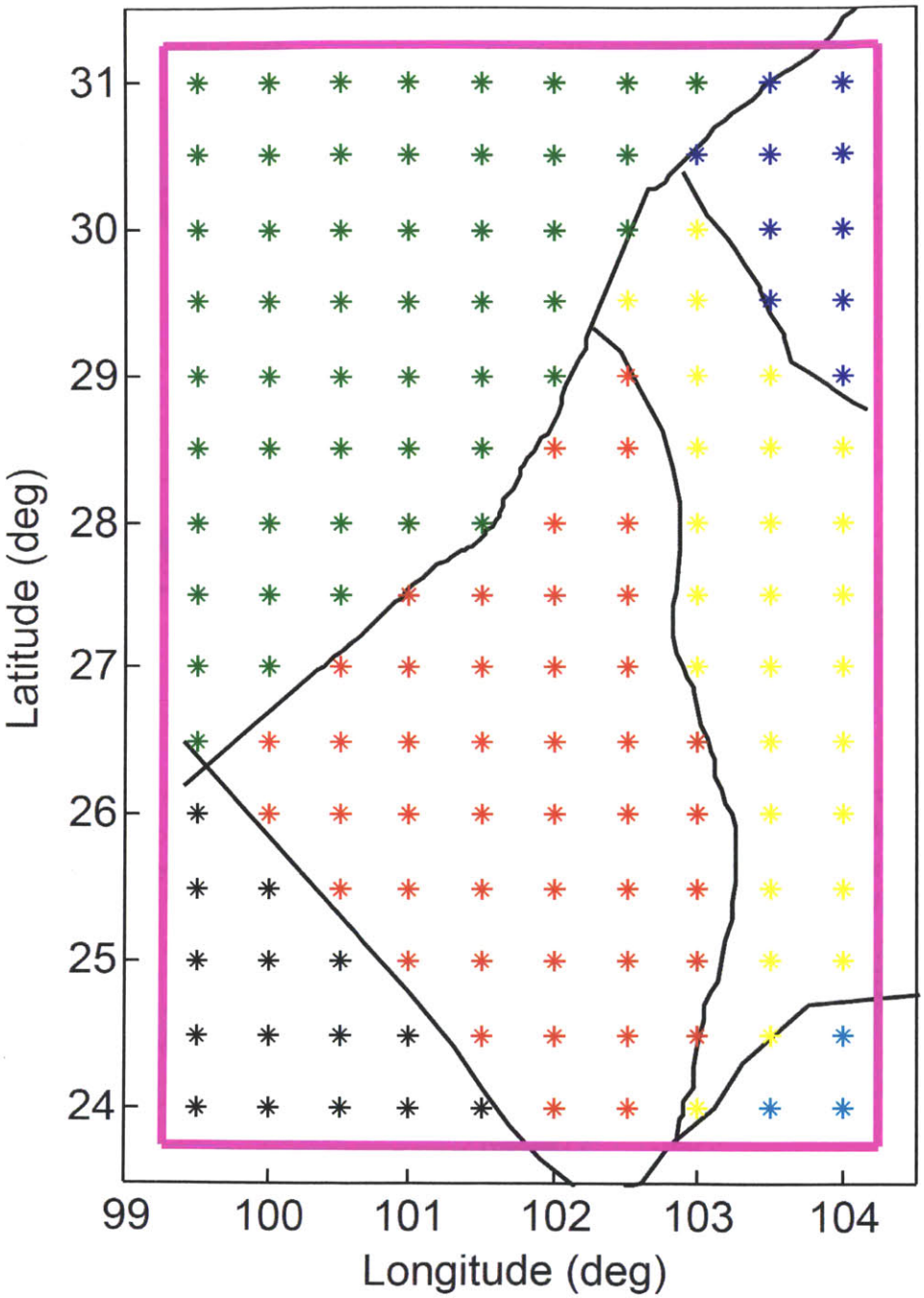

Figure 2A-4. The six main tectonic regions for our study area. Each star represents a grid point in the inversion. Black curves are either major faults or unit boundaries (Figure 2-1). Each cross represents a grid point in our inversion. Green: Songpan-Ganze block; black: Lhasa block, dark blue: Sichuan Basin; red: the Yangtze craton west to the Xianshuihe-Xiaojiang fault system; yellow: Yangtze block east to the Xianshuihe-Xiaojiang fault system; and cyan: Youjiang block.

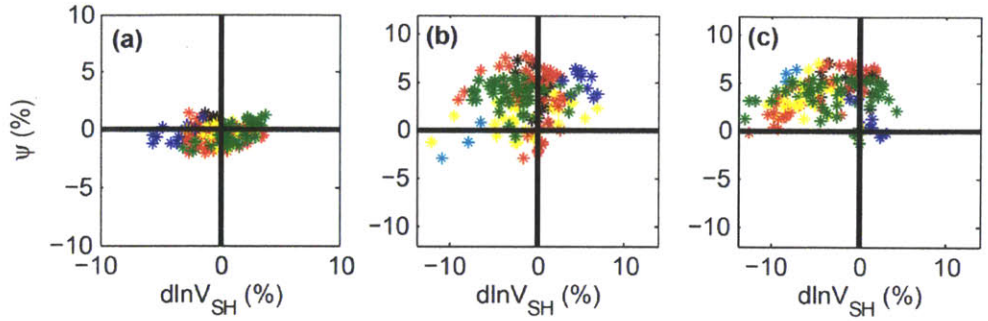

Figure 2A-5. Relationship between relative Vsv anomalies (dlnVsv) and radial anisotropy (ψ) for (a) upper crust; (b) middle crust and (c) lower crust. Each cross represents a grid point on map. Colors represent different tectonic regions defined in Figure 2A-4.

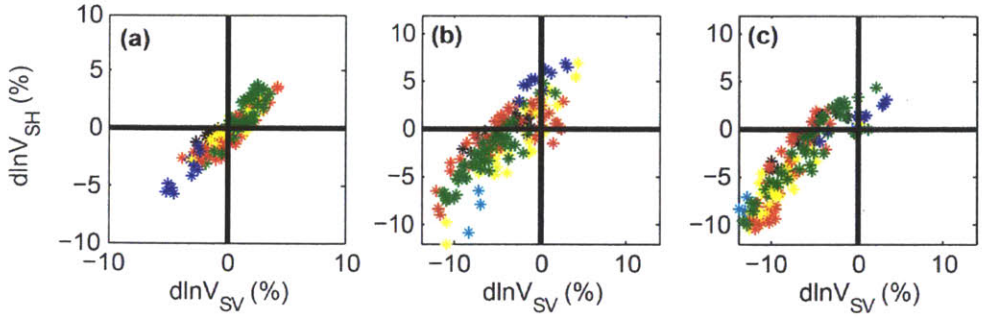

Figure 2A-6. Relationship between relative Vsv anomaly (dlnVsv) and Vsh anomaly (dlnVsh) for (a) upper crust; (b) middle crust and (c) lower crust. Each cross represents a grid point on map. Colors represent different tectonic regions defined in Figure 2A-4.

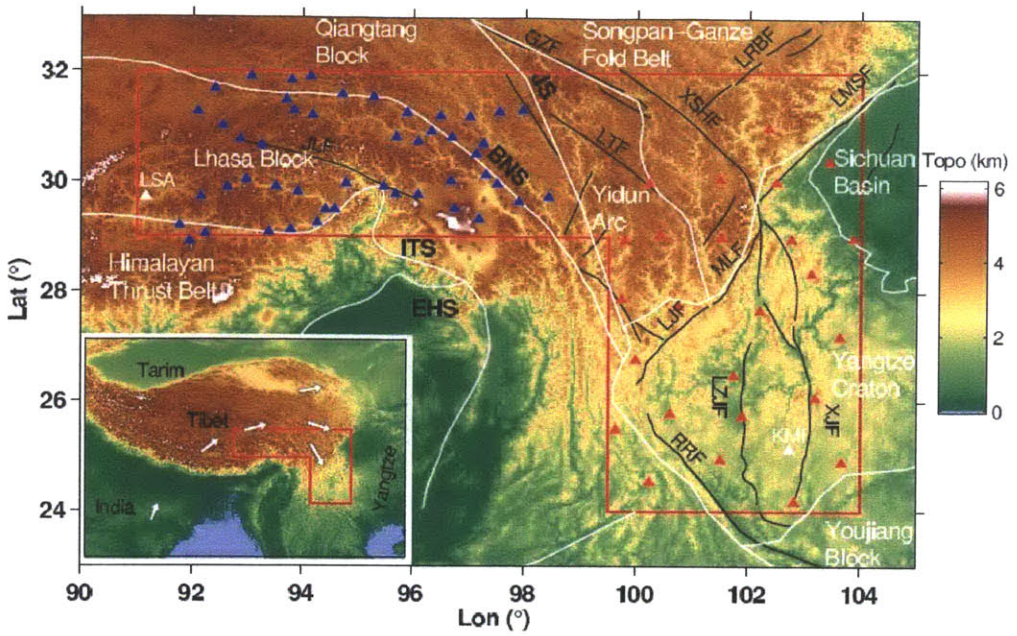

Figure 2B-1. Topography, geological units and seismic stations used in this study. The topography is represented by the background color. The locations of seismic stations are depicted as blue and red triangles for Lehigh and MIT arrays, respectively. The two permanent stations KMI and LSA are depicted as white triangles. The white curves depict the boundaries of the geological units: Lhasa block, Qiangtang block, Yidun Arc, Songpan-Ganze fold belt and Yangtze Craton including the Sichuan Basin. Major faults are depicted as thin black lines and the abbreviations are: Ganze fault (GZF), Longriba fault (LRBF), Xianshuihe fault (XSHF), Longmenshan fault (LMSF), Longquan fault (LQF), Litang fault (LTF), Chenzhi fault (CZF), Lijian fault (LJF), Muli fault (MLF), Anninghe fault (ANHF), Zemuhe fault (ZMHF), Xiaojiang fault (XJF), Shimian fault (SMF), and Luzhijiang fault (LZJF) (after Wang et al., 1998; Wang and Burchfiel, 2000; Shen et al., 2005). Other abbreviations are: Eastern Himalayan Syntaxis (EHS), Jingsha Suture (JS), Bangong-Nujiang Suture (BNS), and Indus-Tsangpo Suture (ITS). The inset shows the location of our study region, depicted by the red box, in the background of the whole Tibetan Plateau and its surrounding areas. The white arrows show the approximate surface motion relative to the Yangtze Craton from GPS observations (Zhang et al., 2004; Shen et al., 2005).

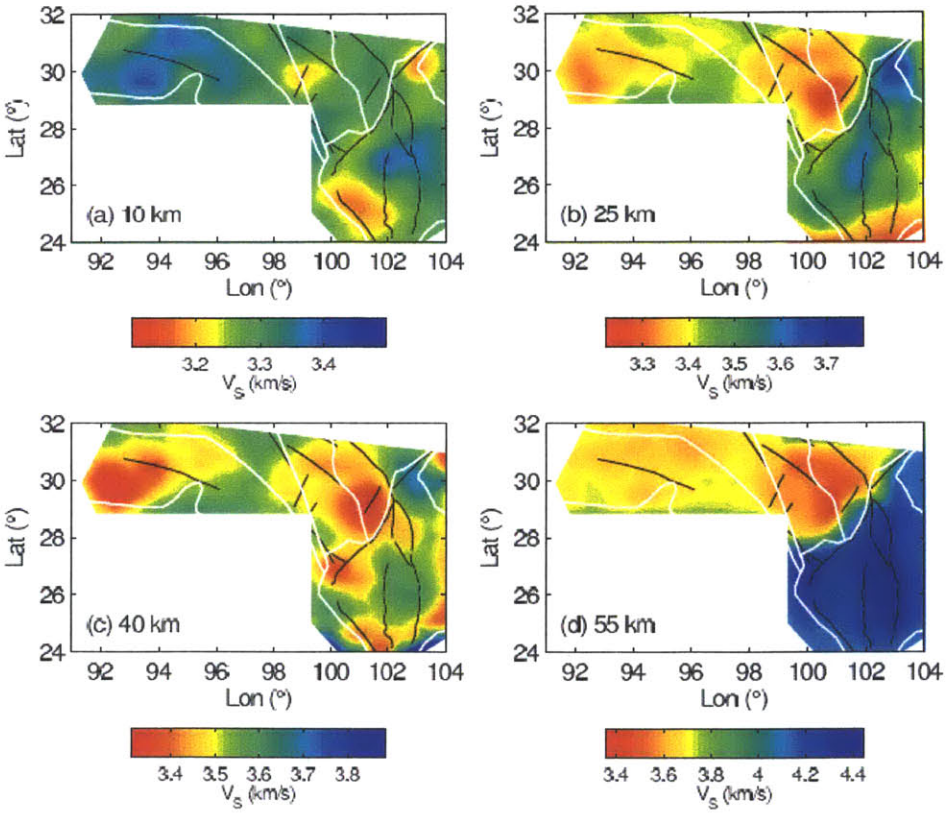

Figure 2B-2. The variations of the vertically polarized shear wavespeed (V_{SV}) at (a) 10 km; (b) 25 km; (c) 40 km; and (d) 55 km.

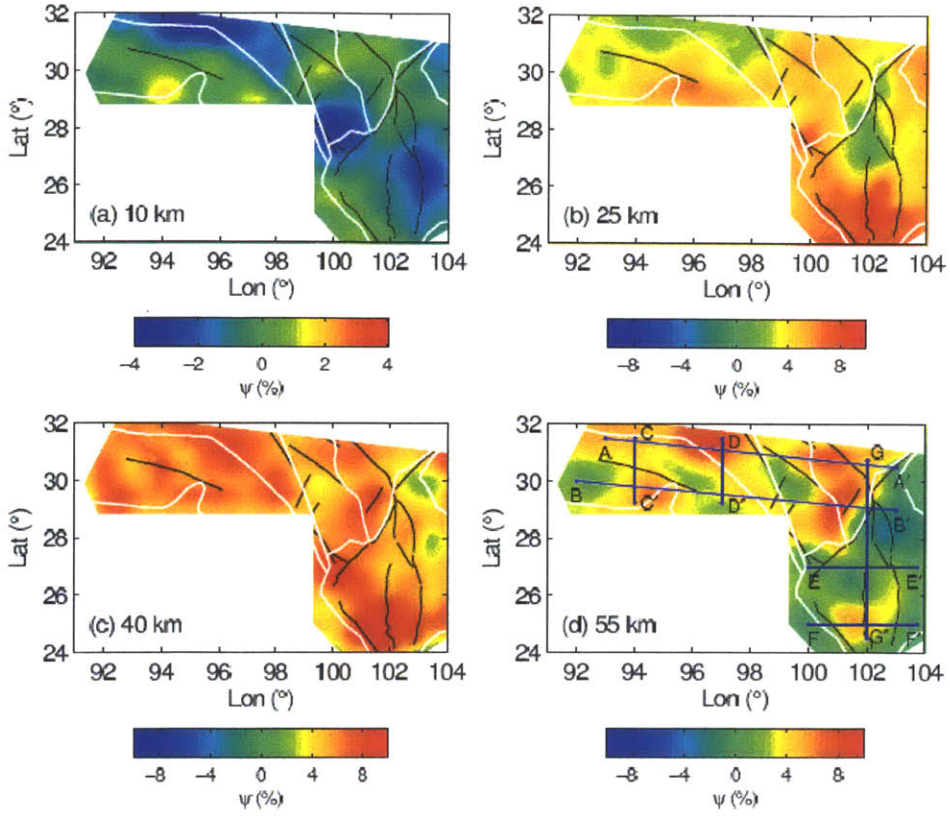

Figure 2B-3. The variations of the radial anisotropy variations at (a) 10 km; (b) 25 km; (c) 40 km; and (d) 55 km. The positions of the vertical profiles in Figures 2B-4 and 2B-5 are shown in (d).

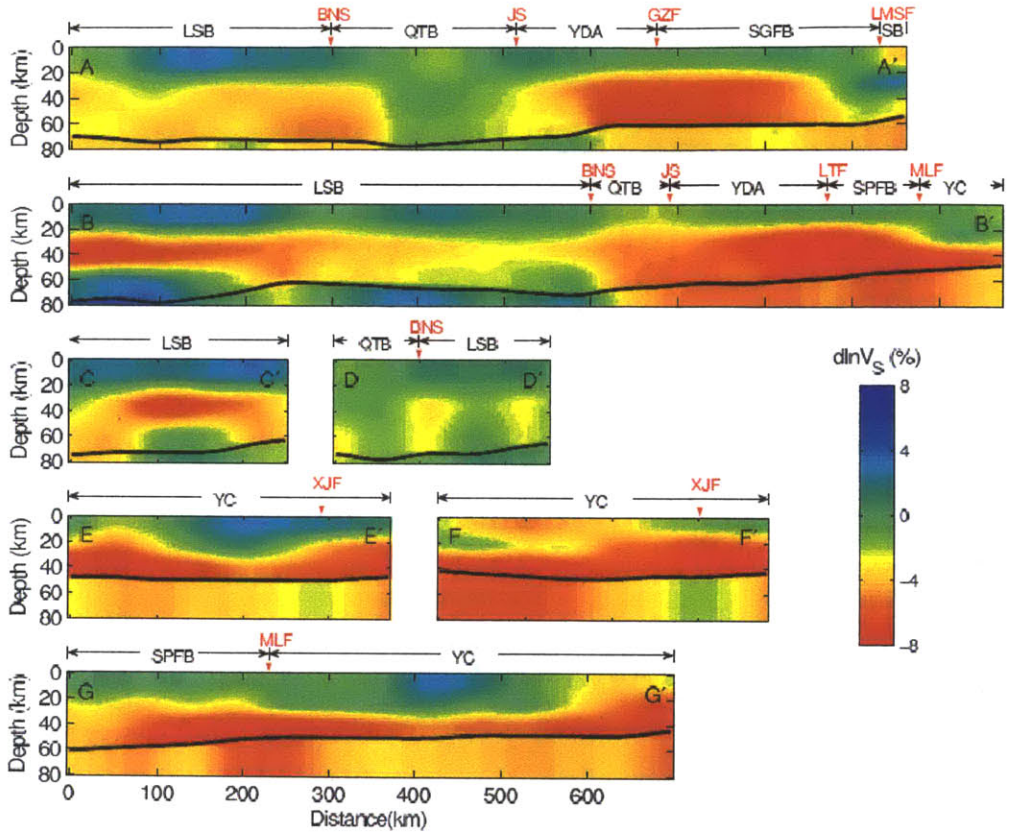

Figure 2B-4. Vertical profiles for the perturbed V_{SV} with respect to the reference model (3.3, 3.6 and 3.8 km/s in the upper, middle, and lower crust, respectively). On top of each profile the locations of major faults and sutures are shown as red ticks (see their abbreviations in Figure 2B-1). The abbreviations for sub-blocks are: Lhasa block (LSB), Qiangtang block (QTB), Yidun Arc (YDA), Songpan-Ganze fold belt (SGFB), Yangtze Craton (YC), and Sichuan Basin (SB).

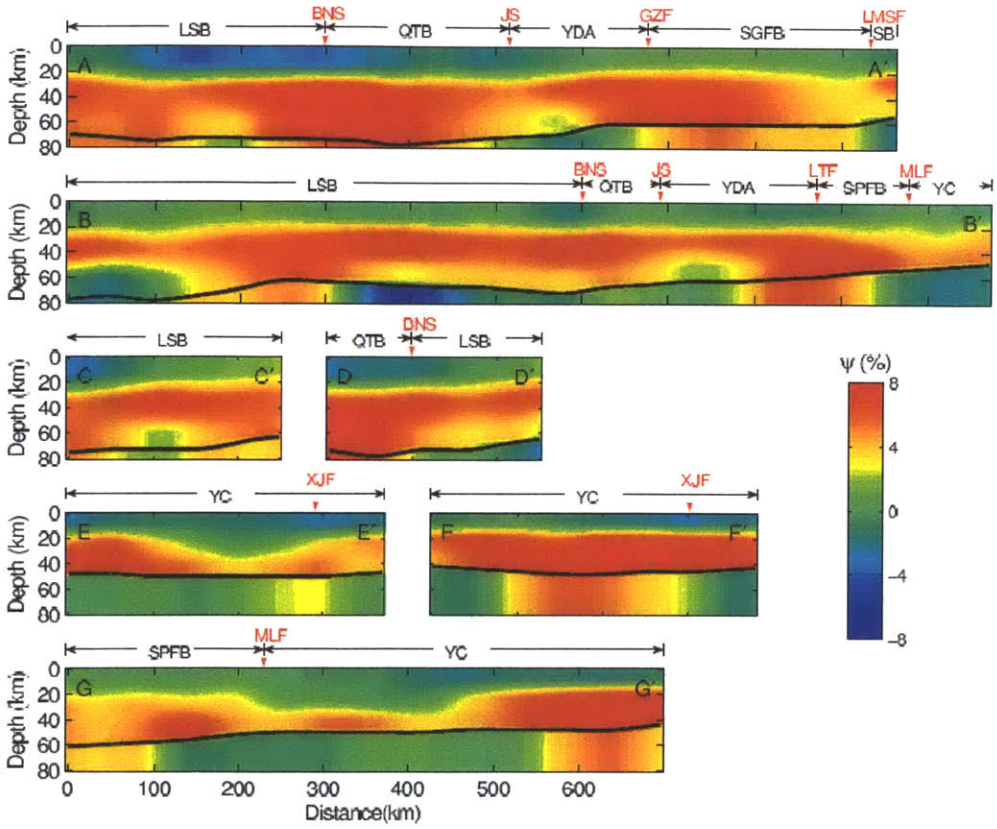

Figure 2B-5. The same as Figure 2B-4, but for radial anisotropy.

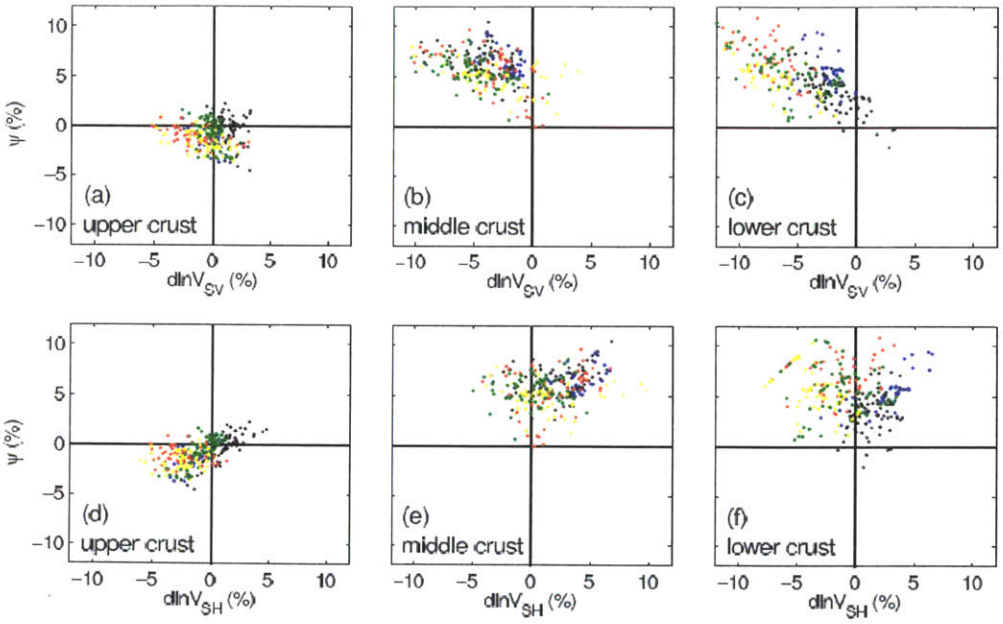

Figure 2B-6. Statics analysis for shear wavespeeds and radial anisotropy: (a) - (c) V_{SV} and radial anisotropy in upper, middle and lower crust, respectively; (d) - (f) the same as (a) - (c), but for V_{SH} and radial anisotropy. The colors represent different geological unites: black for the Lhasa block, blue for the Qiangtang block, cyan for the Yidun Arc and Songpan-Ganze fold belt, red for the western Yangtze Craton (west to the Xiaojiang fault), and yellow for the eastern Yangtze Craton (east to the Xiaojiang fault, including the Sichuan Basin).

Chapter 3

High resolution tomography and radial anisotropy of SE Tibet and its surrounding regions using ambient noise interferometry[2]

Abstract

We perform ambient noise interferometry on records from a dense array in the southeastern margin of Tibetan Plateau. Green's functions and dispersion curves for both Rayleigh and Love waves are extracted at periods from 6s to 40s. Phase velocity maps are inverted from the measured dispersion curves; the resolution can reach to 0.5° at short periods (around 10s) and 1.0° at long periods (around 30s) due to the densely deployed seismic stations. To understand the crustal structures better, we then perform a second-step inversion for depth-dependent shear wave speeds from the obtained phase velocity maps. In general, the shear wave speeds reveal structures consistent with known geology. In the Sichuan Basin, we observe low wavespeed and positive radial anisotropy ($V_{SH}>V_{SV}$) and at shallow depth the magnitudes of their disturbances both reduce from the Longmenshan fault eastward to the Longquan fault, reflecting the gradual decrease of the thickness of the sedimentary layer from the boundary to interior; in contrast, the high velocity anomaly in deep crust reflects a cold and rigid basin root. In the southeastern margin of the Tibetan Plateau, we find widespread low wavespeed zones with positive anisotropy in the middle and lower

[2] In preparation as: Huang, H., Y. Li, Q. Liu, H. Yao, R. D. van der Hilst, High resolution tomography and radial anisotropy of SE Tibet and its surrounding regions using ambient noise interferometry, to be submitted to Physics of the Earth and Planetary Interiors.

crust; the low wavespeed anomalies and their correlation with the anisotropy may reflect sub-horizontal deformation as indicated by the channel flow model. The northern part of the Central Yunnan block shows relative high wave speeds and little or no anisotropy in almost the whole crust, reflecting vertical structures in the inner zone of the Emeishan flood basalt due to material intrusion from the mantle.

3.1 Introduction

The Tibetan Plateau begins its uplift at around 50 Ma when the northernmost part of the Indian plate first collided with the Eurasian plate (Molnar and Tapponnier, 1975). As the Indian plate moves northward, materials are extruded from the collision front to the margins of the plateau; however, not until approximately 8 Ma has the southeastern Tibet started rapid surface uplift (Royden et al., 2008). Furthermore, due to the obstacle of the rigid Sichuan Basin and the rollback of the Pacific and Burman subduction system (Flesch et al., 2001; Royden et al., 2008), the movement direction of the extruded materials turns around 90 degrees at the southeastern margin: from nearly eastward to nearly southward (Wang, 1998; Wang and Burchfiel, 2000; Shen et al., 2005). Therefore, the area between the Eastern Himalaya Syntaxis and the Sichuan Basin is of particular importance to understand the uplift history and relevant dynamic processes of the whole plateau.

Previous studies show complex material properties and tectonic history in this region (Figure 3-1). At the surface, GPS observations reveal several sub-blocks with distinguished motions and deformations (Shen et al., 2005). At depth, a weak middle and lower crust has been suggested by recent discoveries of low velocity zones (LVZs)

(Yao et al., 2008, Zhang et al., 2012), high Poisson's ratio (Hu et al., 2005; Xu et al., 2007), high heat flow (Hu et al., 2000), low electrical resistivity (Bai et al., 2010), and strong radial anisotropy (Huang et al., 2010); however, the strong spatial variation (both horizontal and vertical) of these properties indicate complex structure and tectonic history (Royden et al., 2008). Hence, the deformation in the deep crust, for example flows as indicated by the channel flow model (Royden et al., 1997), is also expected to vary greatly in pattern. Furthermore, based on the comparison of GPS observations and shear wave splitting, Sol et al. (2007) suggest strong lower crust and hence couple lithosphere around the Eastern Himalayan Syntaxis but possible weak lower crust and decoupled lithosphere in southeastern Plateau. Therefore, a 3-D high-resolution model including anisotropy is required to better understand the structures, ongoing deformations and their geological meanings for this complex region.

In this paper, we study the wavespeed of the two shear waves representing vertical and horizontal polarizations respectively using ambient noise data from a densely deployed array in the conjunction region between the southeastern Tibetan Plateau and Yangtze Platform (Figure 3-1). This work is an extension of our previous work (Huang et al., 2010) with higher resolution and more details in structure. The discrepancy between the speeds of the two shear waves is explained as radial anisotropy. The tectonic units in our target region reveal distinct patterns of the wavespeed anomalies and anisotropy, which are consistent with known geology.

3.2 Seismic noise data and interferometry

We use ambient seismic noise data from an array in the region between the Southeastern Tibet Plateau and the Yangtze Platform (Figure 3-1). The densely deployed array, which contains 298 broadband seismometers with inter-station distance of about 15 km, enables high resolution seismic tomography inversion and thus revealing detailed geological structures in this region.

It has been well established in theory and successfully practiced in real data that the surface wave Green's functions between two locations can be extracted from the cross-correlation of the noise records at these two locations (Lobkis and Weaver, 2001; Roux et al., 2005; Yao et al., 2006; Lin et al., 2008):

$$\frac{dC_{AB}(t)}{dt} = -G_{AB}(t) + G_{BA}(-t) \tag{3.1}$$

where $C_{AB}(t)$ is the cross-correlation function and $G_{AB}(t)$ is the Green's function from "source" A to "receiver" B. We do not distinguish the Green's functions in positive and negative time lapse. So the two parts $G_{AB}(t)$ and $G_{BA}(t)$ are summed as the Green's function between locations A and B.

In this study, we use both vertical and transverse seismic records to calculate the Green's functions for Rayleigh and Love waves, respectively. Because one-year-long noise data is sufficient to extract stable Green's functions (Yao et al., 2006; Bensen et al., 2007), we only use seismic records of the year 2007. And we only keep Green's functions with signal-to-noise ratio (SNR) larger than 10 for future analysis. Here the SNR is defined as the average energy ratio in the signal (with velocity 2.5-4 km/s) and noise (with velocity 1.5-2 km/s) windows. Figure 3-2 is the example of Love waves'

Green's functions related to station KCD10 and their corresponding raypaths. The Green's functions reveal a clear travel time move-out against inter-station distance (or travel distances).

Phase velocity dispersion curves (or travel time) at periods from 6 to 40 s are then measured from the Green's functions following Yao et al. (2006). For most of the interested periods we have more than 5,000 measurements (Figure 3-3). At longer periods, the measurement number for Love waves decays faster than that for Rayleigh waves because the SNR for Love waves decrease greater at those longer periods (Lin et al., 2008). The raypath coverage is dense and nearly homogeneous distributed (Figure 3-4) and thus enables us to extract wavespeed models of high-resolution.

3.3 Phase velocity inversion

We first invert for 2-D phase velocity maps from the measured path-averaged phase velocities at periods from 6 to 40 s with interval of 2 s. We aim to minimize the penalty function (Tarantola and Valette, 1982; Montagner, 1986; Griot et al., 1998):

$$\Phi(s) = (t - t_{obs})^T C_d^{-1} (t - t_{obs}) + (s - s_0)^T C_m^{-1} (s - s_0) \qquad (3.2)$$

where t and t_{obs} are the synthetic and measured travel times, and s and s_0 are the inverted and reference slowness models. The synthetic travel time t is the integral of slowness s on the great circle raypath. The data covariance matrix C_d describes the data uncertainties σ_d; and the model covariance matrix C_m is a function of a prior knowledge about the model uncertainty σ_p and the correlation length L (for details see Griot et al, 1998; Yao et al., 2006). So the inversion is controlled by σ_d , σ_p and L: the

data uncertainty σ_d determines the matching preciseness between the calculated and measured travel times; the model uncertainty σ_p and the correlation length L determine the variation magnitude and spatial resolution of the inverted model, respectively. In this study, the data uncertainty σ_d (e.g. the uncertainty of measured dispersion curves) is about 1%-2% following our previous analysis (Yao et al, 2006; Yao et al, 2010). To be conservative, we use 2% for all the measured dispersion curve data. The model uncertainty σ_p is set to be 2% of the reference slowness (the average of all measured slownesses at a specific period). Generally, the correlation length L is function of the wavelength and raypath sparsity (Griot et al., 1998). However, the raypath is always very dense in locations where there are stations (Figure 3-4). So the correlation length L is set to be one reference wavelength.

To examine the resolution of our data set, the inversion scheme described above is applied to synthetic data from checkerboard models (Figure 3-5). The region under study is discretized by a $0.25^{\circ}\times0.25^{\circ}$ grid. At shorter periods (around 10 s), 0.5° anomalies can be recovered in most of the study region; while at longer periods (around 30 s), 1.0° anomalies are recovered. The difference in resolution ability is mainly because the correlation length L increases with period.

The inverted phase velocity maps for both Rayleigh and Love waves are shown in Figure 3-6. Although at a specific period the absolute values of phase velocities are different, similar patterns are observed for Rayleigh and Love waves. At short period (Figure 3-6a, b), the most distinct feature is the strong low velocity anomaly in western Sichuan Basin indicating thick sediments. Also, relatively low anomalies

(compared to the interiors of neighboring blocks) are observed on some major faults, for example the Xianshuihe, Litang, and Xiaojiang faults. This wavespeed reduction near major fault is also observed in the Mojave Shear Zone and along the Garlock Fault in California, US (Shapiro et al., 2005). At longer period (Figure 3-6c, d), as shown in the resolution tests, the resolved anomalies are of larger size and hence show simpler variation patterns. The Basin is dominated by a high velocity body implying cold and (mechanically) strong root. In contrast, the low velocity anomalies in the territory of the Tibetan Plateau reflect active Cenozoic deformation in middle and deep crust (Royden et al., 2008). Also observed is that the magnitude of the anomalies in the Rayleigh wave result is stronger than in the Love wave results. Although the two surface waves have different sensitivity kernel with respect to depth-dependent shear velocity, this discrepancy possibly indicate radial anisotropy in the middle and lower crust.

The posterior errors of phase velocities are about 0.5% in the interior of the array and 1% near the array edges (Figure 3-7). They very small compared with the 5-10% anomaly magnitude, so the observed anomalies are reliable and reflect real structures. Also, the posterior error is smaller than the 2% data uncertainty, which means random noises in data could be suppressed in inversion with sufficient data coverage.

3.4 Shear wave speed inversion

3.4.1 Inversion scheme

We have obtained dispersion curves for every location in our study region. Now

for each location (or grid point), we invert for 1-D depth-dependent shear wave speed using a neighborhood algorithm (NA) (Sambridge, 1999a, 1999b). Juxtaposition of these 1-D models represents the 3-D variation of the wave speeds. Two shear wave speeds, V_{SV} and V_{SH}, with vertical and horizontal polarization directions, respectively, are simultaneously inverted for. We minimize the penalty function:

$$\Phi(m) = \chi^2 + \alpha \cdot \|L\Delta m\|^2 + \beta \cdot \|L\psi\|^2 \qquad (3.3)$$

The three terms in the right hand side are the data mismatch, wave speed regularization, and anisotropy regularization, respectively. The data mismatch function is defined as:

$$\chi^2 = 1/n \cdot \sum_{i=1}^{n} \left[\left(c_i^{pred} - c_i^{obs} \right) / \sigma_i \right]^2 \qquad (3.4)$$

where c_i^{obs} are the phase velocities obtained in the previous section, σ_i are their standard deviations, and c_i^{pred} are the predicted phase velocities from the inverted model m. Here we use posterior errors of c_i^{obs} (Figure 3-7) with minimal values of 1% of c_i^{obs} as the standard deviations. In the two regularization terms, Δm is the model perturbation with respect to the reference model and ψ is the radial anisotropy describing the difference between the two shear wave speeds V_{SV} and V_{SH}:

$$\psi = 2\left(V_{SH} - V_{SV}\right) / \left(V_{SH} + V_{SV}\right) \cdot 100\% \qquad (3.5)$$

The matrix L is the first-derivative operator, imposing the constraint that the wave speed and anisotropy do no change significantly between neighboring layers. The coefficients α and β are to be determined, for instance, using L-curve analysis.

3.4.2 Parameter setting

The wave speed model for each grid contains several crustal layers, one mantle layer,, and a half-space layer below. In our previous studies (Yao et al., 2008; Huang et al., 2010; Yao et al., 2010), the crust is divided equally into three layers, representing upper, middle, and lower crust. We follow this division for the entire study region except the Sichuan Basin. For the Sichuan Basin, the upper crust is further divided equally into two layers to improve data fit (Figure 3-9 and more discussion later). Because the model perturbation Δm is also included in the penalty function (Eq. 3.3), the choice of reference model (or starting model) is not trivial. To be simple but still representative, we use the avarage values from crust 2.0 model (http://mahi.ucsd.edu/Gabi/rem.html). In the crust, the shear wave speeds are 3.4, 3.6 and 3.8 km/s downwards for the three-layer-crust model, and 3.0, 3.4, 3.6, and 3.8 km/s for the four-layer-crust model. For the mantle layer and the half space, the reference wave speeds, 4.45 and 4.55 km/s, respectively, are obtained from the global ak135 model (Kennett et al., 1995).

Surface wave dispersion curves are dependent on shear wave speed (V_S), compressive wave speed (V_P), and density ρ. To reduce the number of independent parameters, we do not invert for V_P and ρ directly but calculate them from V_{SV} instead. In the crust, V_P is calculated using Poisson's ratios obtained from receiver function analysis (Xu et al., 2007); then, density is calculated from V_P using empirical relations proposed by Brocher (2005). In the mantle and half-space, the variation of V_P and ρ are scaled to V_{SV} (Masters et al., 2000; Yao et al., 2008). Since the largest period used

in this paper is 40 s, we do not have much sensitivity in the mantle, especially for the Love wave (Mooney et al., 1998). For this reason, the wave speeds in the mantle layer and half-space are designed to vary simultaneously. Moreover, radial anisotropy is only introduced in the crust, which means the two shear wave speeds in the mantle are manually set to be equal. The Moho depth is also from the receiver function analysis (Xu et al., 2007). Because surface waves are not sensitive to interfaces and a varying Moho in inversion do not change the results much (Huang et al., 2010), we fix the Moho depth here for simplicity.

Now we use an L-curve analysis to help choose the coefficients for the regularization terms. The goal is to obtain a balance between the data mismatch and model and anisotropy roughness. For both α and β we test nine values ranging from 0 to 10, so there are total 81 combinations. Figure 3-8a shows the values of the three terms of different coefficient combinations. These values distribute approximately on a convex surface. More clearly, if the value of one of the coefficients is fixed, nice shaped L-curves are obtained for the two others (Fig 3-8b, c). The tests reveal that the turning points are around 1 for both α and β. The selecting of coefficient values is subjective in some sense. But we find that when the values of α and β are near 1 the inversion results (the shear wave speed models) do not vary much. So in this paper both α and β are set to be 1 for all grid points.

After determination of the regularization coefficients, we now examine how the number of crustal layers influences the data mismatch. We compare the values of χ for two different model assumptions: three-layer crust and four-layer-crust (Figure 3-9).

The normalized residue χ, which is the square root of the first term in penalty function (Eq. 3.3), measures the average fit. In an ideal case the value of χ is only a little smaller than 1; therefore, the predicated data fall within the confidence ranges of the observed data and noise over-fitting is also avoided at the same time (Griot et al., 1998).For the three-layer-crust model the normalized residue χ is less than 1 for all the sub-blocks except for the Sichuan Basin (Figure 3-9a), suggesting that this division is sufficient and appropriate to explain the dispersion curves in these areas. The four-layer-crust model always results in smaller residues and hence better data fit than the three-layer-crust model (Figure 3-9b). In the Sichuan Basin the value of χ is less than 1 for the four-layer-crust model but substantially larger than 1 for the three-layer-crust model. This suggests that the larger χ in the three-layer-crust case is due to the insufficient description of the shallower structures of the basin. Therefore, in the following calculations four-layer-crust model is used for the Sichuan Basin and three-layer-crust model is used for all other regions.

3.4.3 Inversion examples

We conduct NA inversions to calculate the depth-dependent shear wave speeds. Figure 3-10 shows the dispersion curves and inverted V_S models for point locations representative of the Tibetan Plateau, Central Yunnan block, and Sichuan Basin. The phase velocity values for Tibet and the Central Yunnan block (Figure 3-10a, c) do no differ much, but the Tibetan point exhibits larger discrepancy between the two dispersion curves for Rayleigh and Love waves. This larger discrepancy is also

reflected in the inversion results: the point in Tibet shows clear anisotropy in the middle and lower crust, while the point in the Central Yunnan block reveals a nearly isotropic V_S model (Figure 3-10b, d) (NB for an isotropic medium the phase velocities of Love waves are about 10% larger than those of Rayleigh waves). Another important feature is that these two points both show low wavespeed values about 3.5 km/s in the lower crust, much lower than the global reference 3.8 km/s. The point in the Sichuan Basin shows different dispersion curves and inverted model (Figure 3-10c, f). We observe large gradient of the dispersion curves with phase velocities less than 3 km/s at short periods and about 4 km/s at longer periods. The inverted V_S model also exhibits large gradient from surface to deep crust with values about 2.7 km/s at surface and 3.8 km/s in the lower crust. In addition, the radial anisotropy is constrained in the upper and middle crust. The posterior errors of the wave speeds are about 1%, which are very small compared to the speed perturbations and the discrepancies of the two wave speeds, indicating that the wave speed anomalies and radial anisotropy revealed in our inversion results are significant.

3.5 Three-dimensional structure of shear wave speed and radial anisotropy

3.5.1 Shear wave speed structure

We obtain the 3-D variation of the two shear wave speeds by combining the 1-D models at all grid points. Figure 3-11 shows the lateral variations of V_{SV} at four different depths. The first two depths, 5 and 10 km, represent the upper and lower parts of the upper crust. And the two other depths, 25 and 40 km, approximately

represent the middle and lower crust. Since only the Sichuan Basin has four layers in crust, the wave speeds at the first two depths (5 and 10 km) are different only in the Basin and the same in other areas (the visional differences for these regions are due to different colorbars).

In the upper crust, the most significant feature is the very low wave speed in the Sichuan Basin (Fig 3-11a, b) with values as low as about 2.7 km/s (also Figure 3-10c). The Basin is not a uniform unit and can be divided into three parts. The northwestern part, bounded by the Longmenshan and Longquan faults, shows the strongest low anomaly in the whole upper crust. The middle part, east of the Longquan fault and approximately parallel to the fault strike with width of about 0.5^{o}, reveals higher wave speed than its surrounding regions; its wave speed reaches to 3.4 km/s and is higher than most of other sub-blocks at the same depth. The third part, the southeastern corner of the Basin, also shows relatively low wave speed but with smaller magnitude than the northwestern part.

Another feature in the upper crust is that the localized anomalies are well bounded by major faults (Figure 3-11b). For example, the Longmenshan fault, as the boundary of the Tibetan Plateau and Sichuan Basin, separates the high and low wave speed anomalies in these two regions; the Xianshuihe fault separates the two localized high anomalies in the centers of the Longmenshan and Yajiang blocks; and the Litang fault separates the relatively high anomaly in the Yajiang block from the low anomaly in the Shangrila block. Furthermore, a small piece of low anomaly in the South China block is well confined by the Zemehe and Shimian faults, distinguished from the

surrounding high anomalous bodies. In the southern part of the study region, the Xiaojiang fault separates two high anomalies in the Central Yunnan block and South China block.

In the deep crust, V_S exhibits simpler anomaly patterns (Figure 3-11c, d) partially due to the larger resolution length of the longer period surface waves. In the middle crust (Figure 3-11c), the Longmenshan-Muli-Lijiang fault line separates the very low anomaly in Tibet from other parts of our study region, with stronger anomalies south of Xianshuihe fault. Also, the Anninghe-Zemuhe-Xiaojiang fault system separates relatively high anomaly in the Central Yunnan block from low anomaly in the South China block. In the lower crust, we observe widespread low wave speed over the entire region except the Sichuan Basin (Figure 3-11d). In contrast to the middle crust, the low anomaly goes across the Lijian-Muli faults. We also find that the Songpan-Ganze block (to the north of the Xianshuihe fault) has smaller magnitude of low anomaly than the Yajiang and Shangrila blocks (to the south of the Xianshuihe fault).

In general V_{SH} reveals similar anomaly patterns as V_{SV} (Figure 3-12): the Sichuan Basin exhibits low wave speed in the upper crust and high speed in the middle and lower crust; the Songpan-Ganze, Yajiang, and Shangrila blocks in the high Tibetan Plateau show low anomalies in the middle and lower crust; and the Central Yunnan block always shows relatively higher wave speed than surrounding regions throughout the whole crust. Differences between V_{SH} and V_{SV} are mainly in the relative anomaly magnitudes. In the upper crust (Figure 3-12b), the speed contrast between regions on

faults and in block interiors are larger than that in V_{SV} results. In the middle and lower crust (Figure 3-12c, d), the low anomalies in all the blocks expect the Sichuan Basin have much smaller magnitudes.

3.5.2 Radial anisotropy

Radial anisotropy reflects the difference between the two shear wave speeds. According to the definition in Eq. (3.5), it is positive if V_{SH} is larger than V_{SV}, and it is negative is if V_{SH} is smaller than V_{SV}. Their values and posterior errors are shown in Figures 3-13 and 3-14.

At 5 km depth, a patch of negative anisotropy is found in the northeastern corner of Sichuan Basin. Considering that the posterior error there is large (about 3%) and the data coverage is relatively poor near the edges of the study region, we are not confident that it reflects realistic structure. At 10 km depth, strong positive anisotropy (about 4%) dominates the Sichuan Basin; the largest magnitude is located in the northwest part and southeastern corner, which is in good correspondence with the patterns of wavespeed anomalies (Figure 3-11b). Localized positive anisotropies with magnitudes of about 1-2% are found in the Longmenshan, Yajiang, and Shangrila blocks. Negative anisotropies are observed near some major faults, with magnitudes between 1-4%. The posterior errors are general about 1-2% and can reach to 3% for some locations (Figure 3-14b). So we are not sure about these weak anisotropies and need to do further analysis to confirm these observations.

In the middle and lower crust (Figure 3-13b and c), the anisotropy has

distinguished patters from these in the upper crust. The anisotropy gradually decreases in magnitude in the Sichuan Basin. We observe anisotropy of about 3% in the middle crust and little or none anisotropy in the lower crust. In contrast, positive anisotropies, with largest magnitude of about 10%, are widespread in the Longmenshan, Yajiang, Shangrila, and South China blocks. In good consistent with wavespeed anomaly, the Longmenshan block (to the north of the Xianshuihe fault) always reveals smaller anisotropy than the Yajiang and Shangrila blocks (to the south of the Xianshuihe fault). The Central Yunnan block shows little or no anisotropy. These patterns are also well revealed in the inversion examples (Figure 3-10).

3.6 Discussion

The sub-blocks in our study region reveal distinct patterns of wave speed anomaly and radial anisotropy. To better understand their structures and geological meanings, we study the vertical profiles of the wavespeed anomaly and anisotropy (Figures 3-15, 3-16) and their correlations (Figure 3-17).

3.6.1 Sichuan Basin

The Sichuan Basin, located in the westernmost part of the South China block, is topographically distinct from its surrounding areas (Figure 3-1). Although the whole Sichuan Basin is sitting on an old basement of Archean-Paleoproterozoic age (Zheng et al., 2006), it can be approximately divided into three sub-units: the Northwestern

Depression, the Central Uplift and the Southeastern Depression (Ma et al., 2007). All the three sub-units have strike parallel to that of the Longmenshan fault. The Northwestern Depression sub-unit, bounded by the Longmenshan fault to the west and Longquan fault to the east, is a foreland basin which has a two-phase flexural-loading history in Late Triassic and Cretaceous-Paleogene, respectively (Yong et al., 2003; Dong et al., 2006). The thickness of the sediment layers in this foreland basin can reach about 10 km near the Longmenshan fault and decreases gradually into the center of the Basin and reaches about 2 km near the Longquan fault (Dong et al., 2006; Richardson et al., 2008). The Central Uplift sub-units, bounded to the west by the Longquan fault and to the east by the eastern Sichuan fold-thrust belt (outside our study region), has outcropping strata mainly of Upper Jurassic age. The thickness of the sediments is about 2 km (Meng et al., 2005), much thinner than the Northwestern Depression unit. However, in the southern end of the Central Uplift sub-unit, the outcropping strata are of Cretaceous age, indicating relatively thicker sediments than other portion of this sub-unit (Richardson et al., 2008).

The seismic array used in this paper mainly covers the southern parts of the Northwestern Depression and the Central Uplift sub-units. The patterns of the two shear wavespeeds are well consistent with the geology described above. For the two wavespeeds (V_{SV} and V_{SH}), the first-order features are the strong low anomaly in the upper crust and high anomaly in the middle and lower crust, reflecting thick sedimentary layers at surface and stable and rigid and stable basin root at depth (Figures 3-11 and 3-12). Careful examination reveals that the in the upper crust the

two wavespeeds have finer structures and well correspond to the sedimentary thickness at the surface. The values of the two wavespeeds are lowest near the Longmenshan fault, and they increase gradually to the interior of the Basin reaching their maximum values near the Longquan fault, and then they decrease again to the southeast (Figures 3-11a, b and 3-12a).

For the radial anisotropy, the first-order features are the positive anisotropy (about 4%) in the upper crust and little or no anisotropy in the middle and lower crust (Figure 3-13). The wavespeed and anisotropy contrasts between the Basin and its neighboring sub-blocks are significant (profiles AA' and EE' in Figures 3-15 and 16). The anisotropy also reveals finer structures at the surface: its largest magnitude appears in the northwest and southeast of the Basin (Figure 3-13b). The radial anisotropy in sediments can be caused by the intrinsic anisotropy in sedimentary rocks (e.g. shale, siltstone etc.) and the layering of fine layers as effective vertical transverse isotropic (VTI) media. In the Central Uplift sub-unit, some sedimentary layers are either thinner or missed (Meng et al., 2005); therefore, the effective radial anisotropy is smaller than in the northwestern foreland basin.

3.6.2 Tibetan Plateau

In our study region, the southeastern Tibetan Plateau is composed of two main geological units: the Songpan-Ganze unit to the north and the Yidun unit to the south separated by the Litang fault. The Yidun unit (coincides with the Shangrila block in our study area: Figure 3-1) comprises of mainly felsic and volcanic rocks (Wang et al.,

2000), revealing lower wave speed in the upper crust (Figures 3-11b, 3-12b, and profile DD' in Figure 3-15). The Songpan-Ganze bold belt, which in our study region contains the Longmenshan and Yajiang blocks, mainly comprises folded flysch (Wang et al., 2000), revealing normal wave speeds around 3.4 km/s in the upper crust.

In the middle and lower crust, the low wave speed anomaly dominates the Yajiang, Shangrila and Longmenshan blocks, although amplitude of the low anomaly is smaller in the Longmenshan block; the magnitude of anisotropy has a similar distribution (profile AA', BB' and DD' in Figures 3-15 and 3-16). When comparing the shear speeds with anisotropy, only V_{SV} shows clear negatively correlation (Figure 3-17). As proposed in our previous study (Huang et al., 2010), we suggest that the low wave speed and negative correlation between V_{SV} and anisotropy are due to the combined effects of reduced temperature and sub-horizontal flow. Low wave speed anomalies in the deep crust indicate increased temperature and hence reduced rock mechanics. If horizontal flow occurs, mineral fabrics would align sub-horizontally and exhibit anisotropy with horizontal fast axis (Weiss et al., 1999; Nishizawa and Yoshitno, 2001). Consequently, V_{SV} would decrease further while the V_{SH} would increase, thus producing positive radial anisotropy. In all, the V_{SV} is reduced but the change of V_{SH} is unclear due to the conflicting effect of the high temperature and horizontal flow. Therefore, a negative correlation is observed between the reduced V_{SV} and positive anisotropy, while no clear correlation is observed between V_{SH} and anisotropy.

3.6.3 Central Yunnan block

The Central Yunnan block is distinct from its neighboring blocks. It shows higher wave speeds and less or no anisotropy in the entire crust; whereas the neighboring Tibetan blocks and South China block contain strong slow anomaly and positive radial anisotropy in the middle-lower crust (Figures 3-11 to 3-13 for horizontal profiles and Figures 3-15 to 3-16 for vertical profiles CC' and EE'). In the context of larger region (Yao et al., 2008; Huang et al., 2010), we find that this high wave speed and little anisotropy body is confined to the northern part of the Central Yunnan block; in the southern part low wave speed and positive radial anisotropy are observed near the Red River and Xiaojiang faults.

The high wavespeed anomaly in the Central Yunnan block may be related to materials intruded from the mantle. In their gravity study, Lou and Wang (2005) observe a high density anomaly nearly the northern Central Yunnan block, and they argue that the anomaly represents materials intruded upwards from mantle. In addition, this anomalous body coincides geographically with the inner core of the Emeishan large igneous province. He et al. (2003) argue that the Emeishan flood basalt is caused by a mantle plume just beneath the core zone around the Permian-Triassic boundary. We speculate that the high wavespeed and low radial anisotropy body inferred from our data may reflect the residue of cooled materials intruded from the mantle. Since the intruded materials mainly have sub-vertical structures, the remnants of which may combine with effects of horizontal flow to produce a small net radial anisotropy. Therefore, even if radial anisotropy is small in the Central Yunnan block, it does not

necessarily mean there is no horizontal structures or flows in its middle and lower crust. In fact, azimuthal anisotropy with North-South fast direction is observed in the deep crust of the region (Yao et al., 2010; Huang et al., 2013), which is consistent with sub-horizontal deformation.

3.6.4 South China block

In the upper crust of the South China block a prominent low anomaly is observed between the Zemuhe and Shimian faults, corresponding to the Xichang sedimentary basin (Figures 3-11b and 3-12b, and profile EE' in Figure 3-15). Seismic refraction experiments also reveal relatively low wave speed in its upper crust (Wang et al., 2008). However, unlike the Sichuan Basin little or no anisotropy is found in this region (Figure 3-13b and profile EE' in Figure 3-16). This can be due to several reasons. First, the sediments here are not very thick and fine layering is perhaps not as significant as that in the Sichuan Basin. Second, the strike-slip faults in this region are well developed and dense seismicity is observed (Wang et al., 2008), so these sub-vertical structures would increase V_{SV}. Third, the radial anisotropy has larger uncertainty than the two shear wave speeds, and it is possible that our tomography fails to detect the anisotropy in this small unit.

The middle and lower crust of the South China block contains zones of low wavespeed and positive radial anisotropy anomaly. The anomalies may be connected with the strong low anomalies in Tibet through a narrow channel to the north of the Central Yunnan block. Low wave speed and positive anisotropy are also found to the

south of our study region (Huang et al., 2010). Therefore, these observations suggest that sub-horizontal motions in the middle and lower crust are not truncated, but we do not rule out the possibility that the magnitude of such flow varies over sub-blocks.

3.7 Summary and conclusions

We conduct ambient noise interferometry to extract Green's functions for both Rayleigh and Love waves; and then a two-step inversion for 3-D shear wave speeds is performed. Tomography results are obtained for the southeastern margin of the Tibetan Plateau and its surrounding regions. The wave speeds anomaly and anisotropy patterns are consistent with known geology at surface. Major findings are listed below.

In the Sichuan Basin, we observe low wave speed and positive anisotropy in the upper crust; and both the magnitude of wave speed anomaly and anisotropy decrease eastward from the boundary Longmenshan fault into the Longquan fault. These patterns reflect the gradually decreasing of sediment thickness from the boundary to interior due to lithospheric flexure of this ancient foreland basin. In contrast, the old basement of the Basin exhibits fast wavespeed and little or no anisotropy.

For the Tibetan Plateau and South China block, very low wavespeed anomalies and positive anisotropy are found in the middle and lower crust. We suggest that they are caused by the combined effects of increased temperature and sub-horizontal flow in the deep part of the crust.

The northern part of the Central Yunnan block reveals relatively high wave speed

anomaly and little or no anisotropy in an area corresponding to the inner core of the Emeishan flood basalt, which have intruded from the mantle at the onset of the Mesozoic. The lack of a clear radial anisotropy may reflect the combined effects of the sub-vertically intruded structures and sub-horizontal motions after the intrusion.

References

Bai, D., M. J. Unsworth, M. A. Meju, X. Ma, J. Teng, X. Kong, Y. Sun, J. Sun, L. Wang, C. Jiang, C. Zhao, P. Xiao, and M. Liu, (2010), Crustal deformation of the eastern Tibetan plateau revealed by magnetotelluric imaging, Nature Geosci., 3, 358-362, doi:10.1038/ngeo830.

Bensen, G.D., M.H. Ritzwoller, M.P. Barmin, A.L. Levshin, F. Lin, M.P. Moschetti, N.M. Shapiro, and Y. Yang, (2007), Processing seismic ambient noise data to obtain reliable broad-band surface wave dispersion measurements, Geophys. J. Int., 169, 1239-1260.

Brocher, T.M., (2005), Empirical relations between elastic wavespeeds and density in the Earth's crust, Bull. Seism. Soc. Am., 95(6), 2081-2092.

Dong, J., Wei G., Chen Z., Li B., Zeng Q., and Yang G., (2006), Longmen Shan fold-thrust belt and its relation to the western Sichuan Basin in central China: new insights from hydrocarbon exploration, The American Association of Petroleum Geologists Bulletin, 90(9), 1425-1447.

Flesch. L.M., A.J. Haines, and W.E. Holt, (2001), Dynamics of the India-Eurasia collision zone, J. Geophys. Res., 106(B8), 16435-16460.

Griot, D.A., J.P. Montagner, and P. Tapponnier, (1998), Phase velocity structure from Rayleigh and Love waves in Tibet and its neighboring regions, J. Geophys. Res., 113(B9), 21215-21232.

He B., Xu Y., Chung S., Xiao L., and Wang Y., (2003), Sedimentary evidence for a rapid, kilometer-scale crustal doming prior to the eruption of the Emeishan flood basalts, Earth and Planetary Science Letters, 213, 391-405, doi:10.1016/S0012-821X(03)00323-6.

Hu, S., He, L. & Wang, J., 2000. Heat flow in the continental area of China: a new data set, Earth planet. Sci. Lett., 179, 407–419.

Hu, J.F., Su Y.J., Zhu X..G., Chen Y., (2005), S-wave velocity and Poisson's ratio structure of crust in Yunnan and its implication, Science in China Ser. D Earth Sciences, 48(2), 210-218.

Huang, H., H. Yao, and R.D. van der Hilst (2010), Radial anisotropy in the crust of SE Tibet and SW China from ambient noise interferometry, Geophysical Research Letters, 37(21), DOI: 10.1029/2010GL044981.

Huang, H., Li Y., Liu Q., De Hoop M.V., van de Hilst R., (2013), Eikonal tomography and azimuthal anisotropy for the SE Tibet and SW China, in preparation.

Kennett,B.L.N., E.R. Engdahl, R. Buland, (1995), Constraints on the velocity structure in the earth from travel times, Geophys. J. Int., 122, 108–124.

Lin, F., M.P. Moschetti, and M.H. Ritzwoller, (2008), Surface wave tomography of the western United States from ambient seismic noise: Rayleigh and Love wave phase velocity maps, Geophys. J. Int., 173, 281-298.

Lou, H., and Wang C., (2005), Wavelet analysis and interpretation of gravity data in Sichuan-Yunnan region, China, ACTA Seismologica Sinica, 18(5), 552-561.

Lobkis, O.I., R.L. Weaver, (2001), On the emergence of the Green's function in the correlations of a diffuse field, J. Acoust. Soc. Am, 110(6), 3011-3017.

Ma, Y., Guo X., Guo T., Huang R., Cai X., and Li G., 2007, The Puguang gas field: new giant discovery in the mature Sichuan Basin, southwest China. The American Association of Petroleum Geologists Bulletin, 91(5), 627-643.

Masters, G., G. Laske, H. Bolton, and A. Dziewonski, (2000), The relative behavior of shear velocity, bulk sound speed, and compressional velocity in the mantle: implications for chemical and thermal structure, Geophys. Monogr. Ser., 117, 63–87.

Meng, Q., E. Wang, and Hu J., (2005), Mesozoic sedimentary evolution of the northwest Sichuan basin: Implication for continued clockwise rotation of the South China block, Geological Society of America Bulletin, 117 (3/4), 396-410. doi: 10.1130/B25407.

Molnar P., and P. Tapponnier, (1975), Cenozoic tectonics of Asia: Effects of a continental collision: Features of recent continental tectonics in Asia can be interpreted as results of the India-Eurasia collision, Science, 189, 419-426.

Montagner, J.P., (1986), Regional three-dimensional structures using long period surface waves, Ann. Geophys., 4, 283-294.

Mooney, W.D., G. Laske, and G. Masters, (1998), CRUST5.1: a global crustal model at $5^{\circ} \times 5^{\circ}$, J. geophys. Res., 103, 727–747.

Nishizawa, O., T. Yoshitno, (2001), Seismic velocity anisotropy in mica-rich rocks: an inclusion model, Geophys. J. Int. 145, 19-32.

Richardson, N.J., Densmore A.L., Seward D., Fowler A., Wipf M., Ellis M.A., Rong L., and Zhang Y., (2008), Extraordinary denudation in the Sichuan Basin: insight from low-temperature thermochronology adjacent to the eastern margin of the Tibetan Plateau, J. Geophys. Res., 113, B04409, doi: 10.1029/2006JB004739.

Roux, R., K.G. Sabra, W.A. Kuperman, A. Roux, (2005), Ambient noise cross correlation in free space: Theoretical approach, J. Acoust. Soc. Am, 117(1), 79-84. Sambridge M., (1999a), Geophysical inversion with a neighborhood algorithm –I. Searching a parameter space, Geophys. J. Int., 138, 479-494.

Royden, L.H., B.C. Burchfiel, R.W. King, E. Wang, Z. Chen, F. Shen, and Y. Liu, (1997), Surface deformation and lower crustal flow in eastern Tibet, Science, 276, 788-790.

Royden, L.H., B.C. Burchfiel, R.D. van der Hilst, (2008), The geological evolution of the Tibetan plateau, Science, 321, 1054-1058.

Shapiro, N.M., M. Campillo, L. Stehly, M.H. Ritzwoller, (2005), High-resolution surface-wave tomography from ambient seismic noise, Science, 307, 1615-1618.

Sambridge M., (1999b). Geophysical inversion with a neighborhood algorithm –II. Appraising the ensemble, Geophys. J. Int., 138, 727-746.

Shen, Z., J. Lv, M. Wang, R. Burgmann, (2005), Contemporary crustal deformation around the southeast borderland of the Tibetan Plateau, Journal of Geophysical research, 110, B11409.

Sol, S., A. Meltzer, R. Burgmann, R.D. van der Hilst, R. King, Z. Chen, P.O. Koons, E. Lev, Y.P. Liu, P.K. Zeitler, X. Zhang, J. Zhang and B. Zurek, (2007), Geodynamics of the southeastern Tibetan Plateau from seismic anisotropy and geodesy, Geology, 35, 563-566.

Tarantola, A., and B. Valette, (1982), Generalized nonlinear inverse problem solved using the least squares criterion, Rev. Geophys. Space Phys., 20(2), 219-232.Wang, E., (1998), Late Cenozoic Xianshuihe-Xiaojian, Red River and Dali fault systems of southwestern Sichuan and central Yunnan, China, Spec. Pap, Geol. Soc, Am., 327.

Wang, E., B.C. Burchfiel, (2000), Late Cenozoic to Holocene deformation in southwestern Sichuan and adjacent Yunnan, China, and its role in formation of the southeastern part of the Tibetan Plateau, Geol. Soc. Am. Bull., 112, 413-423.

Wang, F., Duan Y., Yang Z., Zhang C., Zhao J., Zhang J., Zhang X., Liu Q., Zhu A., Xu X. and Liu B., (2008), Velocity structure and active fault of Yanyuan-Mabian seismic zone – The result of high-resolution seismic refraction experiment, Sci China Ser D-Earth Sci, 51(9), 1284-1296.

Weiss, T., S. Siegesmund, W. Rabbel, T. Bohlen, M.Pohl, Pure Appl. (1999), Seismic Velocities and Anisotropy of the Lower Continental Crust: A Review, Geophys. 156, 97-122.

Xu, L., S. Rondenay, and R. D. van der Hilst, (2007), Structure of the crust beneath the southeastern Tibetan Plateau from teleseismic receiver functions, *Phys. Earth Planet. Int.*, 165, 176-193, doi: 10.1016/j.pepi.2007.09.002.

Yao, H., R. D. van der Hilst, and M. V. De Hoop, (2006), Surface-wave array tomography in SE Tibet from ambient seismic noise and two-station analysis – I. Phase velocity maps, *Geophys. J. Int.*, 166, 732-744, doi: 10.1111/j.1365-246X.2006.03028.x.

Yao, H., C. Beghein, and R.D. Van der Hilst, (2008), Surface wave array tomography in SE Tibet from ambient seismic noise and two-station analysis – II. Crustal- and upper-mantle structure, Geoohys. J. Int., 173, 205-219.

Yao, H., R. D. van der Hilst, and J.P. Montagner, (2010), Heterogeneity and anisotropy of the lithosphere of SE Tibet from surface wave array tomography, Journal of Geophysical Research, 115, B12307, doi:10.1029/2009JB007142.

Yang, T., Hou Z., Wang Y., Zhang H., and Wang Z., (2012), Late Paleozoic to Early Mesozoic tectonic evolution of northeast Tibet: Evidence from the Triassic composite western Jinsha-Garzê-Litang suture, Tectonics, 31, TC4004, doi: 10.1029/2011TC003044.

Yong, L., Allen P.A., Densmore A.L., and Qiang X., (2003), Evolution of the Longmen Shan foreland basin (Western Sichuan, China) during the Late Triassic Indosinian orogeny, Basin Research, 15, 117-138.

Zhang, H., Roecker S., Thurber C.H., and Wang W. (2012). Seismic Imaging of Microblocks and Weak Zones in the Crust Beneath the Southeastern Margin of the Tibetan Plateau, Earth Sciences, Dr. Imran Ahmad Dar (Ed.), ISBN: 978-953-307-861-8, 159-202.

Zhang, P., Shen Z., and Wang M., et al., (2004), Continuous deformation of the Tibetan Plateau from global positioning system data, Geology, 32(9), 809-812.

Zheng. J., Griffin W., O'Reilly S., Zhang M., Pearson N., and Pan Y., (2006), Widespread Archean basement beneath the Yangtze craton, Geology, 34(6), 417-420.

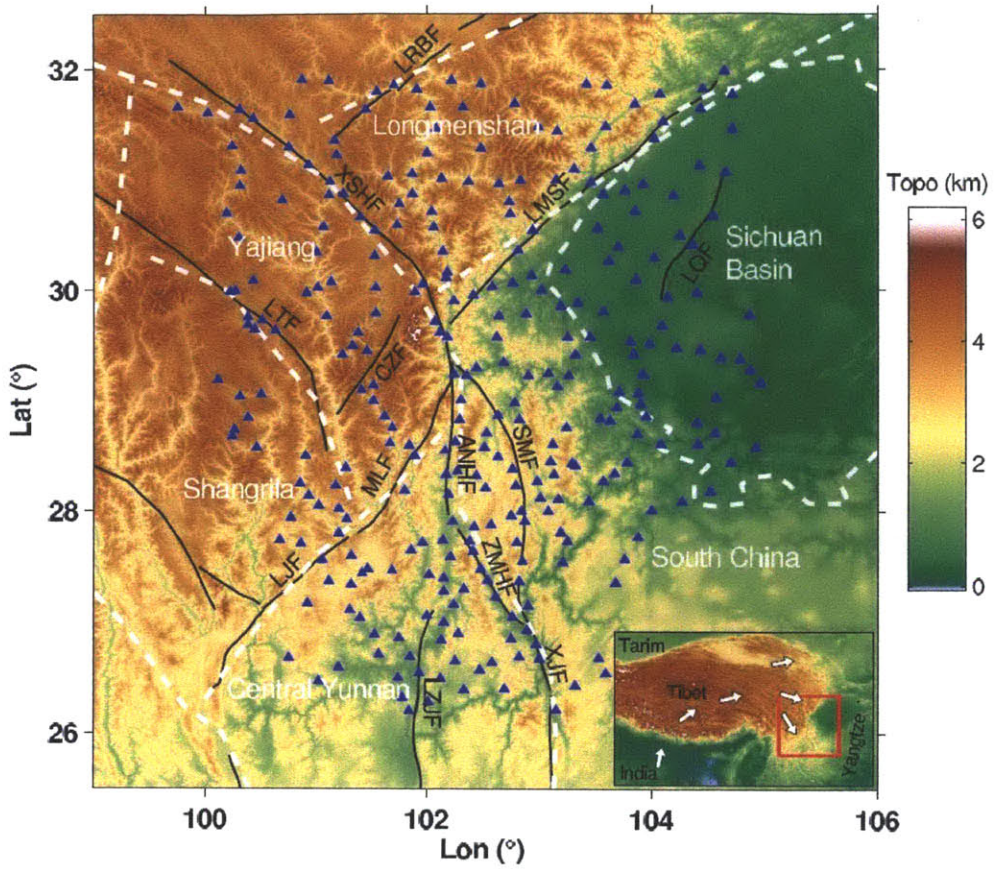

Figure 3-1. Topography, geological units and seismic stations used in this study. The topography is represented by the background color. The locations of seismic stations are depicted as blue triangles. Our study region can be approximately divided into six geological units according to GPS observations (Shen et al., 2005): the Longmenshan block, Yajiang block, Shangrila block, Central-Yunnan block, Sichuan Basin, and the South Chian block; and their boundaries are depicted as white dash curves. Major faults are depicted as thin black lines and the abbreviations are: Longriba fault (LRBF), Xianshuihe fault (XSHF), Longmenshan fault (LMSF), Longquan fault (LQF), Litang fault (LTF), Chenzhi fault (CZF), Lijian fault (LJF), Muli fault (MLF), Anninghe fault (ANHF), Zemuhe fault (ZMHF), Xiaojiang fault (XJF), Shimian fault (SMF), and Luzhijiang fault (LZJF) (after Wang et al., 1998; Wang and Burchfiel, 2000; Shen et al., 2005). The inset shows the location of our study region, depicted by the red box, in the background of the whole Tibetan Plateau and its surrounding areas. The white arrows show the approximate surface motion relative to the Yangtze Craton from GPS observations (Zhang et al., 2004; Shen et al., 2005).

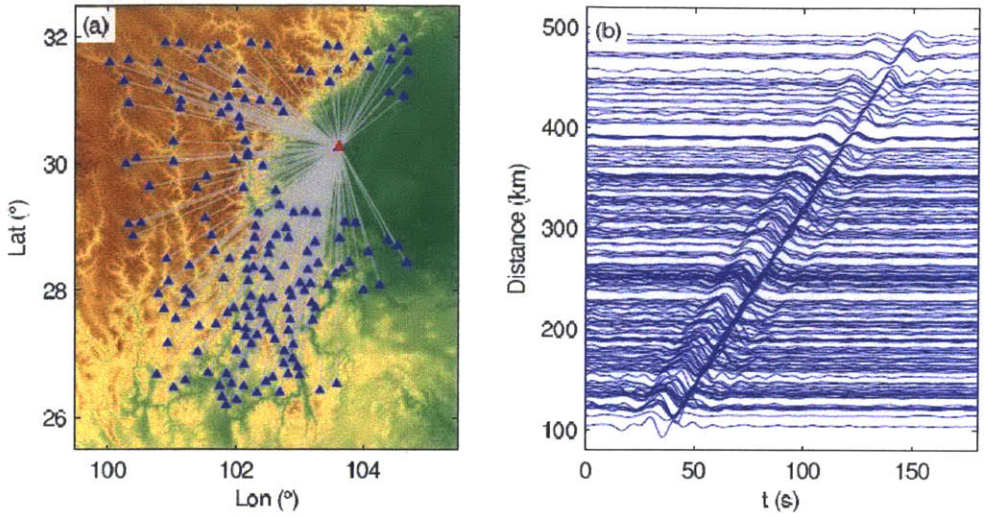

Figure 3-2. (a) All the transverse-component raypaths related to virtual source station KCD10 which is shown as the red triangle. Other stations are shown as blue triangles. (b) The cross-correlation functions (CFs) corresponding to the raypaths in (a). The CFs are filtered between period band 8 – 30 s, and only those with signal-to-noise ratio larger than 10 are plotted.

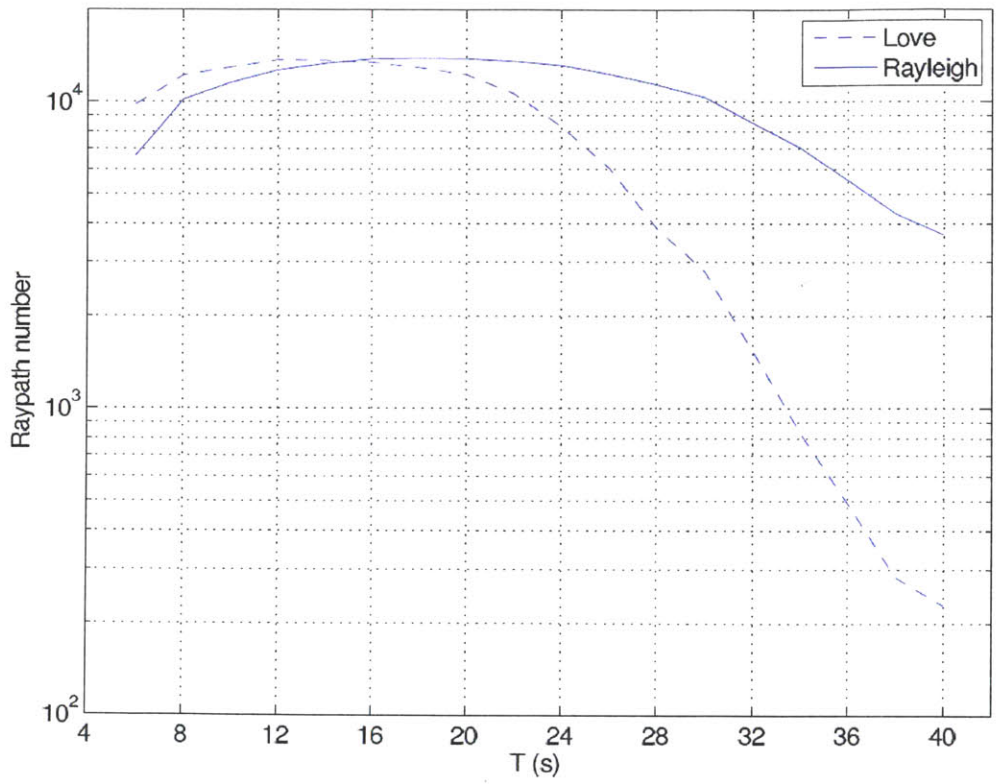

Figure 3-3. Numbers of measured raypath-averaged phase velocities for both Rayleigh and Love waves.

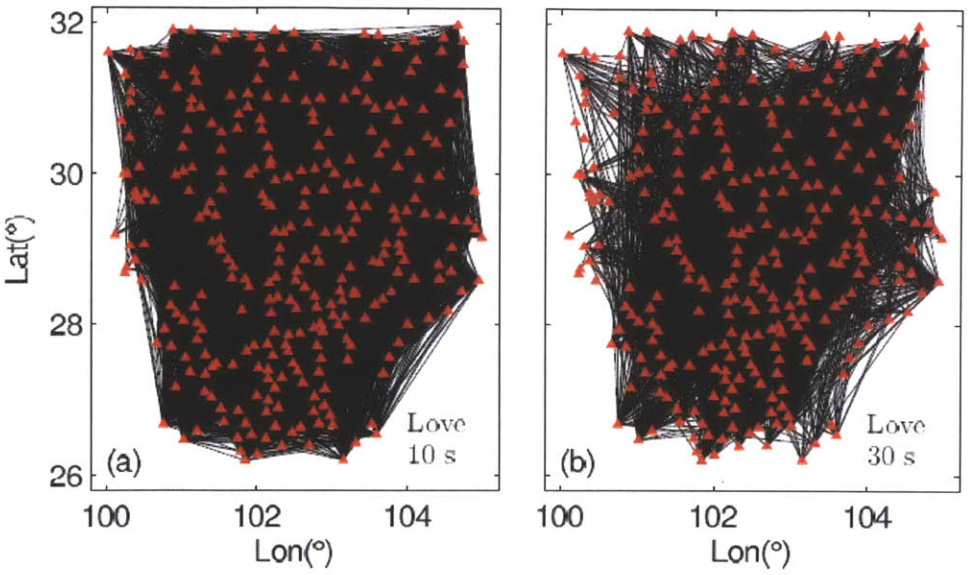

Figure 3-4. Raypath coverage at (a) 10 s and (b) 30 s of Love waves.

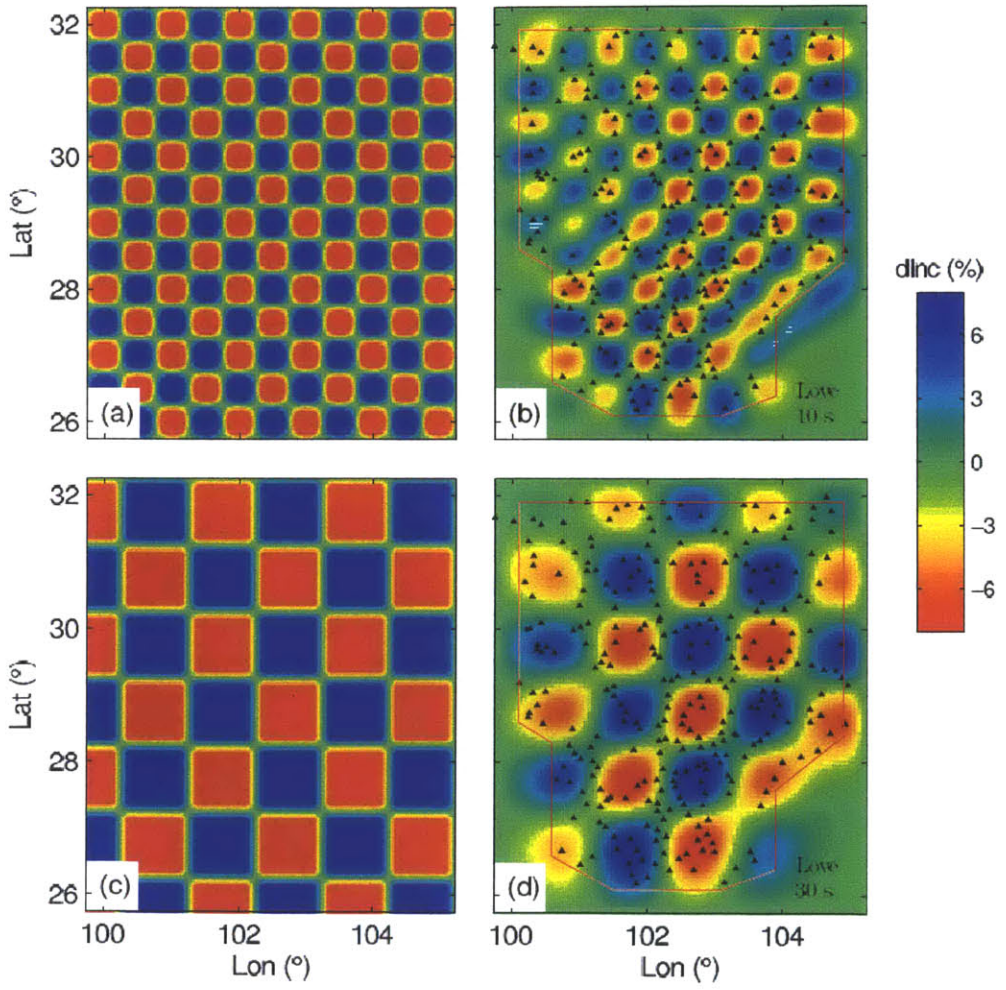

Figure 3-5. Checkerboard test results: (a) $0.5^{\circ}\times0.5^{\circ}$ checkerboard model; (b) recovered model using 10 s Love wave data; (c) $1.0^{\circ}\times1.0^{\circ}$ checkerboard model; and (d) recovered model using 30 s Love wave data. The red curves in (b) and (d) depict the region with good anomaly recovery.

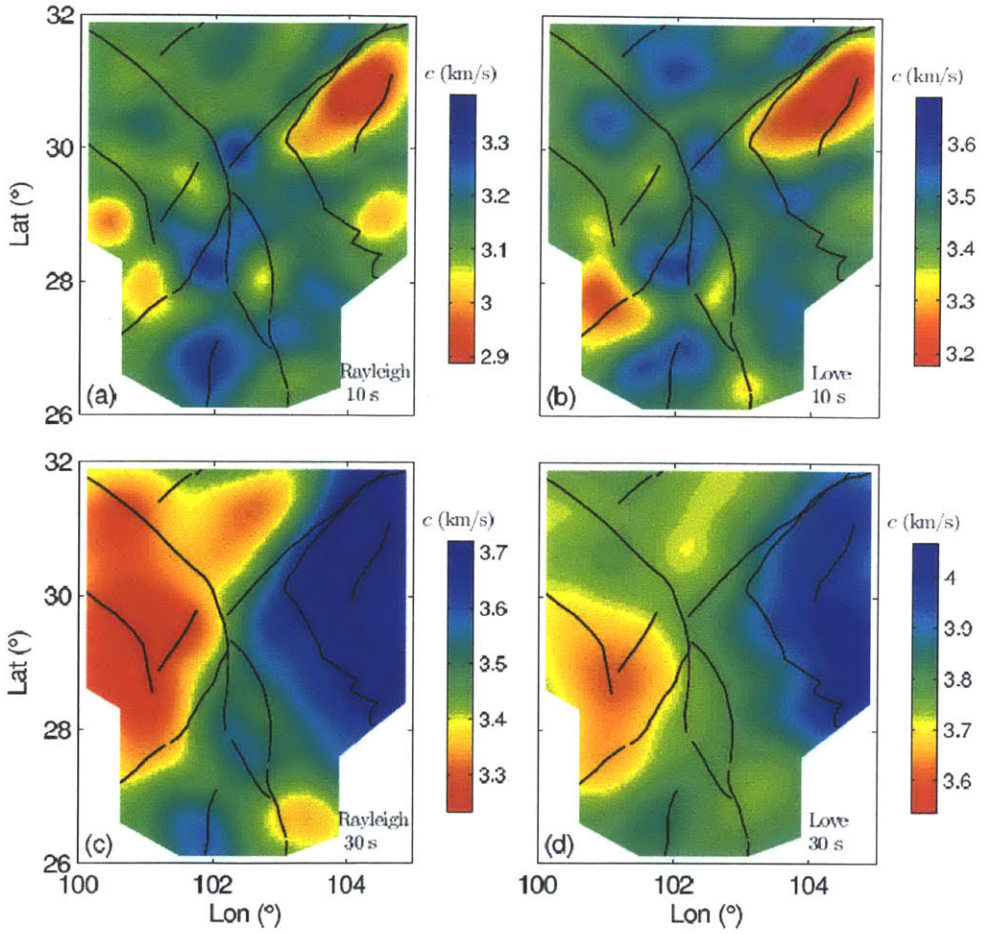

Figure 3-6. Phase velocity variations for both Rayleigh and Love waves at 10 and 30 s.

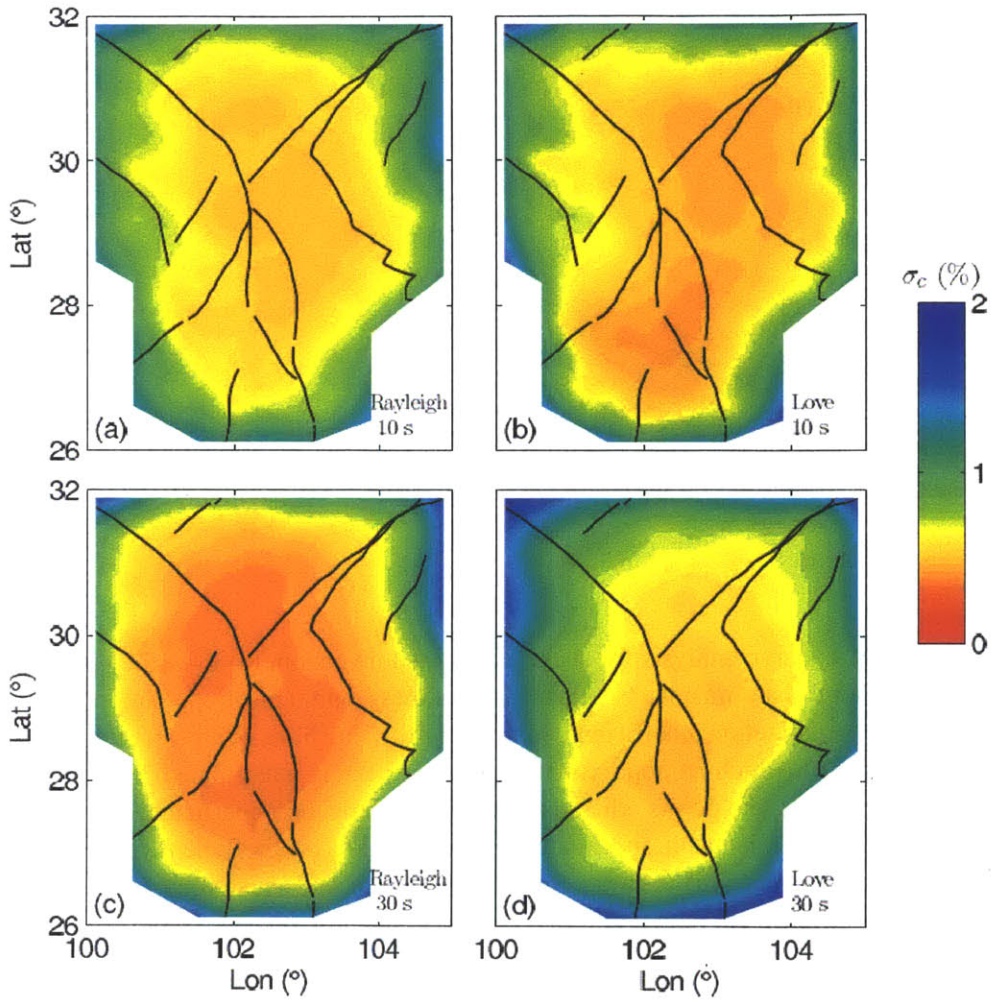

Figure 3-7. Posterior errors (in percentage) of the inverted phase velocity models.

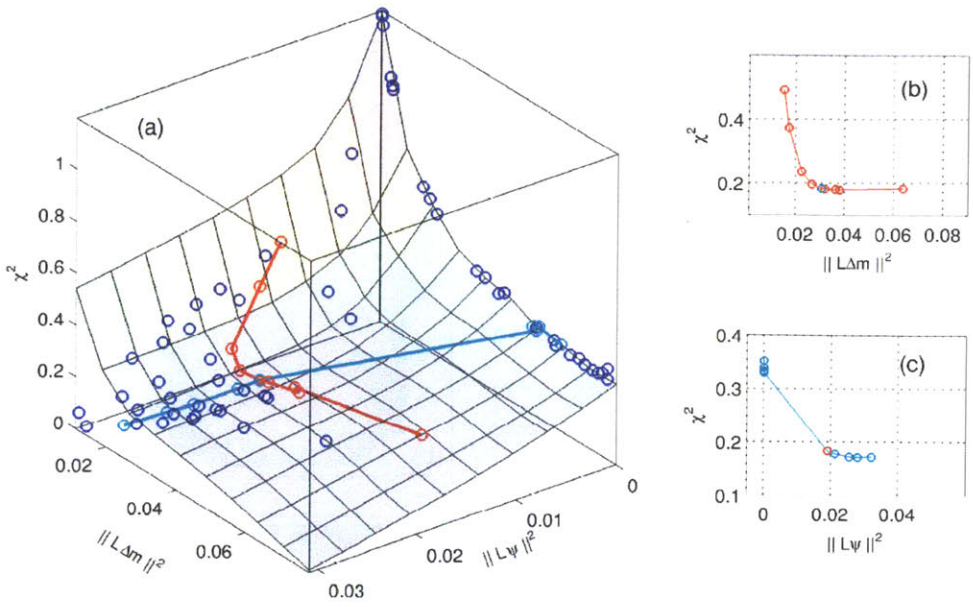

Figure 3-8. L-curve analysis for shear wavespeed inversion. (a) L-surface presenting the values of data mismatch, model smoothness and anisotropy smoothness of different regularization coefficient combinations. The blue circle are the inverted results based on which an approximate convex surface is interpolated. The two color curves connecting the points when one of two regularization coefficients is fixed. (b) L-curve for data mismatch and model regularization. The coefficient for anisotropy regularization is one. (c) L-curve for data mismatch and anisotropy regularization. Here the coefficient for model regularization is one. The cyan and red circle in (b) and (c) represent the cross-point of the two curves (both coefficients are one).

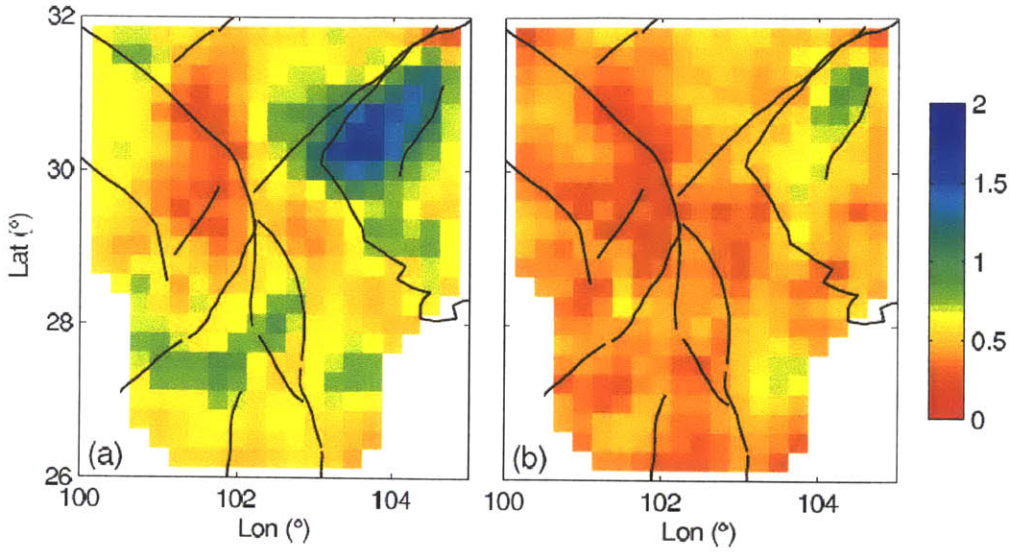

Figure 3-9. Data mismatch for (a) three-layer-crust and (b) four-layer-crust model inversion. When the value of data mismatch is less than one, the predicted data from the inverted model in general fall within the confident range of the measured data, which means the inverted model can explain the measured data.

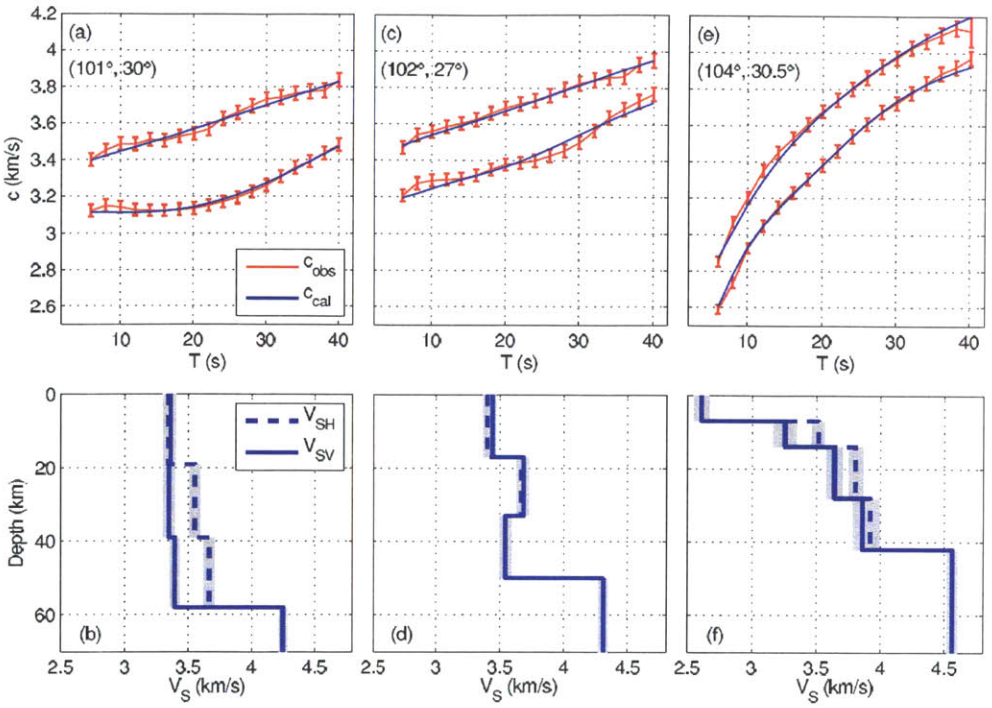

Figure 3-10. Inversion results for the two shear wavespeeds at three locations: (a), (b) Tibetan Plateau (101°, 30°); (c), (d) Central Yunnan block (102°, 27°); and (e), (f) Sichuan Basin (104°, 30.5°). In the top three figures, the measured dispersion curves are shown in red with standard errors; and the predicted dispersion curves from the inverted models are shown in blue. The upper curves are the dispersion curves for Love waves; and the lower curves are for Rayleigh wave. In the bottom three figures, the inverted wavespeed models are plotted in blue and their standard deviations are in grey.

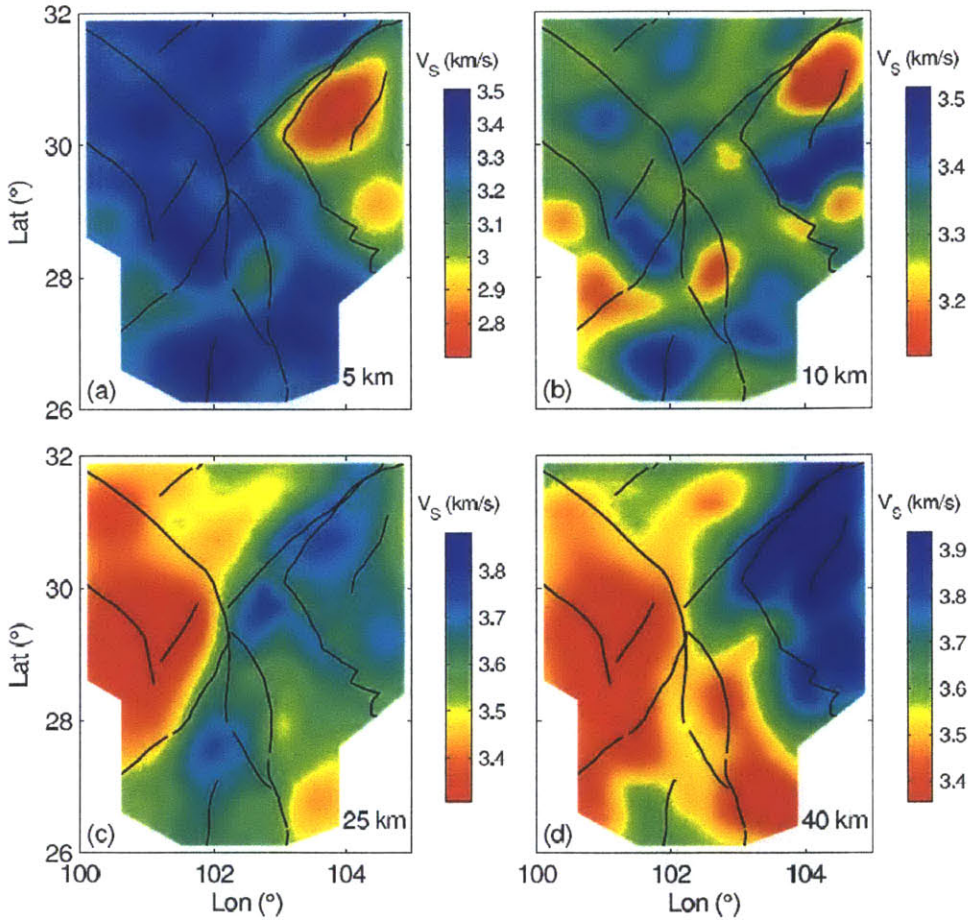

Figure 3-11. The variations of vertically polarized shear wavespeed (V_{SV}) at (a) 5 km; (b) 10 km; (c) 25 km; and (d) 40 km.

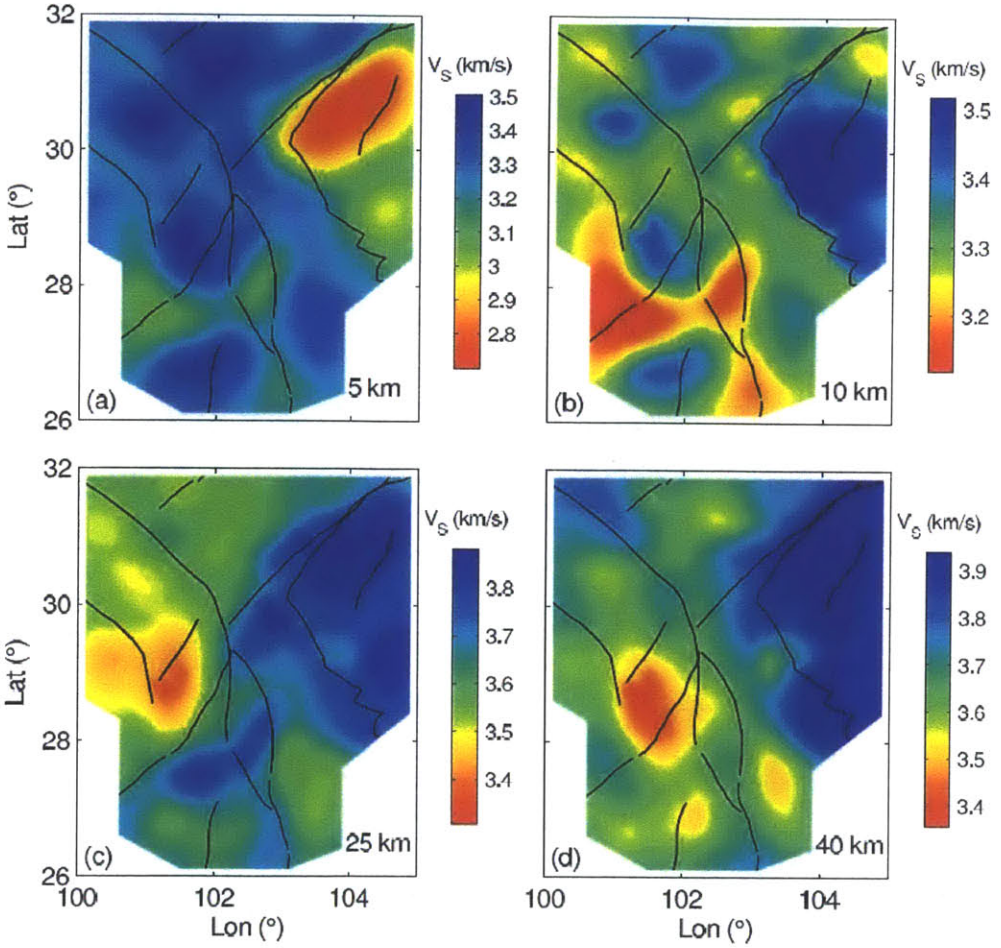

Figure 3-12. The same as Figure 3-11, but for horizontally polarized shear wavespeed (V_{SH}).

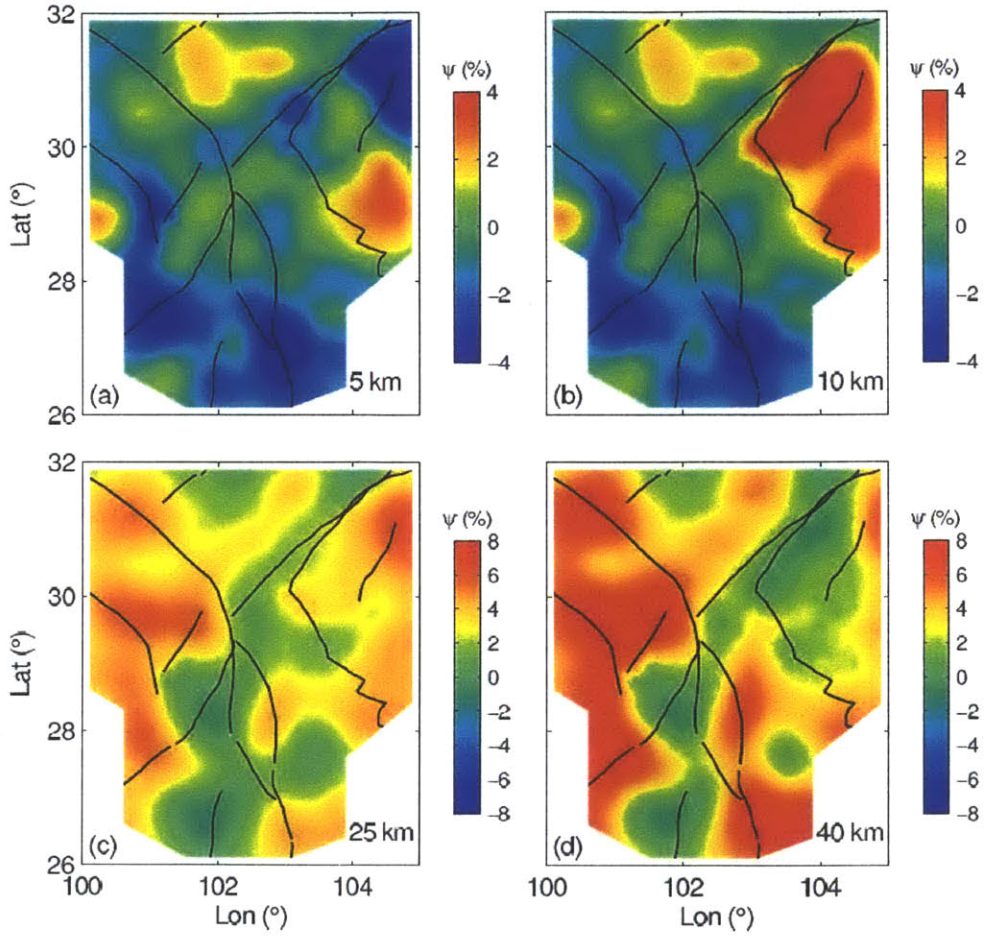

Figure 3-13. The variations of radial anisotropy at (a) 5 km; (b) 10 km; (c) 25 km; and (d) 40 km.

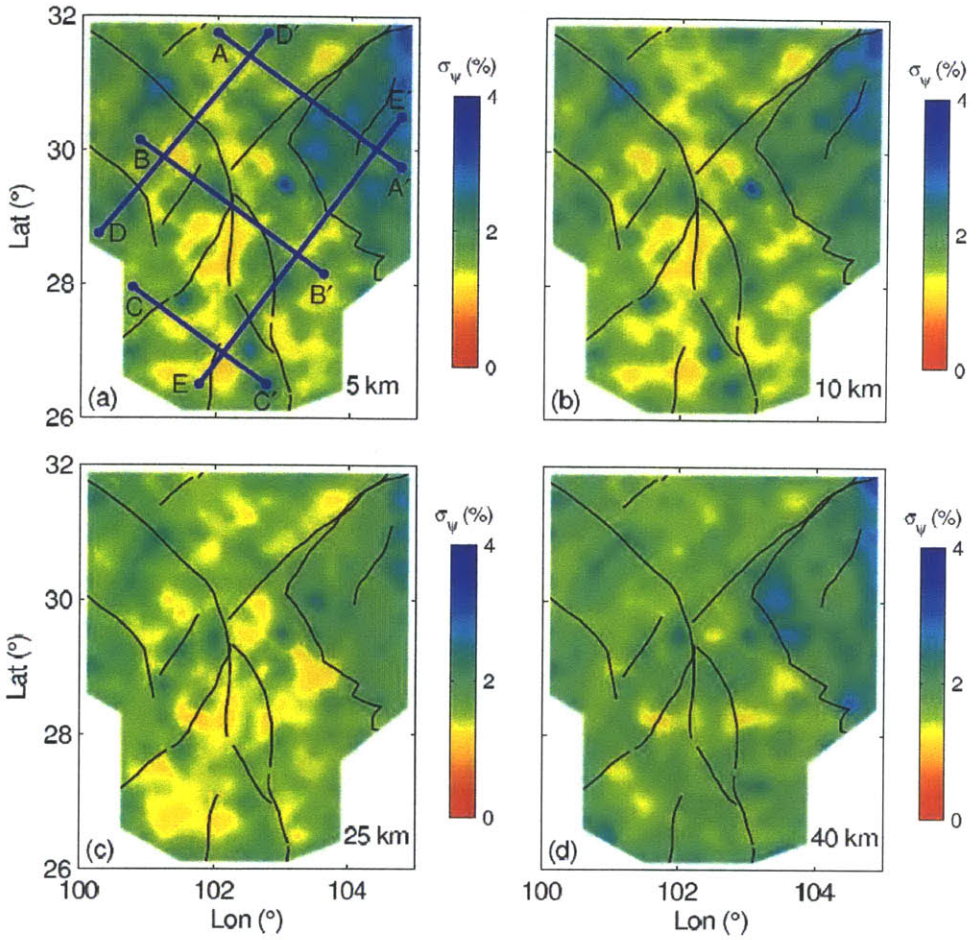

Figure 3-14. The standard deviations for the radial anisotropy in Figure 3-13. The positions of the four vertical profiles in Figures 3-15 and 3-16 are also depicted in (a).

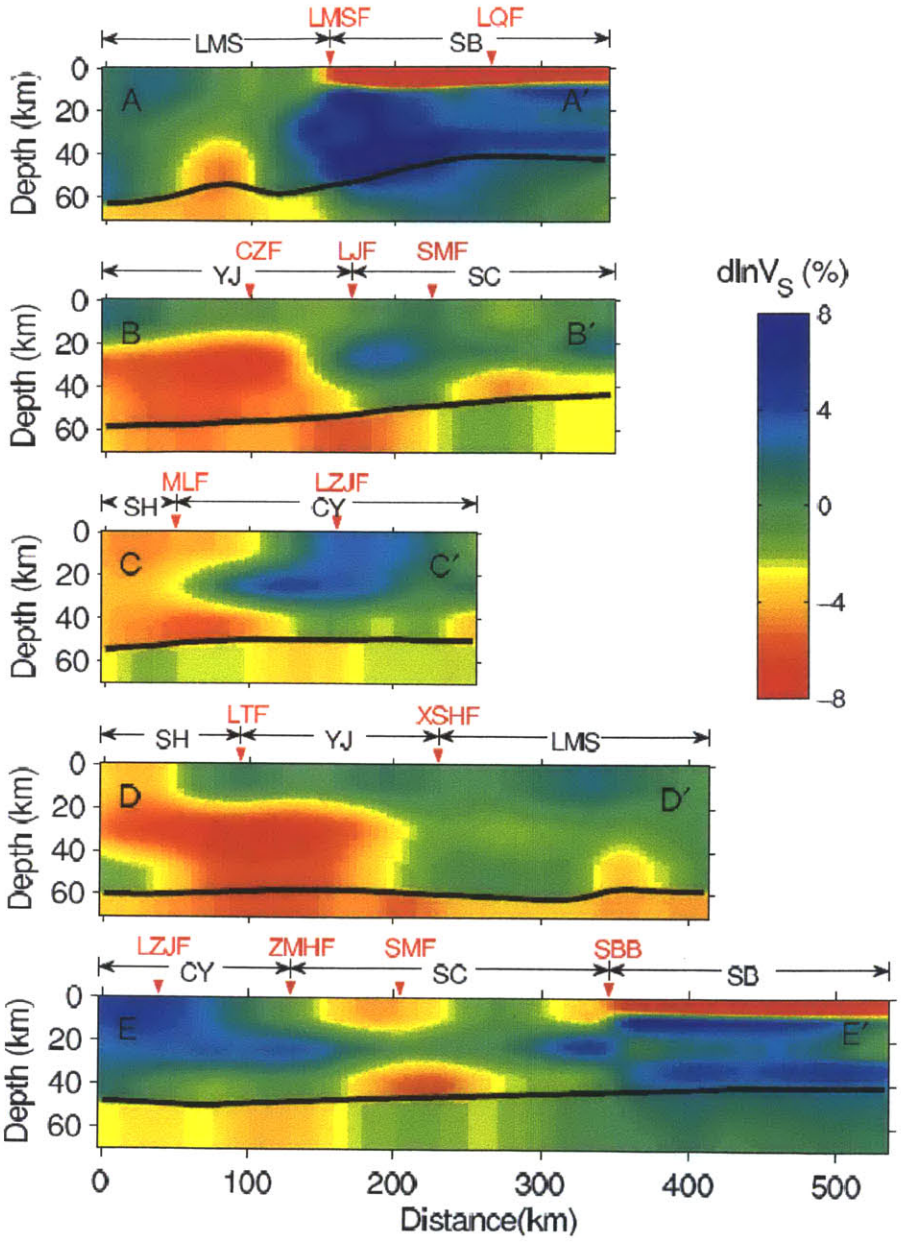

Figure 3-15. Vertical profiles for the perturbed V_{SV} (Figure 3-11) with respect to the average values of each layer. On top of each profile the locations of major faults are shown as red ticks; see the abbreviations in Figure 3-1 and SBB is the Sichuan Basin boundary. The abbreviation for sub-blocks are: Longmenshan block (LMS), Yajiang block (YJ), Shangrila block (SH), Central-Yunnan block (CY), Sichuan Basin (SB), and South China block (SC).

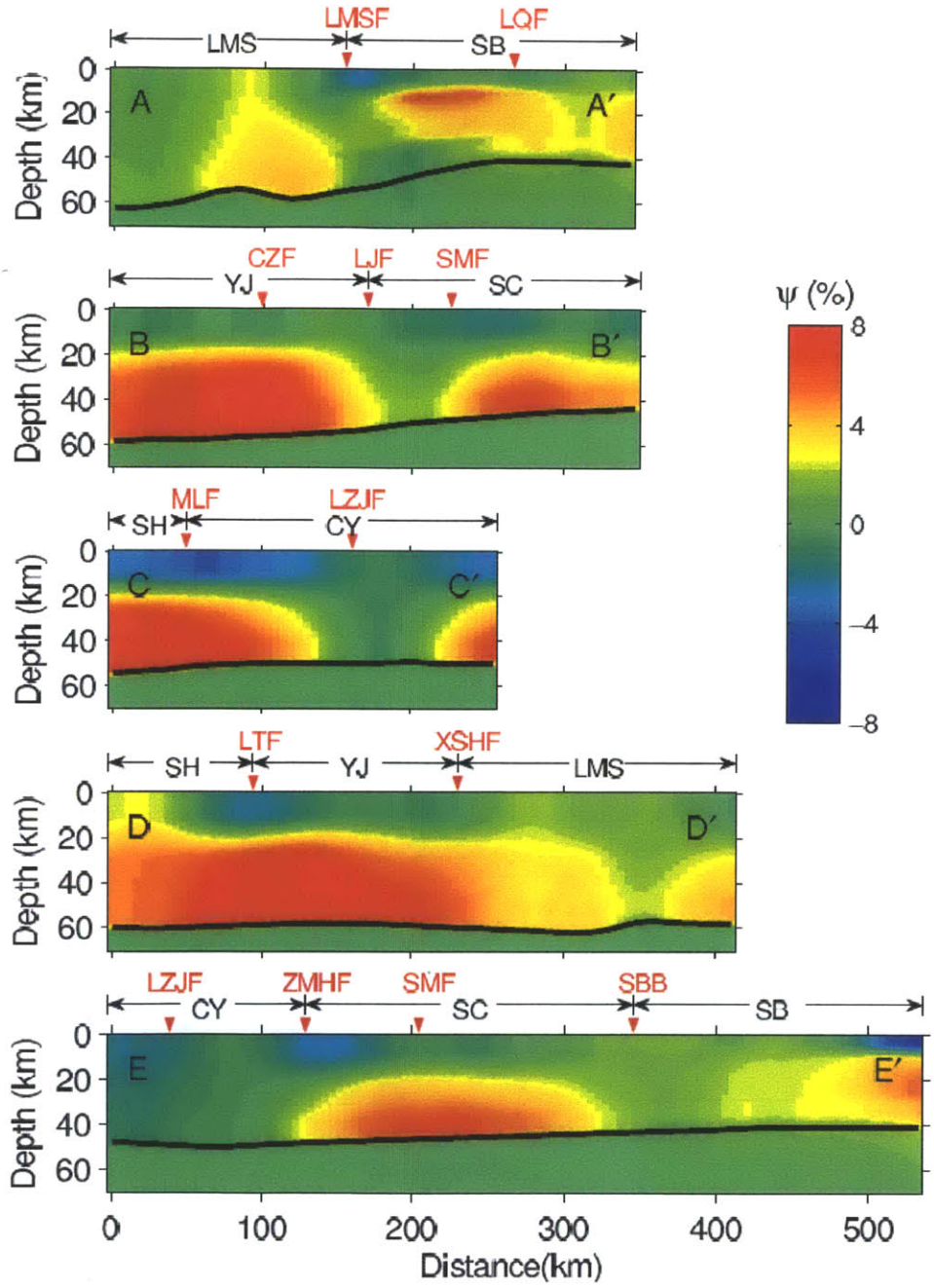

Figure 3-16. The same as Figure 3-15, but for radial anisotropy.

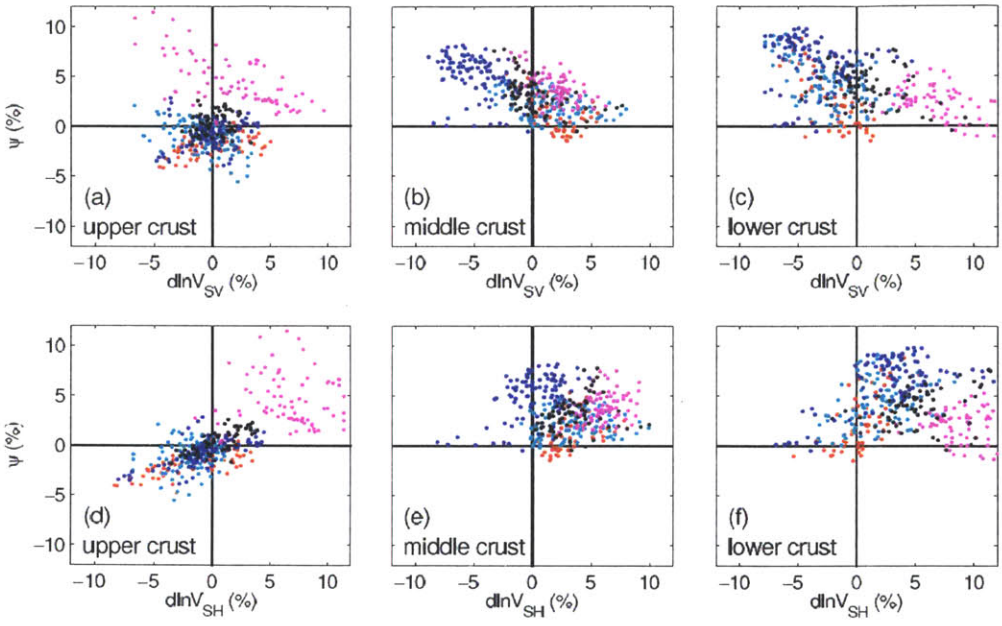

Figure 3-17. Statics analysis for shear wavespeed and radial anisotropy: (a) - (c) V_{SV} and radial anisotropy in upper, middle and lower crust, respectively; (d) - (f) the same as (a) - (c), but for V_{SH} and radial anisotropy. The colors represent different geological unites: black for the Longmenshan block, blue for the Yajiang and Shangrila blocks, red for the Central-Yunnan block, cyan for the South China block, and magenta for the Sichuan Basin.

Chapter 4

Eikonal tomography and azimuthal anisotropy for the SE Tibet and SW China[3]

Abstract

We perform Eikonal tomography on Rayleigh waves extracted from cross-correlations of ambient seismic noise for the SE Tibet Plateau and adjacent areas. Based on Eikonal equation, the local wavespeed and propagation direction are obtained from the gradient of the traveltime. The calculation is on the perturbed traveltimes to improve accuracy in interpolation. The isotropic phase velocity and azimuthal anisotropy are studied for arbitrary location in our study region. Then a two-step inversion is performed to reveal the structures of the isotropic V_{SV} and azimuthal anisotropy. Low velocity zones are widespread in the middle and lower crust of the high Plateau and South China block, in sharp contrast to the high wave speed in deep crust of the Sichuan Basin. Also, strong azimuthal anisotropy (> 2%) is observed in most of the study region throughout the crust except the Sichuan Basin. Although the fast directions at different depths of the crust are all consistent with a clockwise rotation around the Eastern Himalayan Syntaxis, their angular differences are large and thus may imply different deformation patterns at surface and in depth. Furthermore, the synthetic shear-wave splitting from the crustal model in this study exhibits different directions from the observed SKS splitting, which may indicate different deformation directions and patterns in the crust and mantle. Therefore, our

[3] In preparation as: Huang, H., Y. Li, Q. Liu, H. Yao, M. V. de Hoop, and R. D. van der Hilst, Eikonal tomography and azimuthal anisotropy for the SE Tibet and SW China, to be submitted to *Geophys. J. Int.*

results may imply decoupled crust and mantle in the southeastern marginal areas of the Tibetan Plateau.

4.1 Introduction

The rise mechanism and coupling between the crust and mantle for the southeastern Tibetan Plateau have been debated over the last decades. A lot of modeling works, which propose distinct physical settings in lithosphere, have been conducted to account for topography variation, surface velocity field, stress field, and so on. In general, there are three schools of modeling. The first school proposes that the lithosphere of Tibet is composed of rigid blocks, which move coherently throughout the lithospheric depths (Molnar and Tapponnier, 1975; Tapponnier et al., 1982). The second school regards the lithosphere as a thin viscous sheet with continuous deformation (England and McKenzie, 1982; England and Houseman, 1986; Flesch et al., 2001). The viscous lithosphere obeys a Newtonian or a power law rheology, and the vertical gradients of the horizontal velocity are negligible. Thus, both the rheology and modeled deformation represent the average values over the entire study depth. The third school, the channel flow model, is proposed to explain the either sharp or smooth topography gradient (Royden et al., 1997; Clark and Royden, 2000). It argues that the extruded materials from the central collision zone of the Indian and Eurasian plates flow and accumulate in a weak layer in the deep crust and thus cause the uprising the southeastern Tibet. The crust and mantle are decoupled due to the existence of the weak layer in the crust. Besides the above three schools

with simple concepts, more complicated numerical modeling has been conducted (Copley and McKenzie, 2007; Copley, 2008). However, the rheology is poorly constrained; even if the deformation at the surface is well modeled its patterns in deep lithosphere can differ greatly with different settings of rheology.

Progress has been made to address different aspects of the lithosphere of southeastern Tibet and surrounding areas; controversy and dispute, however, still exist. On the one hand, the widespread low velocity zones (Yao et al., 2008; Zhang et al., 2012), high Poisson's ratio (Xu et al., 2007), low electrical resistivity (Bai et al., 2010), and strong radial anisotropy (Huang et al., 2010) all suggest weak middle or lower crust and thus decoupled lithosphere. In addition, azimuthal anisotropy reveals different fast directions in the crust and mantle, indicating possible difference in deformation (Yao et al., 2010). On the other hand, based on the direction consistence between the maximum strain-rate (either extension or shear) from GPS observations and SKS splitting, Sol et al. (2007) and Wang et al. (2008) argue for a coupled lithosphere and thus a relative strong crust for the SE Tibet. However, this directional consistence does not necessarily mean coherent lithospheric deformations. The velocity field from GPS only reflects the current deformation patterns at surface. In contrast, SKS splitting measures the integral effect of the anisotropy in the entire mantle and crust and reflect of both current and previous deformation. Hence, the deformation in the lithosphere may vary at different depths even there is some consistence between surface strain-rate and SKS splitting. Therefore, high-resolution wavespeed and anisotropy studies would be helpful to better understand the structures

and deformations for the southeastern Tibetan Plateau.

In this paper, we use the Eikonal equation (Wielandt, 1993; Shearer, 1999) to extract local wavespeed and its variation with propagation direction, i.e. azimuthal anisotropy for Rayleigh waves. The Green's functions for Rayleigh waves are obtained from the cross-correlation functions of the ambient seismic noise. Unlike the traditional tomography which is based on an integral equation, the Eikonal tomography uses a differential equation to connect the local wavespeed and traveltime. Hence, instead of performing the "de-integration" operator, so called "inversion", the local wavespeed and propagation direction are calculated simultaneously from the spatial derivatives of the traveltime field (or wave front) (Lin et al., 2009; Gouédard et al., 2012). Since our previous study (Huang et al., 2013) has already revealed the isotropic structures for the two shear waves (V_{SV} and V_{SH}), we focus here on the azimuthal anisotropy. The variation of azimuthal anisotropy at different depths is carefully examined and compared with the surface strain-rate and SKS splitting to build up comprehensive perspectives about the crustal deformations for the southeastern Tibetan Plateau.

4.2 Eikonal tomography

4.2.1 Ambient noise data and Rayleigh wave Green's function

We use ambient seismic noise data from a temporary array containing 298 broadband seismometers in western Sichuan Province, China (Figure 4-1). Only the records of the year 2007 are used because they are sufficient to extract stable surface

wave Green's functions (Yao et al., 2007; Bensen et al., 2007). Following our previous studies (Yao et al., 2006; Huang et al., 2013), Rayleigh wave Green's functions between two stations are extracted from noise cross-correlation functions (CFs) of the vertical components. In this study a CF is retained for analysis if (1) its effective stacking length is larger than three months and (2) its signal-to-noise ratio (SNR) (Bensen et al., 2007; Huang et al., 2013) is larger than five. Figure 4-2 is an example of all the extracted CFs connecting a virtual "source" station KCD10 and other stations as "receivers". Phase velocity dispersion curves in period band 6-40 s are then measured from the Green's functions (Yao et al., 2006). There are more than 5000 measurements for most of the periods considered (Figure 4-3), which ensures accurate estimation of the wave front to perform Eikonal tomography.

4.2.2 Eikonal equation

The complete form of the Eikonal equation is (Wielandt, 1993; Shearer, 1999):

$$\left|\nabla t(\mathbf{r}, \mathbf{r}_s)\right|^2 = \frac{1}{c^2(\mathbf{r})} + \frac{\nabla^2 A}{A\omega^2} \tag{4.1}$$

where $t(\boldsymbol{r}, \boldsymbol{r}_s)$ is the traveltime from source $\boldsymbol{r}_s$ to location $\boldsymbol{r}$, $c(\boldsymbol{r})$ is the local wavespeed, A is the amplitude of the propagating wave, and ω is the angular frequency. If the frequency ω is high or the spatial variation of amplitude A is small, the second term on the right hand side is very small compared to the first term. In our surface wave study, the local wavespeed varies slowly and smoothly based on two facts: first, the results from traditional tomography (Chapter 3) reveal small and smooth variations of

phase velocity; second, the progression of wave front only deflects slightly from perfect circles (Figure 4-4). So the amplitude of the wavefield also changes slowly and smoothly and its 2nd-order spatial derivatives are of small magnitude (Lin et al., 2009; Gouédard et al., 2012). Therefore, despite the fact that we cannot completely recover the amplitude of the Green's function from ambient noise interferometry (Weaver and Lobkis, 2004); the second term of Eq. (4.1) is ignored. We obtain the standard and vector forms of the Eikonal equation:

$$\left|\nabla t(\mathbf{r}, \mathbf{r}_s)\right|^2 = \frac{1}{c^2(\mathbf{r})} \quad \text{and} \tag{4.2}$$

$$\nabla t(\mathbf{r}, \mathbf{r}_s) = \frac{1}{c(\mathbf{r})}\hat{\mathbf{k}}, \tag{4.3}$$

where $\hat{\mathbf{k}}$ is the unit vector in the wave propagating direction. Once we have obtained the traveltime field across the entire study region, the computation of local wavespeed *c(r)* and propagation direction is straightforward.

4.2.3 Minimum curvature interpolation

Successful implement of Eikonal tomography depends on the accurate estimation of traveltimes in target region. As measurements are only available at station locations, interpolation is necessary to get traveltimes and their gradients on regular grids. Since we assume slowly and smoothly varying wavespeed, the traveltime and its gradient should also be smooth and slowly varying. In this study, we use a minimum curvature method, which minimizes the total squared curvature of the interpolated field, to approximate the traveltimes (Briggs, 1974; Sandwell, 1987):

$$t(\mathbf{r}) = \sum_{j=1}^{N} \alpha_j \phi_j(\mathbf{r}) \tag{4.4}$$

The traveltime field is the linear combination of bi-harmonic basis functions. Following Sandwell (1987), the j^{th} basis function ϕ_j is defined on the j^{th} data point $\boldsymbol{r}_j$:

$$\phi_j(\mathbf{r}) = |\mathbf{r} - \mathbf{r}_j|^2 \cdot \left[\ln(|\mathbf{r} - \mathbf{r}_j|) - 1\right] \tag{4.5}$$

So there are as many basis functions as data points. The coefficient α_j are determined from the linear equation system:

$$t(\mathbf{r}_i) = \sum_{j=1}^{N} \alpha_j \phi_j(\mathbf{r}_i) \quad , \tag{4.6}$$

where $\boldsymbol{r}_i$ is the location of the i^{th} (i = 1, 2, …, N) data point. By Eq. (4.6) we require the interpolated traveltime have values equal to the measured traveltimes at the data points. The gradient of the traveltime, i.e. the local wave slowness and propagation direction, is calculated from the gradient of the basis functions:

$$\nabla\phi_j(\mathbf{r}) = 2(\mathbf{r} - \mathbf{r}_j)\left[2\ln(|\mathbf{r} - \mathbf{r}_j|) - 1\right] \tag{4.7}$$

The direct application of the above interpolation scheme may fail near the virtual source station and the edges of the array. In a smooth medium, the asymptotic expression of the traveltime is in proportion to the travel distance $|\boldsymbol{r} - \boldsymbol{r}_s|$. Its gradient has a singular point at source location $\boldsymbol{r}_s$, and thus cannot be correctly estimated by the continuous and smooth basis functions in Eq. (4.7). For this reason, Lin et al. (2009) remove the region within two wavelengths of the source station. In this study, this source region elimination cannot be afforded due to the small size of research region (about $5^\circ \times 6^\circ$), especially at longer periods. For example, the 30 s Rayleigh wave has a wavelength of about 100 km or 1°. The removal of area within two wavelengths

would exclude nearly all the study region. At large distance, the basis functions increase in the form of $|r^2 lnr|$, much larger than the asymptotic form $|r|$ of the traveltime. Hence, the interpolation accuracy reduces dramatically near the edges of the array.

An alternative method is to interpolate only the perturbed traveltime. The total traveltime is then divided into two parts:

$$t(\mathbf{r}, \mathbf{r}_s) = t_0(\mathbf{r}, \mathbf{r}_s) + t_1(\mathbf{r}, \mathbf{r}_s) = |\mathbf{r} - \mathbf{r}_s| / c_0 + t_1(\mathbf{r}, \mathbf{r}_s) \qquad (4.8)$$

where $t_0(\mathbf{r}, \mathbf{r}_s)$ is traveltime based on a reference medium with homogeneous wavespeed c_0, and $t_1(\mathbf{r}, \mathbf{r}_s)$ is the perturbed traveltime which reflects the wavespeed perturbations. For simplicity, the reference wavespeed c_0 is the average of all the raw measurements and it may be different a little from the average of the final tomography results. Accordingly, the gradient of traveltime, e.g. the slowness in wave propagation direction, also has two terms:

$$\frac{1}{c(\mathbf{r})}\hat{\mathbf{k}} = \nabla t(\mathbf{r}, \mathbf{r}_s) = \nabla t_0(\mathbf{r}, \mathbf{r}_s) + \nabla t_1(\mathbf{r}, \mathbf{r}_s) = \frac{1}{c_0}\nabla|\mathbf{r} - \mathbf{r}_s| + \sum_{j=1}^{N} \alpha_j \nabla \phi_j(\mathbf{r}) \qquad (4.9)$$

The resulting traveltime surfaces and wavespeed maps for the rays from the virtual source KCD10 are illustrated in Figures 4-4 to 4-6. The circle-like contours of the total traveltime in Figure 4-4 reveal the wave front propagating away from the source along the surface of the earth. Their deviations from perfect circles reflect local wavespeed perturbations. As analyzed above, we observe great improvement in the wavespeed calculation near the source station and the edges of the study region if only the perturbed traveltime is involved in interpolation (Figures 4-5a, b and 4-6a, b). We should point out that in this step we only aim to improve the interpolation accuracy

for a cone-shaped field (as the surface wave traveltime field). Noises and uncertainties in data will be discussed in the next step.

4.2.4 Damping and smoothing in interpolation

As mentioned above, we have as many basis functions as data measurements. Hence if the measured traveltime data are not distorted, the above system of linear equation (4-6) has a unique solution for the unknown coefficients α_j's, and the obtained traveltime surface passes the data points exactly. However, this exact fitting may cause local oscillation and large overshoot when there is noise in data (Sandwell, 1987; Lin et al., 2009; Gouedard et al., 2012). This effect is not so clearly illuminated in traveltime maps (Figure 4-5b) but significant in wavespeed maps, which amplifies the high-frequency oscillations due to the spatial derivative (Figure 4-6b). Therefore, we construct a surface which only approximately fits the data points alternatively. Sophisticated algorithms can be designed for this purpose, for example, using a subset of the total basis functions or adding extra terms to minimize oscillations in the linear inversion system of Eq. (4.6). In this study, to be simple and also effective we apply a damping term in the linear inversion system of Eq. (4.6). The large oscillations, which in nature are coefficients before some basis functions, are suppressed (Figure 4-6c). Even using data from only one source station, structures that are consistent with known geology begin to emerge (Figure 4-10). Relative high phase velocities are observed in the interiors of the sub-blocks; and low anomalies are observed on some faults.

Further, giving that surface waves can only resolve structures comparable to or larger than their wavelength, we apply a 2-D Gaussian filter to smooth the obtained wavespeed. This procedure plays a similar role as the correlation length in the model regularization term in tradition tomography (Yao et al., 2010; Huang et al., 2013). To some extent, the selection of the standard deviation of the Gaussian function is subjective. Experiments show that an appropriate choice is 1/4 of the reference wavelength ($c_0 \cdot T/4$) with a minimum value of one grid size here (0.125°, or about 14 km). The smoothing does not change the pattern or distribution of the wavespeed anomalies, but it reduces their magnitude and increases their wavelength (Figures 4-5d and 4-6d).

Finally, we perform a quality control for the resulting wavespeed maps. We only retain regions with good data coverage (Lin et al., 2009). First, a circle centered at the source with radius of two wavelengths or 100 km, whichever is smaller, is removed. Second, the location is only retained if there are data in at least three of the four quadrants of the East-West and North-South axes within 150 km distance (Figure 4-6d).

4.3 Phase velocity and anisotropy maps

4.3.1 Azimuthal anisotropy at a single location

The algorithm in section 2 is applied to the wave fronts (traveltimes) of all virtual sources. Then for each location in the study region we have many measurements of wavespeed and corresponding propagation directions (Figure 4-7). Although

scattering is large, we observe cosine variation with 180° periodicity. To stabilize the anisotropy analysis we first calculate the mean and standard deviation of the phase velocity in angle bins of 20° width:

$$\bar{c} = \frac{1}{n}\sum_{i=1}^{n} c_i \tag{4.10}$$

$$\sigma_c^2 = \frac{1}{n(n-1)}\sum_{i=1}^{n}(c_i - \bar{c})^2 \tag{4.11}$$

where n is the total number of phase speeds in a specific angle bin. Since standard deviation is dramatically reduced for large number of measurements, which is not reasonable physically, we set a minimum value of 1% of the mean value for the standard deviation.

In a horizontal transverse isotropic (HTI) medium the phase velocity of Rayleigh wave has the form (Smith and Dahlen, 1973):

$$c(\omega,\psi) = c_0(\omega) + a_0(\omega) + a_1(\omega)\cos 2\psi + a_2(\omega)\sin 2\psi \tag{4.12}$$

where c_0 is the reference phase velocity and a_0 and a_i (i = 1, 2) are the isotropic phase velocity perturbation and azimuthal anisotropy coefficients, respectively. These coefficients can be determined from weighted least-square fitting of the means and standard deviations in Eq. (4.10) and (4.11). The fast direction ψ_0 and amplitude of anisotropy A are then calculated from $\psi_0 = 1/2 \cdot \arctan(a_2/a_1)$ and $A = \sqrt{a_1^2 + a_2^2}$.

4.3.2 Resolution test

It is always important to check the resolution ability in tomography. The incomplete resolution of the isotropic velocity may result in artificial anisotropy

(Appendix 4A). So we perform separate checkerboard tests for isotropic and anisotropic phase velocity. For the isotropic model, the smallest resolvable anomaly is about 0.75° at both short and long periods (Figure 4-8). The anisotropic tests are on a model composed of realistic isotropic phase velocity model (Figure 4A-3a) from our previous study (Huang et al., 2013) and checkerboard anisotropy. It also reveals resolution of about 0.75° (Figure 4-9).

The resolution of surface wave tomography is determined by two factors: the wavelength and the data density or inter-station distance. The influence of wavelength is reflected in the Gaussian filter. The standard deviation of the Gaussian function is about 14 and 25 km for the 10 and 30 s Rayleigh waves, respectively, both of which are much smaller than the 0.75° (about 83 km) resolution. This suggests that the resolution is mainly determined by data density in this study. There are about 18,000 rays for both the 10 s and 30 s Rayleigh waves (Figure 4-3). The average ray number for each source is about 150 if some stations with only fewer measurements are ignored. So for this 5°×6° study region the average inter-station distance is about 50 km or 0.5°. Therefore, our checkerboard experiments show that at least three data points are required in one anomaly cycle (twice of the single anomaly) to obtain satisfactory results, a little larger than the Nyquist sampling rate. We should also mention that the resolution of 0.75° at 10 s period is larger than that of 0.5° in traditional tomography (Huang et al., 2013). The traditional tomography uses all the raypaths simultaneously. In Eikonal tomography the calculation is based on the rays from one source and information from crossing rays are not used. So only the average

wavespeeds are obtained between data points, resulting in lower resolution than traditional tomography.

4.3.3 Phase velocity and anisotropy map

The isotropic phase velocity reveals very similar patterns as our previous study (Huang et al., 2013). At short periods (Figure 4-10a), the Sichuan Basin exhibits strong low anomaly between the Longmenshan and Longquan faults, representative of the thick sediments in the foreland basin (Meng et al., 2005; Richardson et al., 2008). Low anomalies are also found in the Shangrila block, reflecting felsic and volcanic rock of the Yidun unit (Wang et al., 2000; Yang et al., 2012). In contrast, relatively high anomalies are found in the interiors of the Longmenshan, Yajiang, and Central Yunnan blocks. At longer periods (Figure 4-11a), the study region can be approximately divided into three anomalous sub-regions. The high phase velocity in the Sichuan Basin indicates a cold and rigid basin root. The high Plateau, including the Longmenshan, Yajian, and Shangrila blocks, shows strong low phase velocity which, we suggest, reflects a relative higher temperature in the middle and lower crust. The Central Yunnan and South China blocks have normal phase velocities.

The azimuthal anisotropy exhibits patterns consistent with known geology and results of a previous study (Yao et al., 2010). At short periods (Figure 4-10c), the fast direction is NW-SE in the Tibetan Plateau and turns to N-S in the Central Yunnan block, consistent with the clockwise rotation of the surface movement from GPS observations (Shen et al., 2005). The fast direction is NE-SW near the Longmenshan

fault, parallel to the fault strike. At long periods (Figure 4-11c), although the fast directions of the anisotropy are also consistent with a clockwise rotation in the high Plateau and Central Yunnan block, they exhibit large angular differences than those at the short period. For example, the fast directions are more parallel to fault strike near the Xianshuihe fault, and they are NE-SE near the Lijiang-Muli fault line, different from the nearly N-S direction at short periods. The anisotropy is relatively small in the Sichuan Basin and South China block at both short and long periods. The isotropic perturbation and amplitude of anisotropy have posterior errors of about or less than 0.5% in the interior of the study region, which are small compared to the magnitude of the perturbations themselves. We conclude, therefore, that the wavespeed anomalies and anisotropy patterns are robust.

4.4 Shear wave speed and anisotropy

4.4.1 NA inversion for anisotropic model

Following Montagner and Nataf (1986), the Rayleigh wave phase velocity perturbation $\delta c(\omega,\psi)$ in a slightly azimuthal anisotropic medium is expressed as:

$$\delta c(\omega,\psi) = \int_0^H \left[\frac{\partial c}{\partial A}(\delta A + B_c \cos 2\psi + B_s \sin 2\psi) + \frac{\partial c}{\partial L}(\delta L + G_c \cos 2\psi + G_s \sin 2\psi) \right] dz \tag{4.13}$$

The six parameters A, L, $B_{s,c}$, and $G_{s,c}$ are linear combinations of standard elastic coefficients C_{ij}. They determine the transversely isotropic and anisotropic parts of the compressional velocity V_P and vertically polarized shear velocity V_{SV} (Crampin et al.,

1984; Montagner, 2007):

$$V_P = \sqrt{\frac{A + B_c \cos 2\psi + B_s \sin 2\psi}{\rho}} \tag{4.14}$$

$$V_{SV} = \sqrt{\frac{L + G_c \cos 2\psi + G_s \sin 2\psi}{\rho}} \tag{4.15}$$

where ρ is the density. Comparison of Eq. (4.12) and Eq. (4.13) allows us to separate the isotropic and anisotropic terms:

$$a_0(\omega) = \int_0^H \left[\frac{\partial c(\omega)}{\partial A} \delta A + \frac{\partial c(\omega)}{\partial L} \delta L \right] dz \tag{4.16}$$

$$a_{1,2}(\omega) = \int_0^H \left[\frac{\partial c(\omega)}{\partial A} B_{c,s} + \frac{\partial c(\omega)}{\partial L} G_{c,s} \right] dz \tag{4.17}$$

We perform a two-step Neighborhood Algorithm (NA) to estimate these parameters (Sambridge, 1999a, b). The first step is to estimate the isotropic V_{SV} (i.e., L) using the isotropic part of the Rayleigh wave dispersion data, i.e. $c_0(\omega) + a_0(\omega)$. The model settings and parameter selections are the same as our previous study (Huang et al., 2013). The isotropic V_P (i.e., A) is linked to V_{SV} using Poisson's ratios from a receiver function study (Xu et al., 2007); and density ρ is calculated using an empirical relationship (Brocher, 2005). The crust is divided equally into three layers for the entire study region, and the upper crust of the Sichuan Basin is further equally divided into two layers to better account for the velocity changes of the shallow crust due to thick sediments there.

Then sensitivity kernels $\partial c(\omega)/\partial A$ and $\partial c(\omega)/\partial L$ are calculated and used in the second step NA inversion for $G_{c,s}$ and $B_{c,s}$ using the anisotropic part data, i.e. $a_0(\omega)$. As for A in the first step (isotropic) inversion, we do not really include $B_{c,s}$ in the NA

searching but link them with $G_{c,s}$:

$$\frac{B_{c,s}}{A} = \gamma \frac{G_{c,s}}{L} \tag{4.18}$$

If we assume the relative magnitudes of the anisotropy are the same for V_P and V_{SV}, the coefficient γ is equal to 1. After the two-step inversion, we obtain both the isotropic and anisotropic terms of the shear-wave speed:

$$V_{SV} \approx \sqrt{\frac{L}{\rho}}\left(1 + \frac{G_c \cos 2\psi}{2L} + \frac{G_s \sin 2\psi}{2L}\right) \tag{4.19}$$

The fast direction and relative magnitude (w.r.t isotropic wavespeed) are $\psi_0 = 1/2 \arctan(G_s/G_c)$ and $A_{SV} = \sqrt{(G_c/2L)^2 + (G_s/2L)^2}$, respectively.

4.4.2 The 3-D heterogeneity and azimuthal anisotropy

Shear-wave speed V_{SV} and its azimuthal anisotropy are shown in Figure 4-12. The depths of 5 and 10 km are representative of the upper crust. So V_{SV} and anisotropy are only different in the Sichuan Basin. The depths of 25 and 40 km are representative of the middle and lower crust, respectively. The main features of both the V_{SV} and anisotropy maps have already been clearly exhibited in the phase velocity maps (Figures 4-10 and 4-11) due to the period-depth correspondence of the surface wave sensitivity kernels (Mooney et al., 1998). Since the structures revealed in the isotropic V_{SV} are very similar to the results in our previous study and have been fully discussed there (Huang et al., 2013), in this paper, we only introduce some large features and do not go into details of their geological implications.

For the Sichuan Basin, the thick sediments and old stable basin root are well

represented by the significant low V_{SV} in the upper crust and high V_{SV} in the middle and lower crust. Its V_{SV} gradient in the depth direction is the largest among all the sub-blocks. For the three blocks in the high Plateau, i.e. the Longmenshan, Yajiang, and Shangrila blocks, in the upper crust, we observe relatively low V_{SV} on major faults, in compared to the interior of the blocks. This may be indication of damage zones on the Xianshuihe, Litang, and Chenzhi faults. In the middle and lower crust, all three blocks exhibit very low V_{SV} and the most dominant low anomalies are within the Yajiang and Shangrila blocks. This feature suggests higher temperature and possible larger deformation to the south of the Xianshuihe fault than to the north, consistent with Liu et al. (2003). In general, throughout the crust the Central Yunnan block always has higher V_{SV} than its surrounding sub-blocks, which may be evidence of the intruded material from the mantle (Lou and Wang, 2005). The South China block also reveals low V_{SV} in the middle and lower crust, which suggests relative high temperature and weakened rock mechanics. The posterior errors for the isotropic V_{SV} are about 0.5% (about 0.02 km/s) in the upper crust and about 1% (about 0.04 km/s) in the middle and lower crust (Figure 4-13); these values are small compared to the magnitudes of the revealed wavespeed anomalies (which can reach up to 0.3 km/s). Therefore, the structures revealed in the V_{SV} anomalies are reliable.

Azimuthal anisotropy is prominent in our study region. In the upper crust (Figure 4-12a, b), NW-SE fast directions are observed in the northwestern part of the Longmenshan and Yajiang blocks, and they gradually change to N-S in the Central Yunnan block. This pattern of anisotropy resembles the clockwise rotation of the

surface velocity field from GPS observations (Shen et al., 2005). Near major faults, e.g. the Longmenshan, Xianshuihe, Lijiang, and Shimian faults, the fast directions are parallel to the strikes of the faults, which may be reflection of cracks or fractures in the damage zones of these faults. Anisotropy is relatively small in the interior of the Sichuan Basin and South China block. The large anisotropies near the eastern edge of our study region are artifacts due to the combined effects of incomplete angular coverage and recovery of isotropic wavespeed (Figure 4A-3). In the middle and lower crust (Figure 4-12c, d), the change in orientation of the fast directions from NW-SW in the Longmenshan and Yajiang blocks to N-S in the Central Yunnan block is also observed. However, angular differences are obvious when compared with the upper crust. The fast directions are more parallel to the strike of the Xianshuihe faults in the Longmenshan and Yajiang blocks; they are more in the direction of NE-SW rather than N-S near the Lijiang-Muli fault zone; and no obvious anisotropy parallel to fault strike is found near the Simian fault. Anisotropy is relatively small in the Sichuan Basin and South China block as in the upper crust. These results are generally consistent with a previous study of azimuthal anisotropy for a larger region (Yao et al., 2010). The fast directions in the upper crust are nearly the same in the areas where our studies overlap. But the fast directions in the lower crust observed here are closer to their results in the uppermost mantle. In this study we use many more measurements, so we expect that both the isotropic wavespeed and anisotropy are better constrained. In fact, the fast directions change more gradually in depth direction in this study, which may be more reasonable for the real earth.

The posterior errors of the amplitude of the anisotropy are about 0.3% in the upper crust and 0.5% in the middle and lower crust in the interior of our study region (Figure 4-14). These values are small compared to the revealed anisotropy (about 3%), so our results about the anisotropy are significant. Near the edges, especially the northern and southern margins, the uncertainties can reach up to 2% due to limited angular coverage and incomplete recovery of the isotropic V_{SV} (Figure 4A-3). Therefore, we do not discuss the magnitude and directions changes of the anisotropy in the marginal areas. The fast direction of the anisotropy is better determined compared to its magnitude. The average posterior error is about 5° for our study region (Figure 4-16). The errors are large and reach to 20° only at locations where the anisotropy is small and thus shows no clear preferred fast direction.

4.5 Discussion

4.5.1 Phase velocity maps from Eikonal and traditional tomography

Since NA inversion schemes and parameter settings for the isotropic V_{SV} are the same in this research and our previous traditional tomography study (Huang et al., 2013), the differences in isotropic V_{SV} between the two studies are reflection of their differences in phase velocities. In general, Eikonal tomography generates smoother phase velocity maps, especially at short period. We now investigate possible reason.

The resolution of surface wave tomography is determined by both data density and wavelength. In our surface wave tomography using traditional method (Huang et al., 2013), the correlation length thus the anomaly size determined from data density

is always smaller than one wavelength; therefore, the smallest anomaly that can be resolved is of size of about one wavelength. However, Eikonal tomography only uses rays from one virtual source at a time; thus the effective data density is much smaller than that in traditional tomography. As we have shown in section 3.2, the smallest resolvable anomaly size is about 0.75° (83 km) for both short and long periods, which is much larger than the wavelength of short period surface waves (i.e. about 30 km for 10 s Rayleigh wave) and more or less the same as that of long period surface waves (i.e. about 100 km for 30 s Rayleigh wave).

We also need to point out that it is due to the consideration of resolution that we use different data sets in these two studies. In the previous research, we retain Green's functions with SNR larger than 10, and there are more than 5000 measurements for almost all the periods between 4-40 s. These numbers are sufficient and increasing measurements would not improve the resolution in traditional tomography (Griot et al., 1998). In this study, we use a smaller SNR of five in Green's function selection in order to include more measurements to improve resolution. This reduction of SNR results in about 50% more measurements. If we use the same SNR (i.e. 10) as in the previous study, we would expect smoother phase velocity variations and larger differences between results of Eikonal and traditional tomography.

4.5.2 Azimuthal and radial anisotropy

Azimuthal and radial anisotropy reflect different aspects of the angular variation of wavespeed. Azimuthal anisotropy, or transverse isotropy with a horizontal

symmetric axis, measures the variation of wavespeed with polarization direction in the horizontal plane. Radial anisotropy, or transverse isotropy with a vertical symmetric axis, measures the difference between the average wavespeed on the horizontal plane and in the vertical direction. Therefore, a thorough study of the two kinds of anisotropy is necessary to understand the structure and deformation pattern better.

In our previous research (Huang et al., 2013), we observed ubiquitous low velocity zones (LVZs) and positive radial anisotropy ($V_{SH}>V_{SV}$) in the middle and lower crust; and we also observe a clear negative correlation between the magnitude of the low speed anomaly and radial anisotropy. These observations lead to three arguments: first, low wave speed in the middle and lower crust indicates relatively higher temperature and thus weakened rock mechanics in our study region; second, positive radial anisotropy reveals the dominant deformation is on the horizontal plane; third, the correlation between LVZs and radial anisotropy confirms that larger deformation occurs in more mechanically weakened regions.

In this study, we do not observer simple correlation between wavespeed anomaly and azimuthal anisotropy (Figure 4-12). Azimuthal anisotropy in middle and lower crust is not dominant over that in the upper crust. In fact, azimuthal anisotropy seems to have a little larger amplitude in the lower crust than in the upper crust; but the difference is probably not significant. The correlation between the magnitudes of V_{SV} anomaly and azimuthal anisotropy is not clear. For example, the Yajiang and Shangrila blocks, where the most prominent low V_{SV} anomaly resides in the middle

and lower crust, do not exhibit larger anisotropy than the adjacent Longmenshan and Central Yunnan block. This lack of clear correlation between V_{SV} and anisotropy was also found in Yao et al. (2010).

The different behavior of the two anisotropies may have different reasons. Experiments show that both wavespeed and azimuthal anisotropy cannot be resolved well near the boundaries of anomaly bodies with opposite properties (opposite sign of anomaly for wavespeed and perpendicular fast directions for azimuthal anisotropy) (Figures 4-8 and 4-9). The radial anisotropy is calculated from the two speeds V_{SV} and V_{SH}, so it has the same patterns of incomplete recovering or smearing as the two wavespeeds. But the calculation of azimuthal anisotropy is independent of wavespeeds and thus can have different local resolutions. For example, the middle and lower crust of the Yajiang and Shangrila blocks is dominated by low wavespeed anomaly and large positive radial anisotropy. In the middle of this low wavespeed zone near the Chenzhi fault, the azimuthal anisotropy changes its fast direction from NW-SE in the north to N-S in the south and only small azimuthal anisotropy is observed. We believe that the small amplitude of azimuthal anisotropy does not necessarily mean little or no anisotropy but rather limited resolution between two areas with perpendicular fast directions. Therefore, it is easier to observe magnitude correlation between radial anisotropy and V_{SV} anomaly than between azimuthal anisotropy and V_{SV}.

Although the amplitude correlation between azimuthal anisotropy and V_{SV} anomaly is not obvious, we can analyze the deformation variations in the crust

through comparing the fast directions at different depths (Figure 4-15). Between the upper and middle crust, the angular differences of the fast directions are very small in all the sub-blocks except the Sichuan Basin. The angular differences for the Sichuan Basin are distributed nearly homogeneously over the 0^{o} – 90^{o} range. This is not surprising considering the small anisotropy and large angular uncertainty in the Basin. Between the upper and lower crust, the angular differences are larger in general. For example, near the Xianshuihe fault the fast directions are more aligned parallel to the fault strike in the middle and lower crust; and in the Central Yunnan block the near N-S directions in the upper crust change to NE-SW in the lower crust (Figure 4-12). Therefore, the deformation in the upper and middle crust may be correlated; but the correlation between the upper and lower crust is weaker.

Combining the radial and azimuthal anisotropies, we have a more comprehensive picture of the deformation in the SE Tibet and its adjacent regions. Our results show that both the radial and azimuthal anisotropies vary in different layers of the crust, which suggests different deformation patterns in these layers. The largest deformation occurs in the middle and lower crust and mainly on near horizontal planes, revealing positive radial anisotropy in most of our study region. The curvilinear pattern of the fast directions of azimuthal anisotropy may reflect the movement direction of the material extruded from the central Tibet. The deformation or material movement is continuous from the Longmenshan and Yajiang blocks in the north to the Central Yunnan block in the south. But its magnitude may vary over our study region considering the spatial variations of the two kinds of anisotropy. The deformation may

go across the Xiaojiang fault into the South China block, because both radial and azimuthal anisotropy are observed there, but with smaller magnitude. These results indicate a weakened middle and lower crust and a decoupled lithosphere, at least locally, in the southeastern Tibetan Plateau.

4.5.3 Comparison with shear-wave splitting

We make two assumptions in order to compare the anisotropy from this study with SKS splitting. Firstly, we assume the anisotropy is mainly related to the current deformation. However, frozen anisotropy caused by former deformations may cause the comparison not so straightforward. Secondly, we assume A-type lattice preferred orientation (LPO) in mineral following previous studies (Sol et al., 2007; Wang et al., 2008). So the fast direction of the azimuthal anisotropy is parallel to the flow direction.

We calculate the fast direction and delay time of shear-wave splitting caused by azimuthal anisotropy in the crust. These splitting results for the crustal anisotropy are then compared with the SKS splitting for the whole crust and mantle (Lev et al., 2006; Sol et al., 2007; Wang et al., 2008) (Figure 4-16). The synthetic delay times are large to the west of the Longmenshan-Simian-Xiaojiang fault line (black bars), where the values can reach up to 0.5 s. To the east of this fault line, the predicted delay time is very small, less than 0.2 s. The discrepancy between the synthetic and measured splitting is large in both magnitude and direction in most of our study regions. This large difference indicates that the deformations in the crust and in the mantle are not

coherent. In some localized areas, i.e. near the northern Xianshuihe fault and the northern part of the Central Yunnan block, we observe some consistency between the synthetic and measured splitting. In these areas, the delay time from crustal anisotropy can contribute up to 50% of the entire delay time. By itself, however, the consistency does not necessarily mean coupled lithosphere. The deformation may still vary in depth direction, but with less difference as in other regions.

4.6 Conclusions

In this paper, we apply the Eikonal equation to Rayleigh wave Green's functions to study the shear wave speed V_{SV} and its azimuthal anisotropy for the southeastern Tibetan Plateau and adjacent regions. The isotropic wave speed model is in good agreement with surface geology and reveals nearly similar patterns as our previous study from traditional tomography (Huang et al., 2013). Significant V_{SV} contrasts are observed between the high Plateau and Sichuan Basin throughout the entire crust, reflecting distinct tectonics on the two sides of the Longmenshan fault. In contrast, V_{SV} varies smoothly from the high Plateau to the Central Yunnan block, reflecting gradual change over the Lijiang-Muli faults zone. Ubiquitous low wavespeed zones in the middle and lower crust of the high Tibetan Plateau are consistent with increased temperature and low mechanical strength, and these zones may play a role in material transport from central Tibet. Strong azimuthal anisotropy is observed mainly in the high Plateau and the Central Yunnan block. Although, curvilinear pattern associated with the clockwise rotation around the Eastern Himalayan Syntaxes is observed in the

entire crust, angular differences of anisotropy are large between the upper and lower crust, suggesting different deformation patterns at surface and in depth. This variation of deformation patterns at different depths is further confirmed by the comparison of the obtained anisotropy in the study with the GPS and SKS splitting results. Although we cannot rule out the influence of historic or frozen anisotropy, our results suggest a weakened middle and lower crust and a decoupled lithosphere in the SE Tibetan Plateau. There inferences are consistent with the channel flow in the middle and lower crust in our study region, but its extent and magnitude may vary spatially and be influenced by old structures and their different tectonic histories.

Appendix 4A: Azimuthal anisotropy and artifacts in inversion

In a horizontal transverse isotropic (HTI) medium the phase velocities of both Rayleigh and Love waves have the form (Smith and Dahlen, 1973):

$$c(\omega,\psi) = c_0(\omega) + a_0(\omega) + a_1(\omega)\cos 2\psi + a_2(\omega)\sin 2\psi + a_3(\omega)\cos 4\psi + a_4(\omega)\sin 4\psi \quad (4A.1)$$

where c_0 is the reference phase velocity and a_0 and a_i (i = 1 to 4) are the isotropic perturbation and coefficients for azimuthal anisotropy, respectively. In addition, 1-ψ anisotropy (with 360° periodicity) can rise from isotropic bias in inversion (Bodin and Maupin, 2008; Lin et al., 2011). Hence, we first test whether our data contains all or only parts of these anisotropic terms. For models with different anisotropic terms we compare their data fitting:

$$\chi^2 = \frac{1}{N}\sum_{i=1}^{N}\frac{(c_{i,pred} - \bar{c}_i)^2}{\sigma_{c,i}^2} \qquad (4A.2)$$

where $\bar{c}_i$ and $c_{i,pred}$ are the average phase velocity and its prediction in the i^{th} angle bin. It is not surprising that χ^2 reduces when more terms of anisotropy are introduced. Here we use 10 s Rayleigh wave for example (Figure 4A-1). We find that the fitting is greatly improved from isotropic case to anisotropic case with only *2-ψ* terms for most of the study region. Adding *1-ψ* and *4-ψ* terms does not reduce χ^2 much. This experiment is consistent with the theoretic study that the *2-ψ* terms have much larger amplitudes than the *4-ψ* terms (Smith and Dahlen, 1973). So we only include the *2-ψ* terms in our analysis for the azimuthal anisotropy.

Because of the regularization terms in model space and some other assumptions, the model cannot be fully resolved even with noise-free data. So the tomography results contain some artifacts which may influence our understanding and analysis for the structures. For example, artifacts in the checkerboard test for isotropic V_{SV} generate fake azimuthal anisotropy (Figure 4A-2). The recovered anomalies well exhibit the checkerboard pattern but with smaller amplitude. This deficit in anomaly amplitude is reflected and compensated in the angular variations of phase velocity at locations between the positive-negative anomalies. In directions connecting two high (low) anomalies the phase velocity is relatively higher (lower). Because the checkerboard is 180° symmetric, this kind of artifacts is shown as *2-ψ* azimuthal anisotropy. The magnitude of this artificial anisotropy can reach up to 2% with input isotropic anomaly of 8%. The magnitude of the artificial anisotropy greatly decreases for realistic isotropic model which has no clear periodicity (Figure 4A-3). Except for

edges of the study region, the amplitude of the *2-ψ* anisotropy is less than 0.5%. This asymmetric medium may cause 360° periodicity in phase velocity, e.g. *1-ψ* anisotropy (Lin et al., 2011). Since little or no *1-ψ* anisotropy is observed in our data (Figure 4A-1), we do not study this effect here. The experiments here reveal that we need to perform separated checkerboard tests for isotropic phase velocity and anisotropy in order to correctly analyze their resolutions. The isotropic test can use a checkerboard model similar to that in Figure 4A-2a; and the anisotropic test should uses a model with realistic isotropic phase velocity (as in Figure 4A-3a) and checkerboard anisotropy.

Appendix 4B: Phase velocity and anisotropy for Love wave

The Eikonal tomography scheme can also be applied to the Green's functions of Love waves. The variations of phase velocity with propagation angle for location (102°, 29°) are shown in Figure 4B-1. In contrast to the results of Rayleigh waves, the anisotropy is not obvious for both 10 and 30 s. This is further confirmed in the data fitting (Figure 4B-2). For most locations the χ^2 reduces less than 20% from the isotropic to the *2-ψ* anisotropic fitting. Introducing *1-ψ* and *4-ψ* anisotropy may improve data fitting at some locations. But these locations show little correlation with known Geology; they are more like scatters or random points. The finally results for the models only containing *2-ψ* anisotropy are shown in Figures 4B-3 and 4B-4. The isotropic V_{SH} are very close to our previous results of traditional tomography (Huang et al., 2013). And although the depth sensitively kernels are different from those of

Rayleigh waves, the V_{SH} perturbations show similar features as the V_{SV} anomalies. The anisotropy shows no clear pattern or connection with known Geology or the anisotropy from Rayleigh waves; and their amplitudes are small, always less than 2%.

Theoretically, in a slightly anisotropic medium the *4-ψ* terms of anisotropy for the Love waves have amplitudes comparable to the *2-ψ* terms (Smith and Dahlen, 1973). So the *4-ψ* terms are not negligible like those for the Rayleigh waves. So the azimuthal anisotropy for the Love waves are more complicated. In addition, usually the horizontal components of the seismic records have lower signal-to-noise ratio than the vertical components. So the Love waves always have fewer measurements than Rayleigh waves, especially at longer periods (> 25 s) (Lin et al., 2008; Huang et al., 2013). Due to these reasons, we do not include the Love waves in the text of our Eikonal tomography research.

References

Bai, D., M. J. Unsworth, M. A. Meju, X. Ma, J. Teng, X. Kong, Y. Sun, J. Sun, L. Wang, C. Jiang, C. Zhao, P. Xiao, and M. Liu, (2010), Crustal deformation of the eastern Tibetan plateau revealed by magnetotelluric imaging, *Nature Geosci.*, 3, 358-362, doi:10.1038/ngeo830.

Bensen, G.D., M.H. Ritzwoller, M.P. Barmin, A.L. Levshin, F. Lin, M.P. Moschetti, N.M. Shapiro, and Y. Yang, (2007), Processing seismic ambient noise data to obtain reliable broad-band surface wave dispersion measurements, Geophys. J. Int., 169, 1239-1260.

Bodin, T., and Maupin, V., (2008), Resolution potential of surface wave phase velocity measurements at small arrays, Geophys. J. Int., 172, 698–706, doi:10.1111/j.1365-246X.2007.03668.x.

Briggs, I.C., (1974), Machine contouring using minimum curvature, Geophysics, 39, 39-48.

Brocher, T.M., (2005), Empirical relations between elastic wavespeeds and density in the Earth's crust, Bull. Seism. Soc. Am., 95(6), 2081-2092.

Chen, Z., B. C. Burchfiel, Y. Liu, R. W. King, L. H. Royden, W. Tang, E. Wang, J. Zhao, and X. Zhang (2000), Global positioning system measurements from eastern Tibet and their implications for India/Eurasia intercontinental deformation, J. Geophys. Res., 105(B7), 16,215–16,227, doi:10.1029/2000JB900092.

Crampin, S., (1984), An introduction to wave propagation in anisotropic media, Geophysical Journal of the Royal Astronomical Society, 76, 17-28.

Dahlen, F.A., S.H. Huang, and G. Nolet, (2000), Frechet kernels for finite-frequency traveltimes— I. Theory, Geophysical Journal International, 141(1), 157-174.

de Hoop, M.V., and R.D. van der Hilst, (2005), On sensitivity kernels for 'wave-equation' transmission tomography, Geophysical Journal International, 160(2), 621-633.

England, P., and D. McKenzie, (1982), A thin viscous sheet model for continental deformation, Geophys. J. R. Astr. Soc., 70, 295-321.

England, P., and G. Houseman, (1986), Finite strain calculations of continental deformation, 2, Comparison with the India-Asia collision zone, J. Geophys. Res., 91, 3664-3676.

Flesch, L., J. Haines, W. Holt, (2001), Dynamics of the India-Eurasia collision zone, J. Geophys. Res., 106(B8), 16435-16460.

Gouédard P., H. Yao, F. Ernst, and R.D. van der Hilst, (2012), Surface wave eikonal tomography in heterogeneous media using exploration data, 191(2), 781-788, DOI: 10.1111/j.1365-246X.2012.05652.x

Huang, H., H. Yao, and R.D. van der Hilst (2010), Radial anisotropy in the crust of SE Tibet and SW China from ambient noise interferometry, Geophysical Research Letters, 37(21), DOI: 10.1029/2010GL044981.

Huang, H., Y. Li, Q. Liu, H. Yao, and R.D. van der Hilst (2013), High resolution tomography and radial anisotropy of SE Tibet and its surrounding regions using

ambient noise interferometry, in preparation.

Lev, E., M.D. Long, R.D. van der Hilst, (2006), Seismic anisotropy in Easter Tibet from shear wave splitting reveals changes in lithospheric deformation, Earth and planetary science letters, 251, 293-304.

Lin, F., M.P. Moschetti, and M.H. Ritzwoller, (2008), Surface wave tomography of the western United States from ambient seismic noise: Rayleigh and Love wave phase velocity maps, Geophys. J. Int., 173, 281-298.

Lin, F.-C., M.H. Ritzwoller, and R. Snieder, (2009), Eikonal tomography: surface wave tomography by phase front tracking across a regional broad-band seismic array, Geophysical Journal International, 177(3), 1091-1110.

Lin, F.-C., and M.H. Ritzwoller, (2011), Helmholtz surface wave tomography for isotropic and azimuthally anisotropic structure, Geophys. J. Int., 186, 1104-1120.

Liu, Q., R. D. van der Hilst, Y. Li, H. Yao, J. Chen, B. Guo, S. Qi, J. Wang, H. Huang, and S. Li, (2013), Dynamics of eastern Tibetan Plateau revealed by dense seismic array observations, in preparation.

Lou, H., and C. Wang, (2005), Wavelet analysis and interpretation of gravity data in Sichuan-Yunnan region, China, ACTA Seismologica Sinica, 18(5), 552-561.

Meng, Q., E. Wang, and Hu J., (2005), Mesozoic sedimentary evolution of the northwest Sichuan basin: Implication for continued clockwise rotation of the South China block, Geological Society of America Bulletin, 117 (3/4), 396-410. doi: 10.1130/B25407.

Molnar P., and P. Tapponnier, (1975), Cenozoic tectonics of Asia: Effects of a continental collision: Features of recent continental tectonics in Asia can be interpreted as results of the India-Eurasia collision, Science, 189, 419-426.

Montagner, J.P., and H.C. Nataf (1986), A simple method for inverting the azimuthal anisotropy of surface waves, J. Geophys. Res., 91(B1), 511–520, doi:10.1029/ JB091iB01p00511.

Montagner, J.-P., (2007), Upper mantle Structure: Global isotropic and anisotropic tomography, 2007, Treatise on Geophysics, Vol 1: Seismology and Structure of the Earth (Eds. A.M. Dziewonski, B. Romanowicz), Elsevier, 559-590.

Mooney, W.D., G. Laske, and G. Masters, (1998), CRUST5.1: a global crustal model at $5^{\circ} \times 5^{\circ}$, J. geophys. Res., 103, 727–747.

Nicolas, A., Boudier, F., and Boullier, A.M., 1973, Mechanisms of flow in naturally and experimentally deformed peridotites: American Journal of Science, v. 273, p. 853–876.

Royden, L.H., B.C. Burchfiel, R.W. King, E. Wang, Z. Chen, F. Shen, and Y. Liu, (1997), Surface deformation and lower crustal flow in eastern Tibet, Science, 276, 788-790.

Richardson, N.J., Densmore A.L., Seward D., Fowler A., Wipf M., Ellis M.A., Rong L., and Zhang Y., (2008), Extraordinary denudation in the Sichuan Basin: insight from low-temperature thermochronology adjacent to the eastern margin of the Tibetan Plateau, J. Geophys. Res., 113, B04409, doi: 10.1029/2006JB004739.

Sambridge M., (1999a), Geophysical inversion with a neighborhood algorithm –I. Searching a parameter space, *Geophys. J. Int.*, 138(2), 479-494, doi:

10.1046/j.1365-246X.1999.00876.x.

Sambridge M., (1999b). Geophysical inversion with a neighborhood algorithm –II. Appraising the ensemble, *Geophys. J. Int.*, 138(3), 727-746, doi: 10.1046/j.1365-246x.1999.00900.x.

Sandwell, D.T., (1987), Biharmonic spline interpolation of GEOS-3 and SEASAT altimeter data, Geophys. Res. Lett., 14(2), 139-142.

Shearer P., (1999), Introduction to seismology, Cambridge University Press, ISBN 0-521-66023-8 (hbk.).-ISBN 0-521-66953-7 (pbk), 237-240.

Shen, Z., J. Lv, M. Wang, and R. Burgmann, (2005), Contemporary crustal deformation around the southeast borderland of the Tibetan Plateau, *J. Geophys. Res.*, 110, B11409, doi:10.1029/2004JB003421.

Smith, M., and F.A. Dahlen, (1973), The azimuthal dependence of Love and Rayleigh wave propagation in a slightly anisotropic medium, Journal of Geophys. Research, 78(17), 3321-3333.

Sol, S., A. Meltzer, R. Burgmann, R.D. van der Hilst, R. King, Z. Chen, P.O. Koons, E. Lev, Y.P. Liu, P.K. Zeitler, X. Zhang, J. Zhang and B. Zurek, (2007), Geodynamics of the southeastern Tibetan Plateau from seismic anisotropy and geodesy, Geology, 35, 563-566.

Tapponnier, P., P. Molnar, (1976), Slip-line field-theory and large scale continental tectonics, Nature, 264, 319-324.

Tapponnier, P., G. Peltzer, A. Y. Le Dain, R. Armijo, and P. Cobbold, (1982), Propagating extrusion tectonics in Asia: New insights from simple experiments with plasticine, Geology, 10, 611 –616.

Wang, E., (1998), Late Cenozoic Xianshuihe-Xiaojian, Red River and Dali fault systems of southwestern Sichuan and central Yunnan, China, Spec. Pap, Geol. Soc, Am., 327.

Wang, E., B.C. Burchfiel, (2000), Late Cenozoic to Holocene deformation in southwestern Sichuan and adjacent Yunnan, China, and its role in formation of the southeastern part of the Tibetan Plateau, Geol. Soc. Am. Bull., 112, 413-423.

Wang, C.Y., L. M. Flesch, P. G. Silver, L.-J. Chang, and W. W. Chan (2008), Evidence for mechanically coupled lithosphere in central Asia and resulting implication, Geology, 36, 363–366, doi:10.1130/G24450A.1.

Weaver, R., O.I. Lobkis, (2004), Diffuse fields in open systems and the emergence of the Green's function (L), J. Acoust. Soc. Am., 116(5), 2731-2734.

Wielandt, E., (1993), Propagation and structural interpretation of nonplane waves, Geophys. J. Int., 113, 45-53.

Xu, L., S. Rondenay, and R. D. van der Hilst, (2007), Structure of the crust beneath the southeastern Tibetan Plateau from teleseismic receiver functions, *Phys. Earth Planet. Int.*, 165, 176-193, doi: 10.1016/j.pepi.2007.09.002.

Yang, T., Hou Z., Wang Y., Zhang H., and Wang Z., (2012), Late Paleozoic to Early Mesozoic tectonic evolution of northeast Tibet: Evidence from the Triassic composite western Jinsha-Garzê-Litang suture, Tectonics, 31, TC4004, doi: 10.1029/2011TC003044.

Yao, H., R. D. van der Hilst, and M. V. De Hoop, (2006), Surface-wave array

tomography in SE Tibet from ambient seismic noise and two-station analysis – I. Phase velocity maps, *Geophys. J. Int.*, 166, 732-744, doi: 10.1111/j.1365-246X.2006.03028.x.

Yao, H., C. Beghein, and R.D. Van der Hilst, (2008), Surface wave array tomography in SE Tibet from ambient seismic noise and two-station analysis – II. Crustal- and upper-mantle structure, Geoohys. J. Int., 173, 205-219.

Yao, H., R. D. van der Hilst, and J.P. Montagner, (2010), Heterogeneity and anisotropy of the lithosphere of SE Tibet from surface wave array tomography, Journal of Geophysical Research, 115, B12307, doi:10.1029/2009JB007142.

Zhang, S., and Karato, S.I., 1995, Lattice preferred orientation of olivine aggregates deformed in simple shear: Nature, v. 375, p. 774–777, doi:10.1038/375774a0.

Zhang, H., Roecker S., Thurber C.H., and Wang W. (2012). Seismic Imaging of Microblocks and Weak Zones in the Crust Beneath the Southeastern Margin of the Tibetan Plateau, Earth Sciences, Dr. Imran Ahmad Dar (Ed.), ISBN: 978-953-307-861-8, 159-202.

Zhang P., Z. Shen, and M. Wang, et al. (2004), Continuous deformation of the Tibetan Plateau from global positioning system data, *Geology*, 32(9), 809-812.

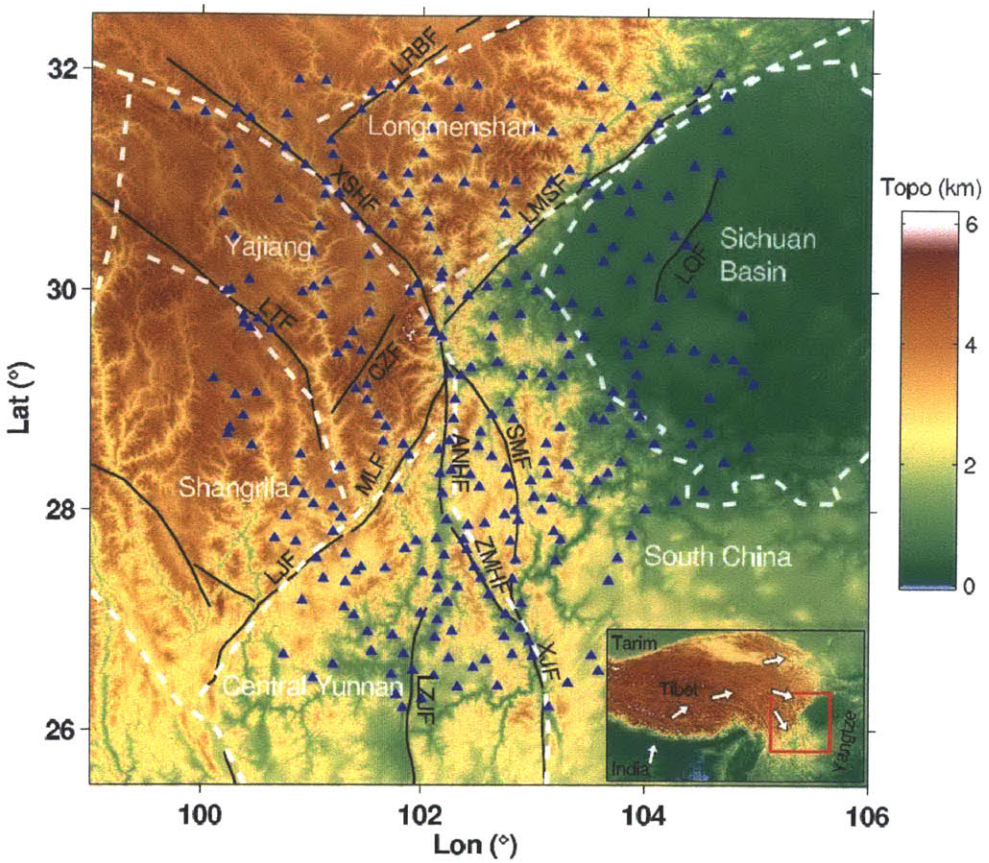

Figure 4-1. Topography, geological units and seismic stations used in this study. The topography is represented by the background color. The locations of seismic stations are depicted as blue triangles. Our study region can be approximately divided into six geological units according to GPS observations (Shen et al., 2005): the Longmenshan block, Yajiang block, Shangrila block, Central Yunnan block, Sichuan Basin, and the South China block. Their boundaries are depicted as thick white dash lines. Major faults are depicted as thin black lines and the abbreviations are: Longriba fault (LRBF), Xianshuihe fault (XSHF), Longmenshan fault (LMSF), Longquan fault (LQF), Litang fault (LTF), Chenzhi fault (CZF), Lijiang fault (LJF), Muli fault (MLF), Anninghe fault (ANHF), Zemuhe fault (ZMHF), Xiaojiang fault (XJF), Shimian fault (SMF), and Luzhijiang fault (LZJF) (after Wang et al., 1998; Wang and Burchfiel, 2000; Shen et al., 2005). The inset shows the location of our study region, as the red box, in the context of the whole Tibetan Plateau and its surrounding areas. The white arrows depict the approximate surface motion relative to the Yangtze Craton from GPS observations (Zhang et al., 2004; Shen et al., 2005).

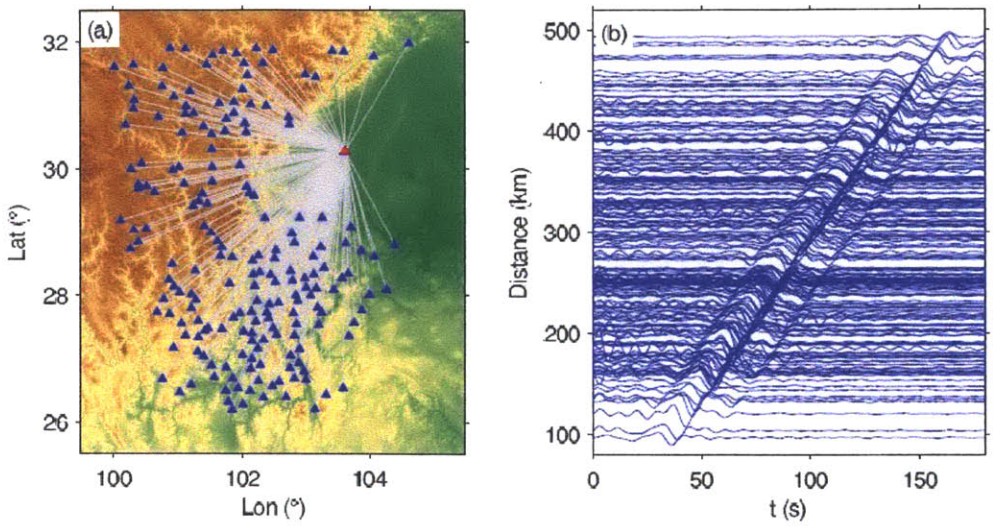

Figure 4-2. (a) All the raypaths related to virtual source station KCD10. The station KCD10 is shown as red triangle, and other stations are shown as blue triangles. (b) The cross-correlation functions (CFs) corresponding to the raypaths in (a). The CFs are filtered between period band 8 – 30 s, and only those with signal-to-noise ratio larger than 10 are plotted.

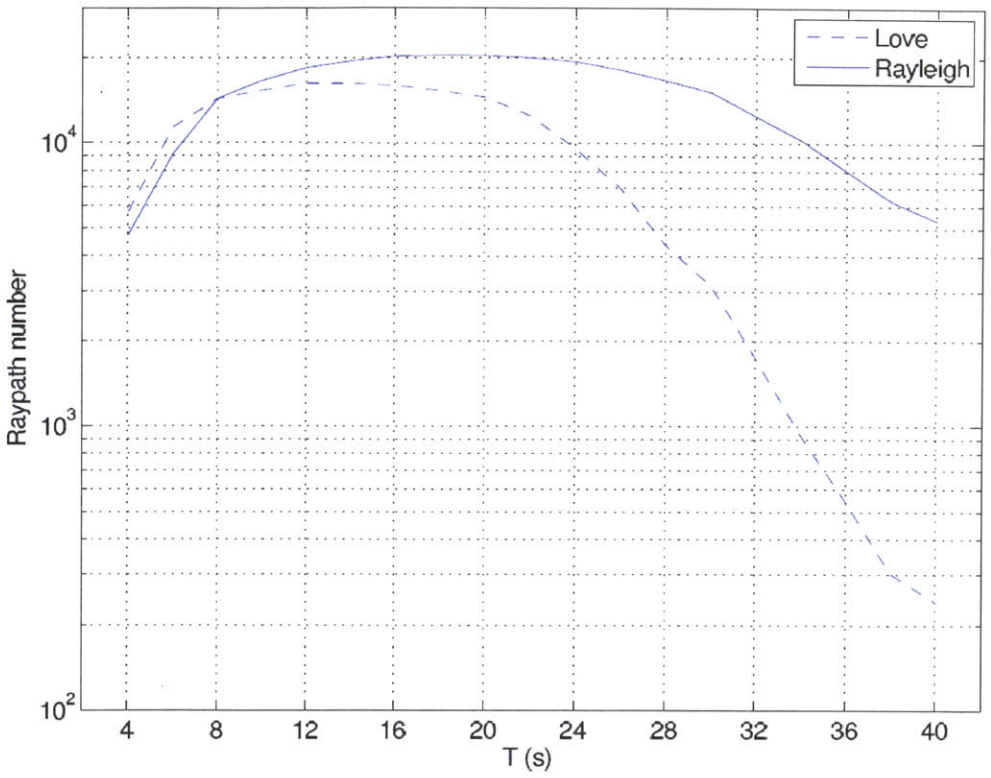

Figure 4-3. Numbers of measurements (traveltime) for both Rayleigh and Love waves.

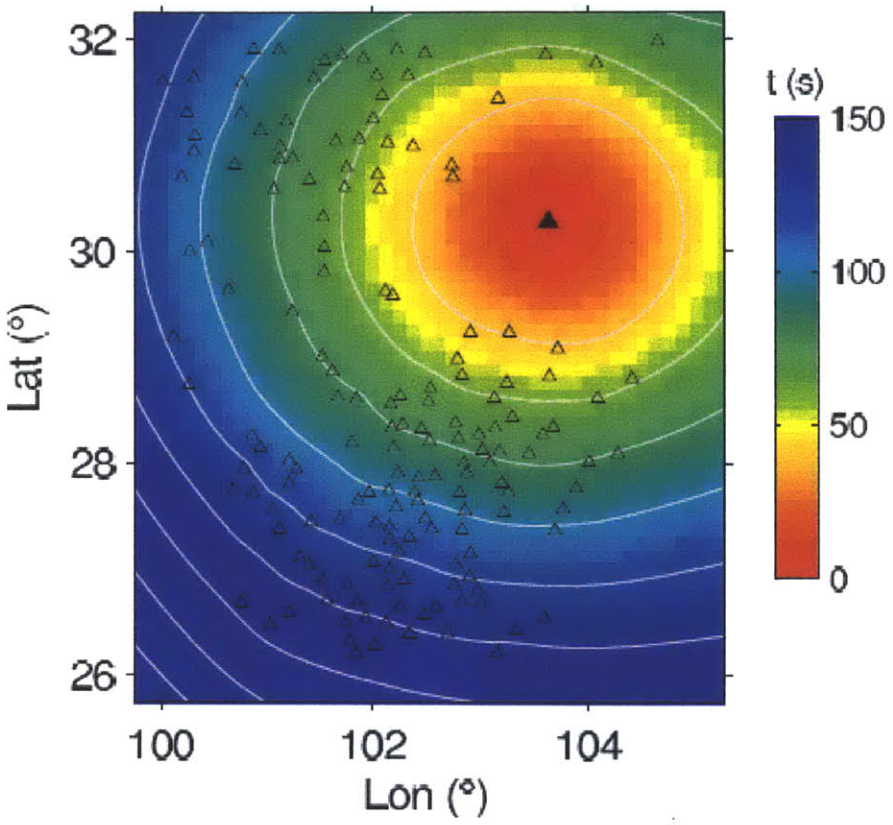

Figure 4-4. Interpolated traveltime from the virtual source station KCD10 for 10s (period) Rayleigh wave. The black solid triangle represents the location of the source station KCD10; and black hollow triangles show all other "receiver" stations where measurements are available. The silver curves are the traveltime contours with an increment of 20 s; and the innermost contour is the 40 s traveltime surface.

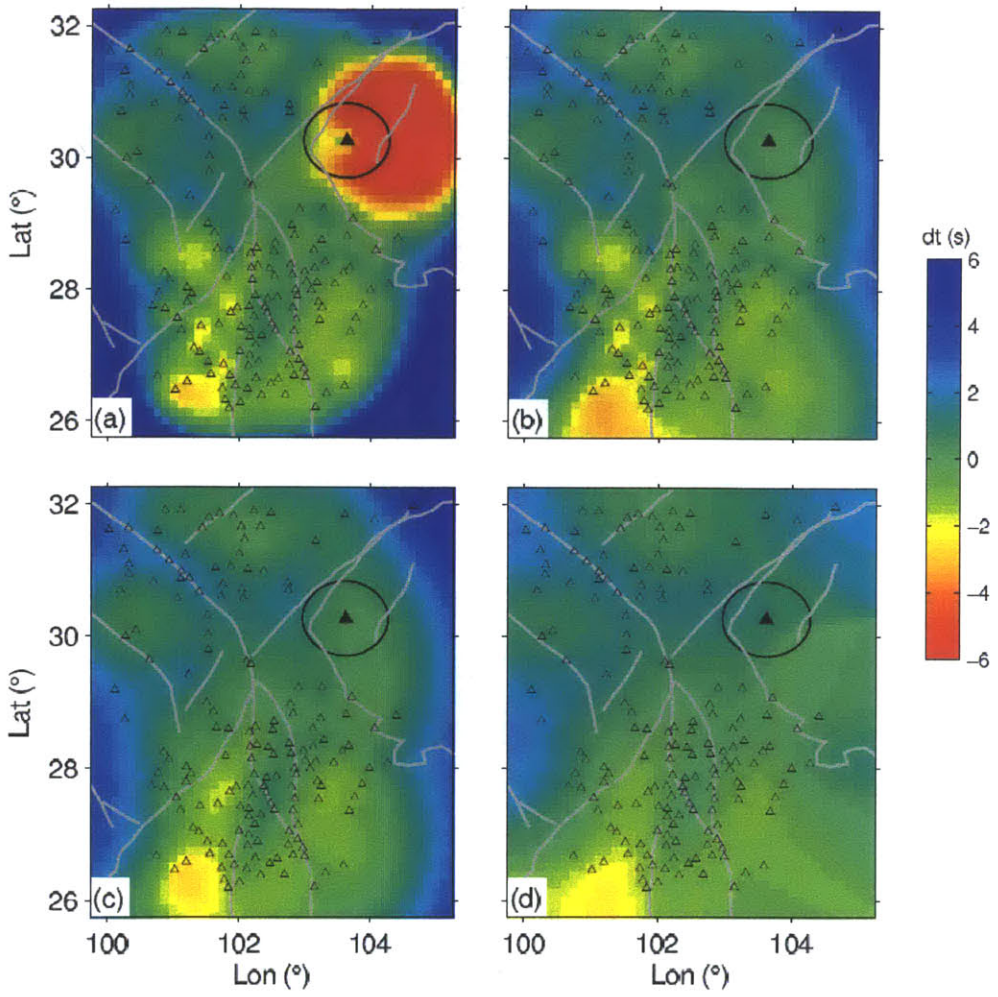

Figure 4-5. Perturbed traveltime from the virtual source station KCD10 for 10s (period) Rayleigh wave. The background traveltime based on a homogeneous wavespeed model has been removed. This figure shows the procedure of data processing and signal enhancing. The black circles are centered at the source station with 50 km radius. (a) The interpolation is on the total traveltime field, and then the reference traveltime field is removed. (b) The reference traveltime has been removed before the interpolation is performed. (c) The same as (b) but a damping term is used in interpolation. (d) A Gaussian filter is applied to smooth the traveltime in (c).

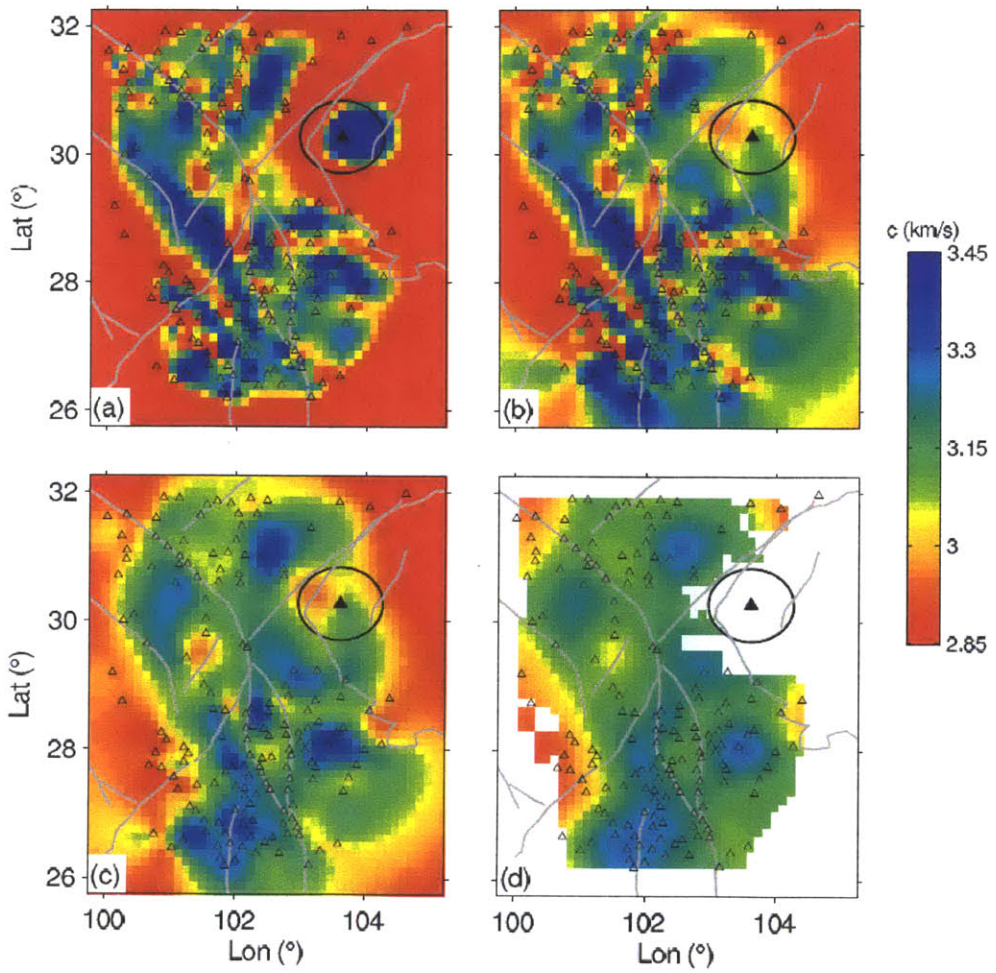

Figure 4-6. Phase velocity maps calculated from the traveltime fields in Figure 4-5. Locations with poor data coverage have been removed in (d). The improvement of calculation performance is clear from (a) to (d).

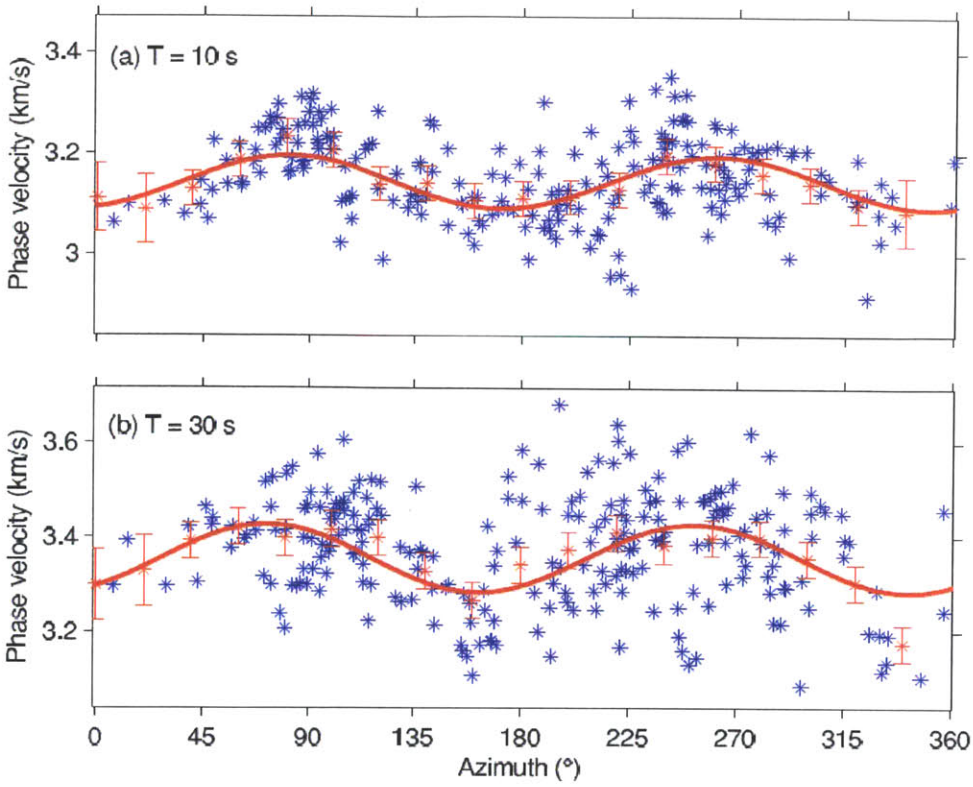

Figure 4-7. The variations of phase velocity against propagation direction at period (a) 10 s, and (b) 30 s for location (102°, 29°). The blue stars represent the results from different sources; the red stars with error bars are the average values and standard deviations of the wavespeed in the 20° angle bins. The thick red lines are the 2-ψ anisotropy fitting results for the averages values.

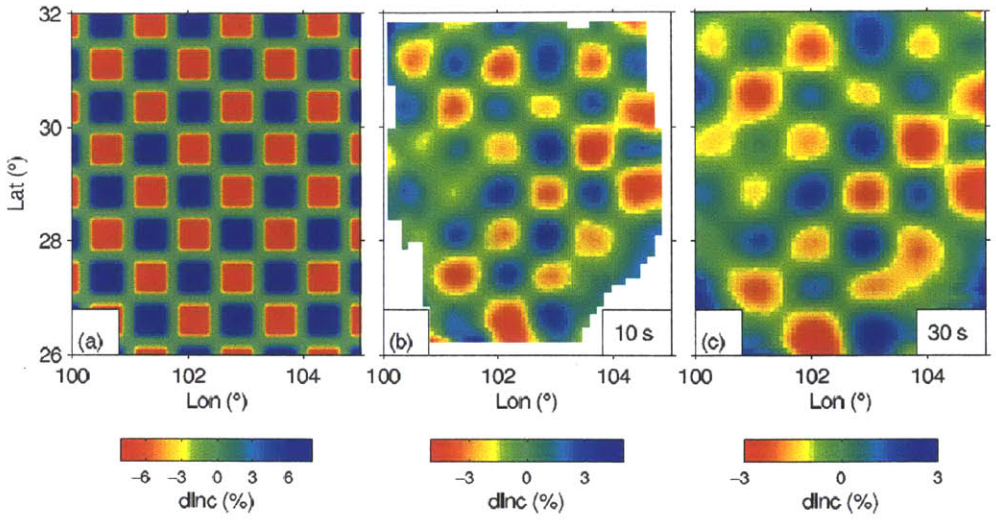

Figure 4-8. Checkerboard test for isotropic phase velocity: (a) $0.75^{o}\times0.75^{o}$ checkerboard model; (b) recovered model using 10 s Rayleigh wave data; and (c) recovered model using 30 s Rayleigh wave data.

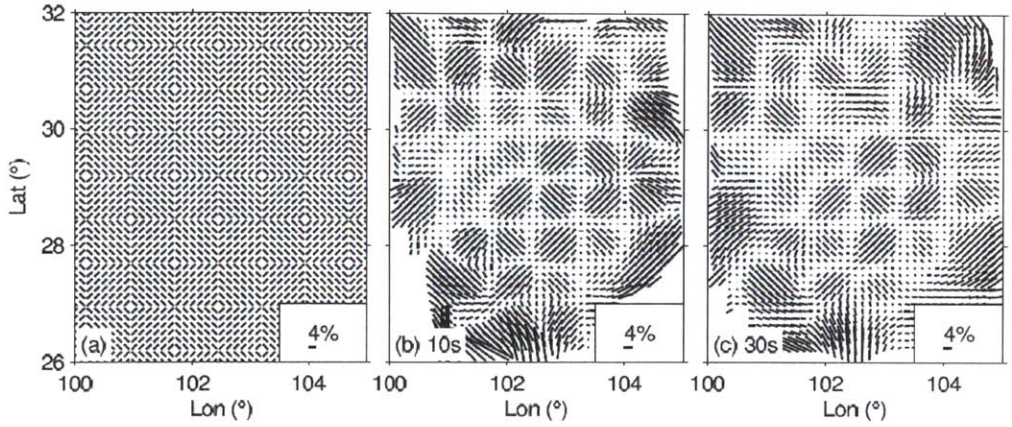

Figure 4-9. Checkerboard test for azimuthal anisotropy: (a) $0.75^{\circ}\times0.75^{\circ}$ checkerboard model; (b) recovered model using 10 s Rayleigh wave data; and (c) recovered model using 30 s Rayleigh wave data. The black bars describe both the fast direction and amplitude of the anisotropy.

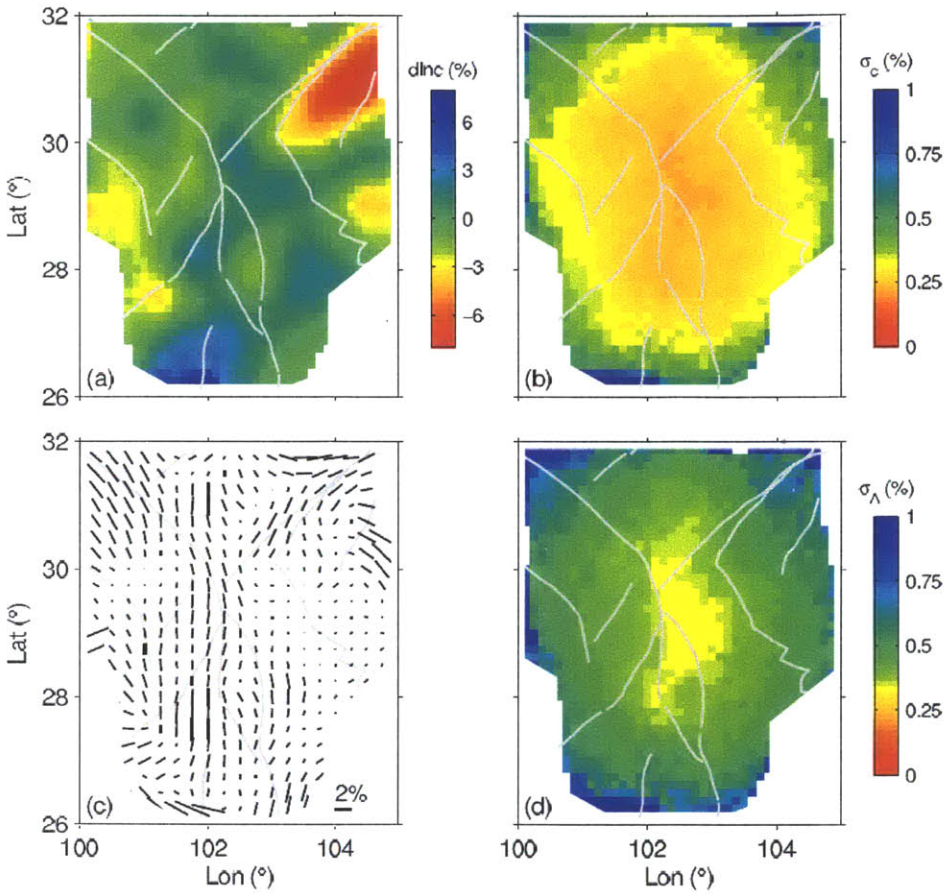

Figure 4-10. Eikonal tomography results for 10 s Rayleigh wave: (a) The isotropic phase velocity; (b) standard error for isotropic phase velocity; (c) azimuthal anisotropy; (c) standard error for the amplitude of azimuthal anisotropy.

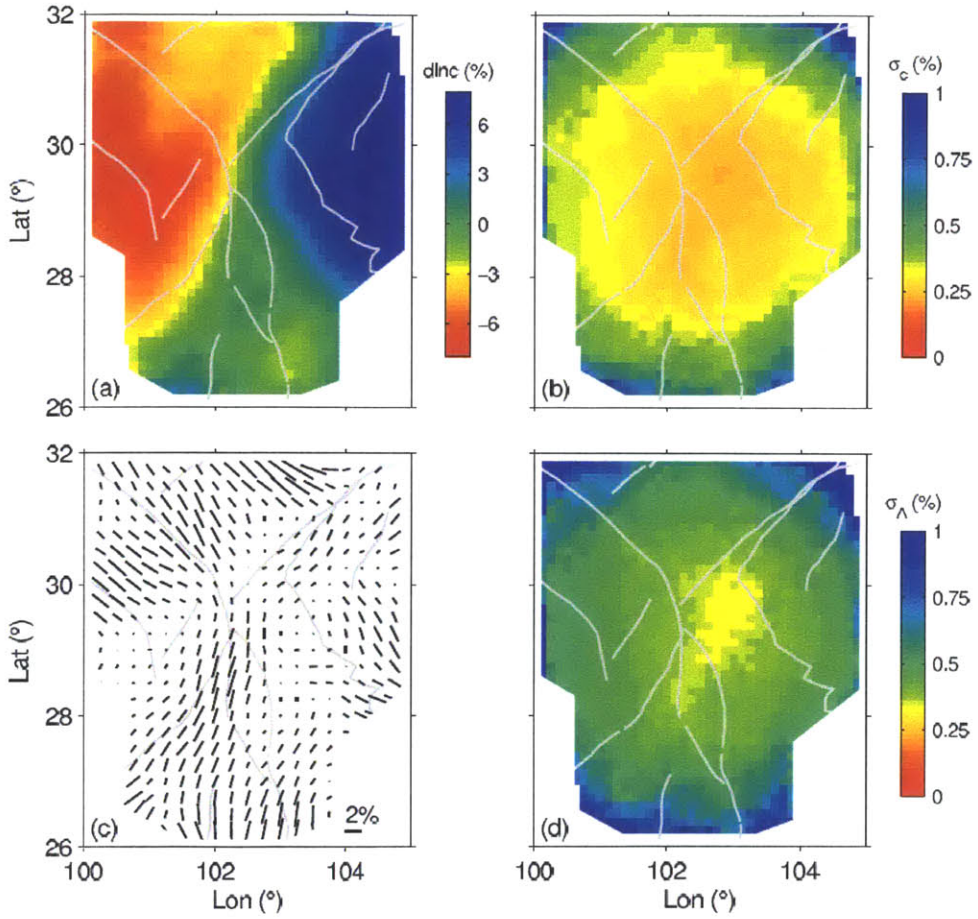

Figure 4-11. The same as Figure 4-10, but for 30 s Rayleigh wave.

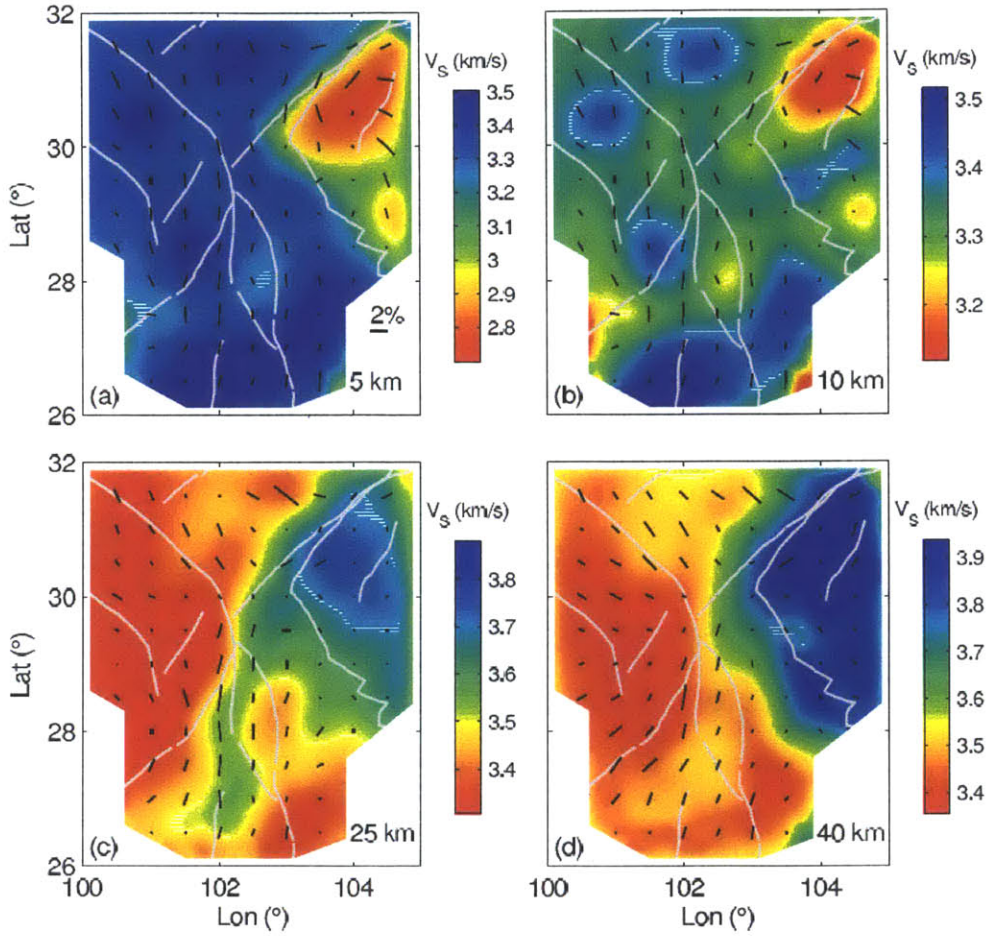

Figure 4-12. Variations of V_{SV} and azimuthal anisotropy at four depths: (a) 5 km; (b) 10 km; (c) 25 km; and (d) 40 km. The depths of 5 and 10 km represent the upper crust; and the 25 and 40 km represent the middle and lower crust, respectively.

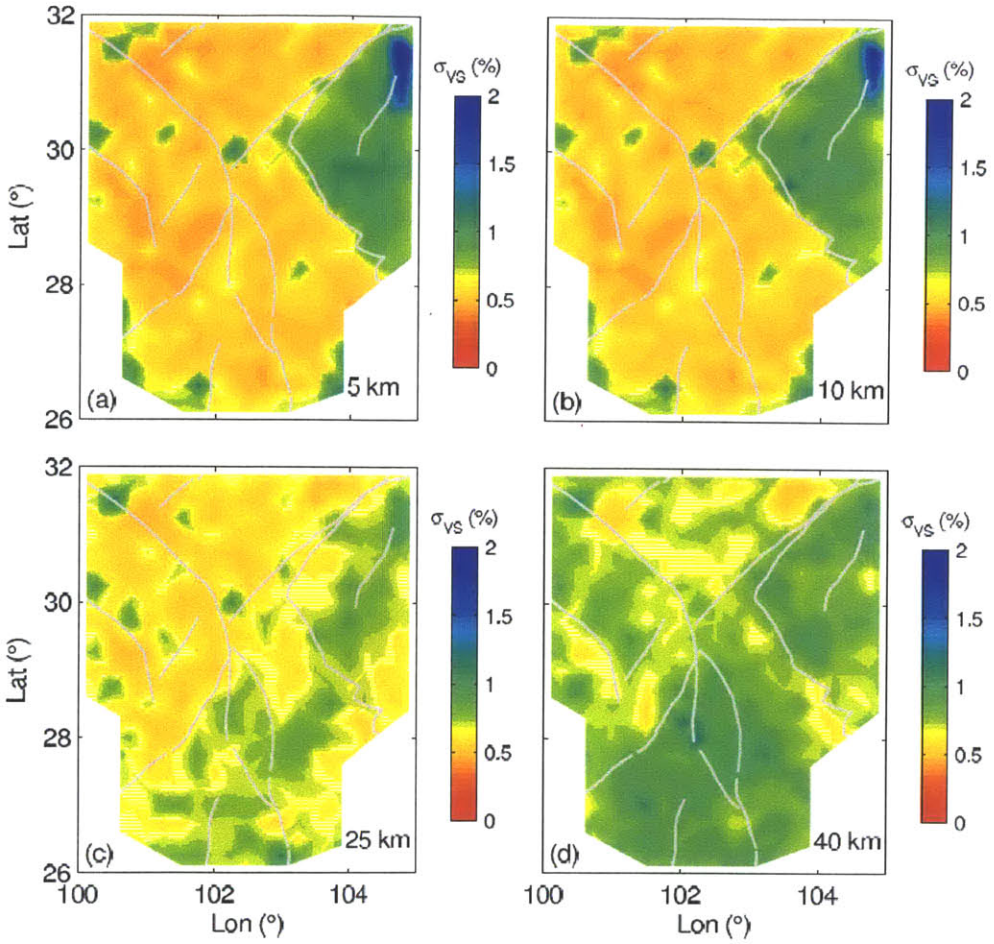

Figure 4-13. Standard errors (in percentage) for V_{SV}.

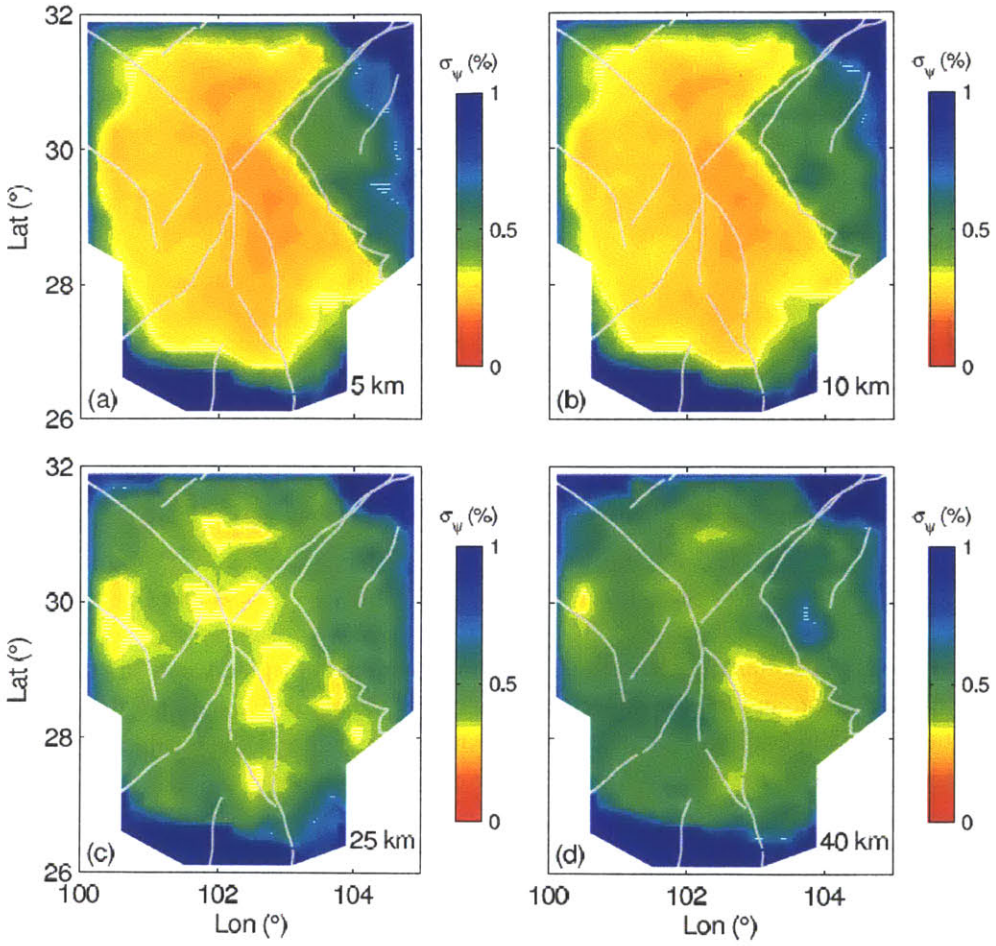

Figure 4-14. Standard errors for the amplitude of azimuthal anisotropy.

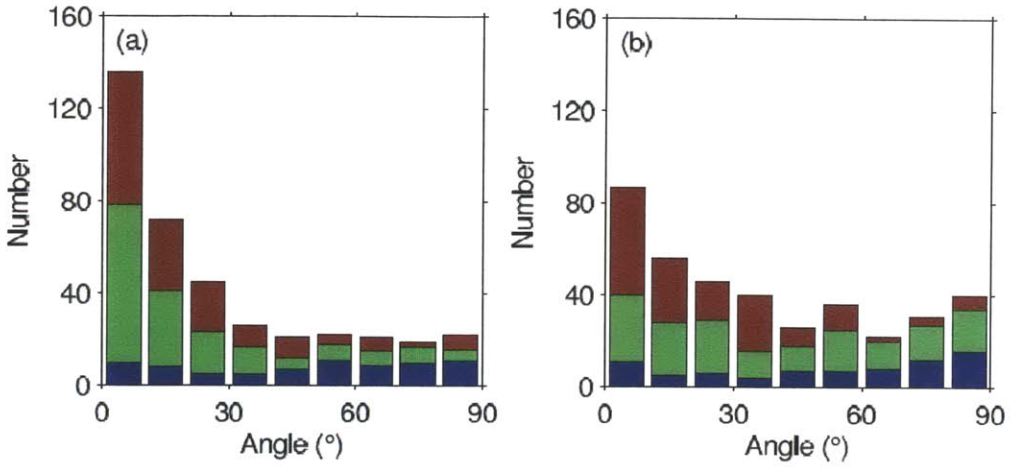

Figure 4-15. Angular differences of the azimuthal anisotropy between (a) the upper and middle crust; and (b) the upper and lower crust. The blue bars are for the Sichuan Basin; the green bars are for the Longmenshan, Yajiang, and Shangrila blocks; and the red bars are for the Central Yunnan and South China blocks.

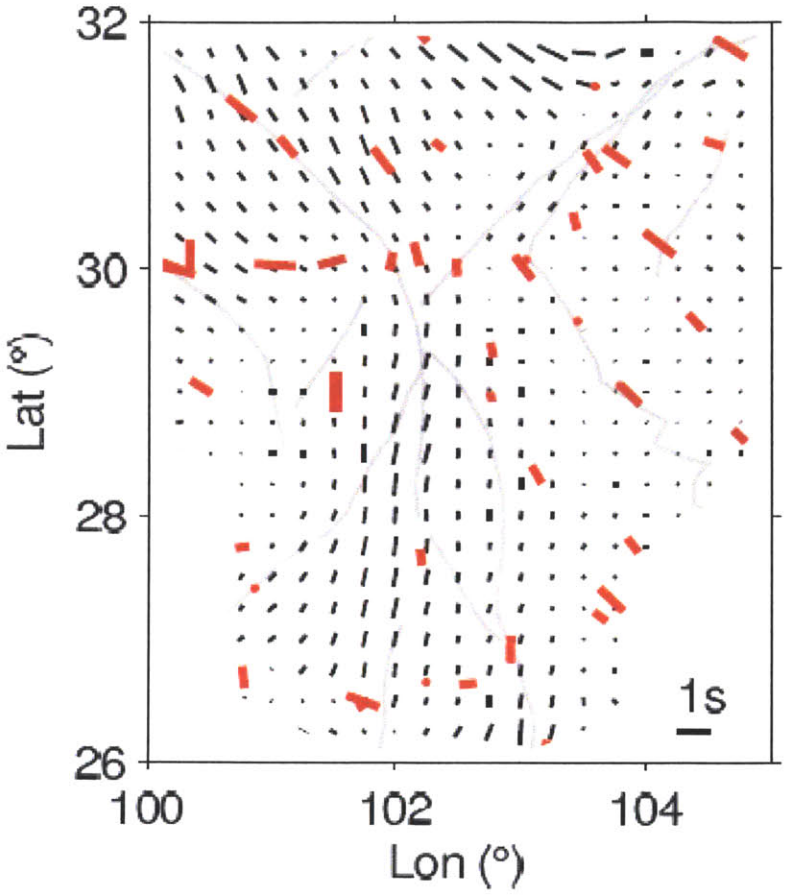

Figure 4-16. Comparison of the delay times measured from SKS splitting (Lev et al., 2006; Sol et al., 2007; Wang et al., 2008) and predicted from the anisotropic crustal model in this study. The measured and predicted delay times and fast directions are shown as red and black bars, respectively.

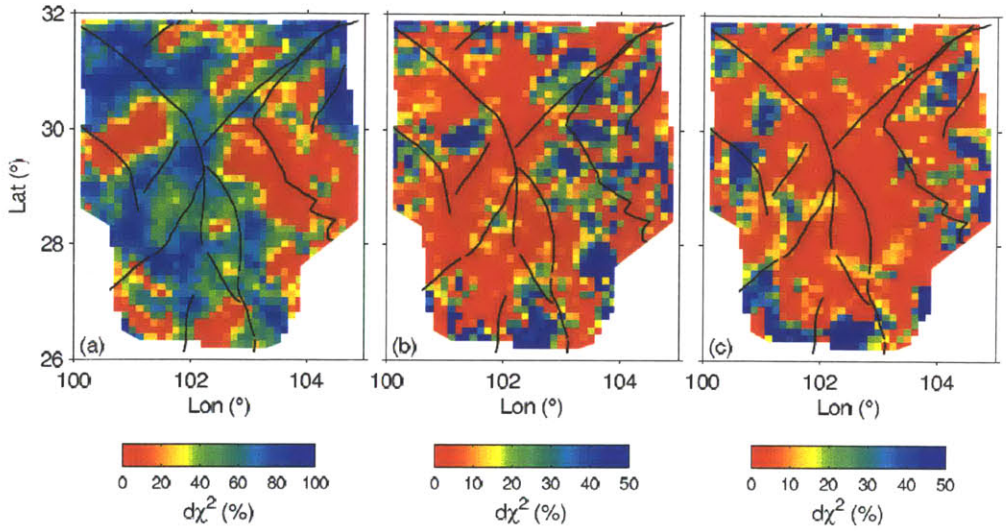

Figure 4A-1. Test of 1-ψ, 2-ψ and 4-ψ anisotropy for 10 s Rayleigh wave: (a) the reduction of χ^2 when only 2-ψ anisotropy is introduced with respect to the isotropic model; (b) the further deduction of χ^2 when both 1-ψ and 2-ψ anisotropies are introduced; and (c) the further deduction of χ^2 when both 2-ψ and 4-ψ anisotropies are introduced.

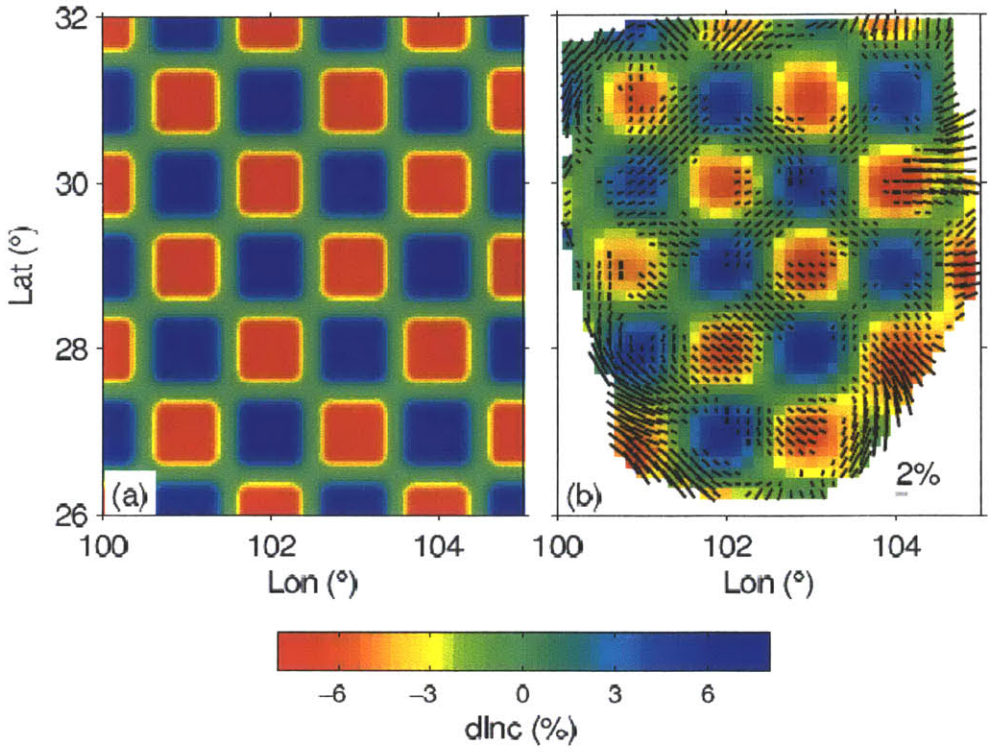

Figure 4A-2. Artificial azimuthal anisotropy from checkerboard model: (a) $1.0^{o}\times1.0^{o}$ checkerboard model; (b) recovered model using 10 s Rayleigh wave data. The phase velocity heterogeneities (isotropic part) are shown as background colors. The black bars show the artificial azimuthal anisotropy. We only plot anisotropies with amplitude larger than 1%.

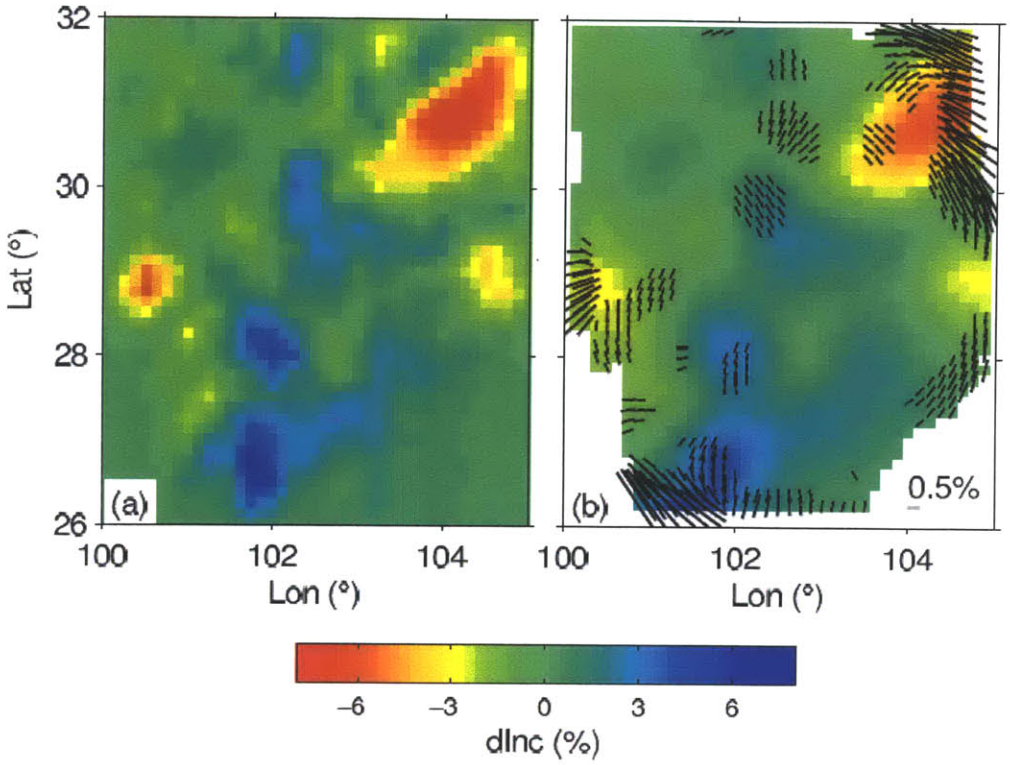

Figure 4A-3. Artificial azimuthal anisotropy from realistic model: (a) a realistic isotropic phase velocity model from traditional tomography at 10 s (Huang et al., 2013); (b) recovered model using 10 s Rayleigh wave data. We only plot anisotropies with magnitude larger than 0.5%.

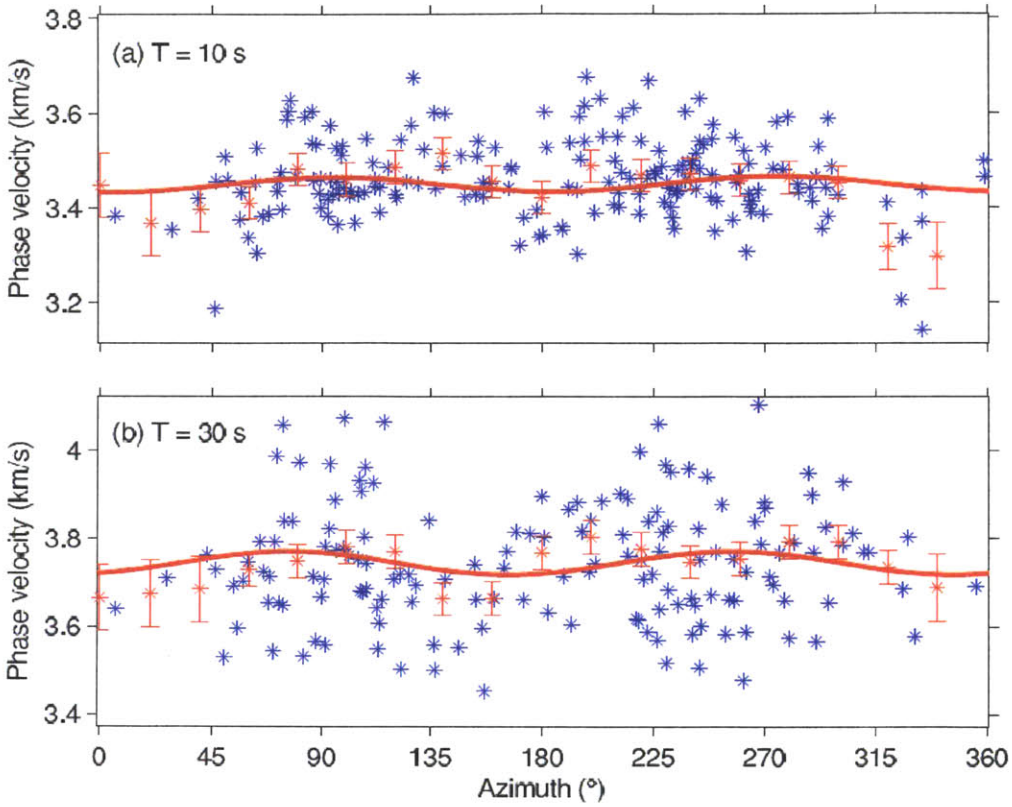

Figure 4B-1. The variations of Love wave phase velocity against the raypath direction at period (a) 10 s, and (b) 30 s for location (102°, 29°). The blue stars represent the results from different sources; the red stars with error bars are the average values and standard deviations of the wavespeed in the 20° angle bins. The thick red lines are the 2-ψ anisotropy fitting results for the averages values.

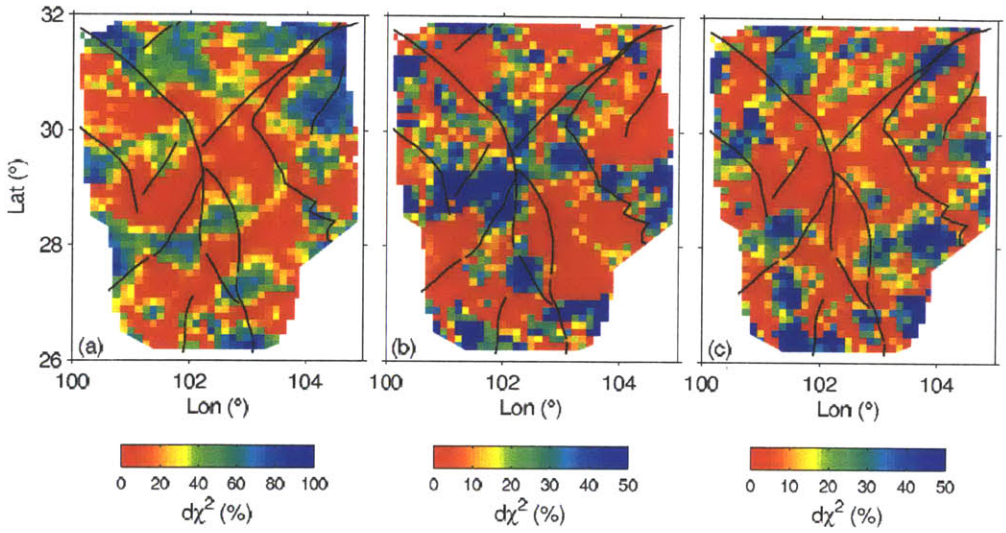

Figure 4B-2. Test of 1-ψ, 2-ψ and 4- ψ anisotropy for 10 s Love wave. It is the same as Figure 4A-1, but for 10 s (period) Love wave.

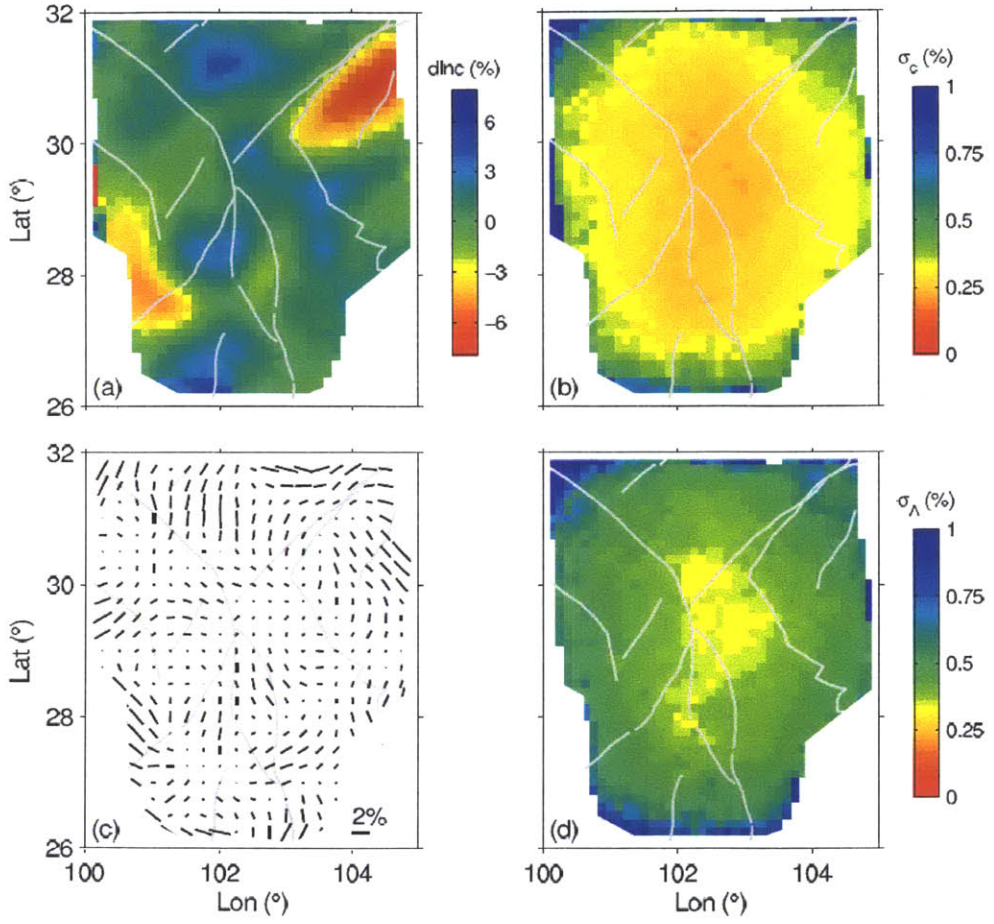

Figure 4B-3. Eikonal tomography results for 10 s Love wave: (a) the isotropic phase velocity; (b) standard error for isotropic phase velocity; (c) azimuthal anisotropy; (c) standard error for the magnitude of azimuthal anisotropy.

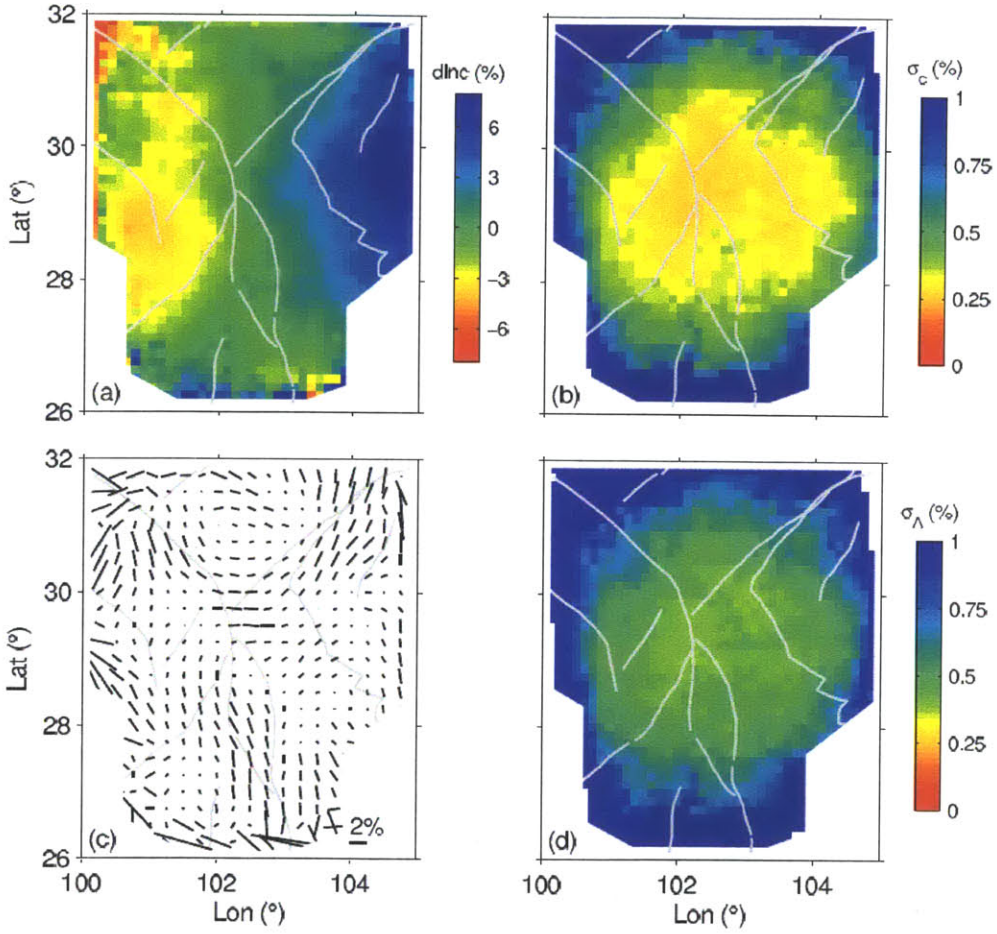

Figure 4B-4. The same as Figure 4B-3, but for 30 s Love wave.

Chapter 5

Concluding remarks

5.1 Summary

We have conducted surface wave tomography to study the structure and deformation in the crust of the southeastern Tibetan Plateau and surrounding regions. The Green's functions for both Rayleigh and Love waves are calculated from the seismic noise cross-correlation functions of the vertical and transverse components, respectively. Then we use the dispersion curves measured from the Green's functions to invert for shear wavespeeds and anisotropy.

In Chapter 2 and 3, we conduct traditional traveltime tomography to study the structures of the two shear wavespeeds and radial anisotropy. In Chapter 2, we use seismic records from two relatively sparse arrays deployed by Massachusetts Institute of Technology and Lehigh University. The two shear wavespeeds V_{SV} and V_{SH} are inverted separately from the dispersion curves of the Rayleigh and Love waves, respectively. Then the differences of the two wavespeeds are examined as radial anisotropy. In Chapter 3, we use seismic records from a densely deployed array by China Earthquake Administration (CEA). To better constrain the radial anisotropy, we jointly invert for the two wavespeeds thus the radial anisotropy is explicitly included in the inversion. Besides regularization terms for the wavespeeds, we also introduce a

term in the penalty function to require smooth variation of the radial anisotropy. The major results and conclusions in the Chapter 2 and 3 are similar, but the work in Chapter 3 reveals more detailed structures in the area where the studies overlap due to the much denser raypath coverage from CEA array. In Chapter 4, we conduct Eikonal tomography to study the structures of the vertically polarized shear wavespeed V_{SV} and its azimuthal anisotropy. We use seismic records from CEA array. The traveltime of Rayleigh wave from a virtual source station is calculated for every location in the study region using an improved minimum curvature interpolation method. Then the local wave slowness and propagation direction are obtained from the gradient of the traveltime. Major results of our tomography works are summarized below.

For the Sichuan Basin, the first-order feature of the wavespeeds is slow anomalies in the upper crust and fast anomalies in the middle and lower crust, consistent with thick sedimentary at surface and indicating cold and rigid basement in depth. Careful examination reveals finer structure in the upper crust. The strongest low wavespeed anomalies are located in the area bounded by the Longmenshan fault to the west and Longquan fault to the east, a foreland basin with sediments of about 10 km thick (Yong et al., 2003; Dong et al., 2006). In the sub-units with higher topography and thinner sediments (of about 1-2 km) west of the Longquan fault (Meng et al., 2005), the wavespeeds are faster than those in the foreland basin proper. Radial anisotropy is positive ($V_{SH}>V_{SV}$) and strong (~4%) in the upper crust and the largest magnitude appears in the foreland basin between the Longmenshan and Longquan faults, probably reflecting horizontal layering of the sediments. In the middle and lower crust,

radial anisotropy is very small (<2%). Small azimuthal anisotropy is found throughout the entire crust (~1%), indicating little deformation within the crust of the Sichuan Basin.

For the high Tibetan Plateau, the most dominant feature is the ubiquitous low wavespeed zones in the middle and lower crust. The strongest low wavespeed anomalies appear in the middle crust of the Lhasa block and middle and lower crust of the Yidun Arc and southern part of the Songpan-Ganze fold belt (south to the Xianshuihe fault). In the Qiangtang block and the northern part of the Songpan-Ganze fold belt (north to the Xianshuihe fault), the magnitude of the low wavespeed anomalies are relatively weak. The radial anisotropy is always positive ($V_{SH}>V_{SV}$) and well correlated with the low wavespeed zones in the middle and lower crust; its largest magnitudes also appear in the middle crust of the Lhasa block and middle and lower crust of the Yidun Arc and southern part of the Songpan-Ganze fold belt. The negative correlation between V_{SV} and radial anisotropy is significant in the middle and lower crust of the southeastern Tibetan Plateau, which we suggest is due to the combined effects of increased temperature and horizontal flow. In general, the azimuthal anisotropy in the southeastern Tibet is consistent with a clockwise rotation around the Eastern Himalayan Syntaxis; however, the angular differences between their fast directions in the upper and lower crust are large. Therefore, the deformation pattern at surface may be different from that in depth.

The Central Yunnan block, bounded by the Lijian-Muli fault to the northwest, the Anninghe-Zemuhe-Xiaojiang fault to the east, and the Red River fault to the

southwest, can be approximately divided into two parts. The northern part, north to the 26°N, has higher wavespeeds than the surrounding areas throughout the whole crust. The southern part has very low wavespeed in the lower crust. Radial anisotropy is small in the entire crust of the northern part; while it is positive and strong in the middle and lower crust of the southern part. Since we only conduct Eikonal tomography for the CEA data, azimuthal anisotropy is obtained only for the northern part of the Central Yunnan block. The azimuthal anisotropy, with magnitude of about 2%, reveals fast directions of nearly NS in the middle crust and NNE-SSW in the lower crust. The northern part of the Central Yunnan block geographically coincides with the inner core of the Emeishan large igneous province (He et al., 2003), and gravity study observes high density anomaly in this area (Lou and Wang, 2005), indicating intruded material from mantle. This material intrusion and Emeishan basalt floor occurs at the onset of the Mesozoic (He et al., 2003), the remnant of which may combine with horizontal flow initiated in the Cenozoic (Royden et al., 2008) to reveal relatively high wavespeed, small radial anisotropy, and azimuthal anisotropy in the flow direction.

In summary, our tomography study has revealed detailed structure for the crust of the Sichuan Basin, southeastern Tibetan Plateau, and Central Yunnan block. Strong contrasts are observed between the high Tibetan Plateau and Sichuan Basin in aspects of wavespeeds and radial and azimuthal anisotropy. A mechanically weak middle and lower crust is suggested for the Tibet Plateau and Central Yunnan block, in which large deformation and material transport or flow may occur. Our results also suggest

large lateral variation of the flow intensity and pattern in different geological units. Thus, the Tibetan Plateau can be divided into subunits which have distinct features of wavespeeds and anisotropy, although these subunits or blocks are by no means rigid.

5.2 Future work

In this thesis, surface wave Green's functions are calculated using ambient noise interferometry. Since the two dominated period bands of noise cross-correlation functions, i.e. 6-9 s and 15-17 s (Bensen et al., 2007), are both in the short period range, it is difficult to extract long period surface wave Green's function (> 40 s) using the interferometry method. Therefore, to study structures in mantle, we have to construct Green's function at longer periods using other methods. Yao et al. (2006) develop a two-station analysis method using earthquake coda waves to extract Rayleigh waves in the period band of 20-150 s and apply it to both MIT and Lehigh arrays (Yao et al., 2010). This two-station analysis can also be applied to MIT and Lehigh arrays for Love wave and CEA array for both Rayleigh and Love waves to study the structures of the two wavespeeds and radial and azimuthal anisotropy in mantle. A comprehensive study of wavespeeds and anisotropy in the crust and mantle down to about 300 km can greatly improve our understanding about the deformation and thus dynamic evolution for the southeastern Tibet.

Secondly, we can include azimuthal anisotropy in the traditional tomography. Currently, we invert for isotropic phase velocities for surface waves using traditional tomography method in Chapter 3, and we measure the azimuthal anisotropy using

Eikonal tomography in Chapter 4. However, azimuthal anisotropy can also be introduced in tradition tomography (Yao et al., 2010), and the results can be compared with those in Eikonal tomography. This can improve our understanding about the difference of the two tomography methods, for example, their advantages and drawbacks.

Third, the improved minimum curvature interpolation in Chapter 4 ensures accurate estimation of traveltime field and produce stable results for wavespeed and azimuthal anisotropy. We can apply it to other data set, including noise and earthquake data from other arrays, to study the lithosphere structure and deformation for other regions.

References

Bensen, G.D., M.H. Ritzwoller, M.P. Barmin, A.L. Levshin, F. Lin, M.P. Moschetti, N.M. Shapiro, and Y. Yang, (2007), Processing seismic ambient noise data to obtain reliable broad-band surface wave dispersion measurements, Geophys. J. Int., 169, 1239-1260.

Dong, J., Wei G., Chen Z., Li B., Zeng Q., and Yang G., (2006), Longmen Shan fold-thrust belt and its relation to the western Sichuan Basin in central China: new insights from hydrocarbon exploration, The American Association of Petroleum Geologists Bulletin, 90(9), 1425-1447.

He B., Xu Y., Chung S., Xiao L., and Wang Y., (2003), Sedimentary evidence for a rapid, kilometer-scale crustal doming prior to the eruption of the Emeishan flood basalts, Earth and Planetary Science Letters, 213, 391-405, doi:10.1016/S0012-821X(03)00323-6.

Lou, H., and Wang C., (2005), Wavelet analysis and interpretation of gravity data in Sichuan-Yunnan region, China, ACTA Seismologica Sinica, 18(5), 552-561.

Meng, Q., E. Wang, and Hu J., (2005), Mesozoic sedimentary evolution of the northwest Sichuan basin: Implication for continued clockwise rotation of the South China block, Geological Society of America Bulletin, 117 (3/4), 396-410. doi: 10.1130/B25407.

Royden, L.H., B.C. Burchfiel, R.D. van der Hilst, (2008), The geological evolution of the Tibetan plateau, Science, 321, 1054-1058.

Yao, H., R. D. van der Hilst, and M. V. De Hoop, (2006), Surface-wave array tomography in SE Tibet from ambient seismic noise and two-station analysis – I. Phase velocity maps, *Geophys. J. Int.*, 166, 732-744, doi: 10.1111/j.1365-246X.2006.03028.x.

Yao, H., R. D. van der Hilst, and J.P. Montagner, (2010), Heterogeneity and anisotropy of the lithosphere of SE Tibet from surface wave array tomography, Journal of Geophysical Research, 115, B12307, doi:10.1029/2009JB007142.

Yong, L., Allen P.A., Densmore A.L., and Qiang X., (2003), Evolution of the Longmen Shan foreland basin (Western Sichuan, China) during the Late Triassic Indosinian orogeny, Basin Research, 15, 117-138.